REDUCED-ORDER ANALYSIS OF DUAL MODE SUPERSONIC COMBUSTION RAMJET PROPULSION SYSTEM

by

VIJAY GOPAL

Presented to the Faculty of the Graduate School of

The University of Texas at Arlington in Partial Fulfillment

of the Requirements

for the Degree of

MASTER OF SCIENCE IN AEROSPACE ENGINEERING

THE UNIVERSITY OF TEXAS AT ARLINGTON

DECEMBER 2015

Acknowledgements

I would like to thank my parents Mrs. Sheelavathy Gopal and Mr. Gopal Ananthan for their complete financial and moral support during the master's program. Also, I would like to thank my advisor Dr. Donald R. Wilson for his valuable guidance and thesis committee members Dr. Frank Lu and Dr. Atilla Dogan for their ideas and feedback on the research work.

I am thankful to my uncle Mr. Venkatesh Ananthan and aunt Mrs. Rekha Venkatesh for their support during my stay at the US.

I extend my thanks to my colleague Nandakumar Vijayakumar for valuable suggestions made in the research work.

I would like to thank my friends, Shashank Ramesh, Varun Vishwamithra, Purushotham Balaji, Hatim Rangwala, Esteban Cisneros, Rohit Raju, Warren Freitas, Rahul Kumar, and Umang Dighe for their timely help and support during the course of the master's program.

November 20, 2015

Abstract

REDUCED-ORDER ANALYSIS OF DUAL MODE SUPERSONIC COMBUSTION RAMJET PROPULSION SYSTEM

Vijay Gopal, M.S.

The University of Texas at Arlington, 2015

Supervising Professor: Donald R Wilson

High speed propulsion systems typically possess relatively simple geometry but the complexity involved in the flow characteristics makes their analysis a challenging task. The current research work introduces a reduced order analytical model for a steady operation of dual mode SCRamjet (Supersonic Combustion Ramjet) propulsion system at design and off-design conditions. The model hopes to reduce analysis time and complexity to carry out parametric sweep studies for preliminary design of SCRamjet engines.

The analytical model splits the analysis of SCRamjet engine into five interactive components namely: inlet, isolator, injector, burner and nozzle. Each component is modelled using physics of gas-dynamics and semi-empirical relations. The flow characterization of each component and their interactions are modelled carefully based on observed physical phenomenon reported in the existing literature. The model is developed on MATLAB platform providing flexibility to design a parametrized SCRamjet geometry and to select its free stream and fueling conditions for the analysis.

The analytical model proposed in the current work is validated with various experimental and computational data of individual components and its reliability for predicting the flow characteristics inside a SCRamjet propulsion system is discussed in detail.

Table of Contents

List of Illustrations

List of Tables

Chapter 1

Introduction

Efforts across the globe are underway to develop and realize high speed air-breathing propulsion systems. These systems aim to propel flight at velocities more than a kilometer per second using ambient air as the working gas and are often referred as SCRamjet engines. Realizing such propulsion systems involves multidisciplinary approach. These disciplines mainly include aerothermodynamics, heat transfer, aerodynamic control and structures. In this chapter an overview of the philosophy behind high speed air-breathing propulsion is discussed.

1.1 Why High Speed Atmospheric Propulsion is Necessary?

Rockets are reliable propulsion system which can propel objects at hypersonic speeds. The principle behind rocket propulsion is based on newton's third law where the reaction force generated from propellants leaving the nozzle accelerates the rocket to required velocities. As these propellants stored inside the rocket consumes 80 to 90% of the total mass of the rocket, the payload mass fraction turns out to be around 4-5% [25]. This makes the cost per unit mass of payload for a mission to be expensive. Therefore the motivation is to increase the payload fraction by considering air-breathing engine configuration, where the ambient air is used as the oxidizer instead of carrying it separately as in the case of rocket. This hopes to provide a higher payload fraction compared to rockets thereby cutting the cost of the mission dramatically. Another potential benefit is the possibility of reusing the air-breathing propulsion system like for example SSTO (Single Stage to Orbit) propulsion concept which can potentially cut down operational cost of the launch vehicle [25]. Therefore the access to space by considering air-breathing stage within atmosphere has enormous potential to cut down mission cost.

Military applications of high speed air-breathing engines include mainly tactical missiles which can provide quick response time capability against adversaries. On the other hand for civilian transport applications the high speed air-breathing engines can cut travel time dramatically. However the current technology as of 2015 is far from realizing a civilian hypersonic transport. Therefore high-speed air breathing propulsion remains an important aspect of aerospace technology which has potential to revolutionize the space access and military capabilities.

1.2 Where Do We Stand as of 2015?

The U.S. Navy was the first agency to carry out supersonic combustion ground test during 1957-1962 followed by Russia's Chetinkov research center around the same time [4]. A number of ground test since then was carried out by US, Russia, France, UK, Japan and Germany [4]. The first SCRamjet flight test was carried out by Russia called the Kholod on November 28th 1991 [4] reaching a Mach number of 5.8. The Kholod project was then collaborated with the US when NASA and CIAM worked together on a flight test [1] which lasted for 77 seconds on February 12th 1998. Another notable SCRamjet flight test was performed by NASA called the X-43A which had reached Mach 9.6 for about 10 seconds on 16 Nov 2004 [36]. Since then a number of countries have carried out flight test which includes India, China and Australia. As of 2015, the U.S.A's X-51A holds a record for longest air-breathing hypersonic flight which flew for 210 sec at Mach 5.1 [37] on May 1st 2013. The X-51A is a wind-tunnel sized engine which demonstrated sustained supersonic combustion and proved the concept of SCRamjet powered flight is a reality. The hypersonic flight which can takeoff from ground is still on a drawing board today but not far from reality. In a matter of 100 years after the first flight by Wright brothers which flew approximately at 30-35mph for 59 seconds, we have today reached 3400mph for about 210 seconds. This is a big leap in aviation capability and mankind will always try to

push its limits. Some of the current hypersonic propulsion programs across the world obtained from the public domain are detailed in Table 1.1.

Table 1-1 Some hypersonic programs across the globe as of 2015.

Program/Vehicle	Country/Agency
HiFiRE / SCRamjet	USA, Australia / NASA, AFRL, DSTO
Falcon / Waverider	USA / DARPA
- / SCRamjet	Germany / DLR
GLL-AP-02 / SCRamjet	Russia / Gromov Flight Research Institute
HSTDV / SCRamjet	India / DRDO
SABRE / Combined cycle	UK / Reaction Engines Limited
AVATAR / RLV (SPEX)	India / ISRO
- / SCRamjet	China / -
Bramhos-II / SCRamjet	India, Russia / DRDO, NPO
SR-72 / SCRamjet	USA / Lockheed Martin
HEXAFLY-INT /-	European Union / ESA, DLR, AIRBUS etc.
Hy V / SCRamjet	USA / VSGC Universities, ATK GASL
14-X / SCRamjet	Brazil / Brazilian Air Force

1.3 Technological Barriers

The SCRamjet engine is operational once the flight Mach number exceeds the starting Mach number (usually above Mach 4), therefore, it alone cannot take-off from ground. There exists a technological challenge to integrate different propulsion systems to boost the SCRamjet above its starting Mach number, like for example turbine based combined cycle (TBCC). This adds to the complexity of the design and hence requires additional structures for integration. The additional structures can potentially increase the weight leading to a lower projection of payload mass fraction. The starting Mach number requirement of the SCRamjet can be decreased if it is designed to operate as a dual mode SCRamjet [38].

The compression process of the SCRamjet engine is highly dissipative in nature which produces substantial total pressure losses due to shock phenomenon. The higher the total pressure losses, the bigger is the nozzle required for matched expansion. This leads to a penalty on drag. Additionally the shock structure dramatically varies at off-design

conditions leading to huge variation in mass flow rate which affects the performance of the engine. Therefore there exist a necessity to design a variable geometry SCRamjet inlet. However, the implementation of a variable geometry inlet possess a serious challenge to the structural and dynamic aspect of the design as the inlet is subjected to high heat and mechanical loads.

The combustion process in SCRamjet is a huge technological barrier. The supersonic fuel-air mixing process is largely affected by compressibility effects which inhibits an efficient combustion process inside the burner. There exist a necessity for better understanding of supersonic fuel-air mixing process and the associated combustion instabilities in order to manipulate and achieve favorable levels of burner efficiencies. Some recent advancement in supersonic combustion includes the use of hyper-mixers [6], plasma torch [39] and cavity based mixing enhancement [15]. Another road block for efficient combustion in a SCRamjet is the ignition time delay. This is because residence time of the air inside the burner is so low that it is of same order of magnitude as that of the chemical time-scales. Therefore incomplete combustion process leads to decrease in thrust obtained from engine. On other technological fronts, the gasification, storage and injection of fuel remains a challenging task.

Thermal protection systems for a SCRamjet engine becomes increasingly important as the flight Mach number increases. The thermal hot spots found in the inlet or the hot flow inside burner can make the wall temperature go beyond 2500 K. Unlike rockets, SCRamjets takes a longer trajectory for accelerated flight path which demands materials which can support thermal loads for longer duration of flight. Realizing such materials for thermal protection systems remains a technological challenge. Also, the design of thermal protection systems requires a better understanding of wall-boundary layer interaction which remains a scientific barrier to predict the wall temperatures accurately. If the thermal

protection system is based on incorrect prediction of wall temperatures, then the SCRamjet can get disintegrated during its flight leading to a catastrophe.

The SCRamjet propulsion system is highly multidisciplinary in nature in which the flight dynamics is closely coupled with propulsion and structural aspect of the design. The control of hypersonic vehicle is vital as the mechanical loads (especially moments) and the propulsion efficiencies are very sensitive to the flight dynamic parameters. The implementation of control surfaces and fast response control actuators remains a challenging task.

1.4 How Does Current Work Contribute?

The current research work presented in this document proposes a reduced order analytical model of dual mode SCRamjet engine. This model hopes to reduce analysis time and cost to carry out parametric sweep studies of SCRamjet engine. The reduced order model preserves the physical characteristics of the flow to accurately predict the flow variables and their distribution along the engine. The geometry for the SCRamjet analysis is parametrized such that typical existing designs fall in its simulation space. The reliability of the reduced order model is established by validating with experimental and computational results obtained from the existing literatures. Therefore the model serves as a useful tool in the preliminary design phase of SCRamjet engine which provides reliable trends for the designers. The flexibility in the model provides a credible platform to reduce the design space in which high fidelity analysis or experiments can be performed.

Chapter 2

SCRamjet Propulsion System

In this chapter a brief introduction to the working of a typical SCRamjet engine and some existing methodologies to analyze the same are presented. A schematic of a typical SCRamjet is depicted in Figure 2.1.

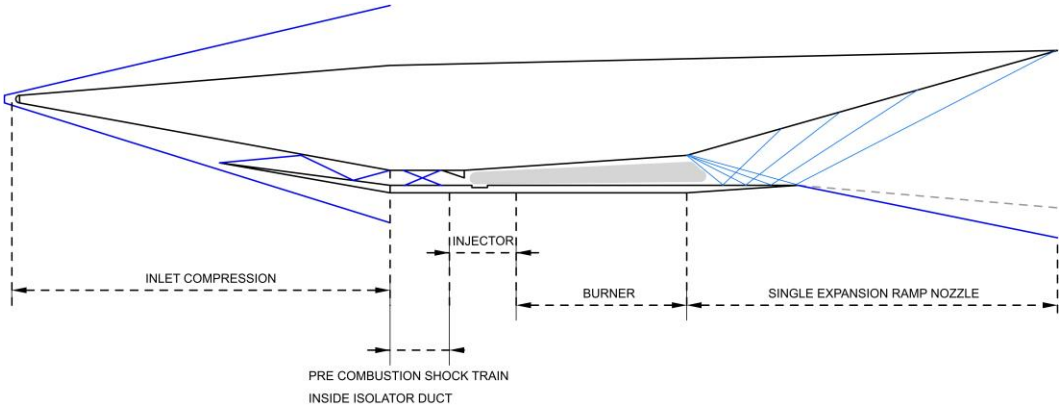

Figure 2-1: Schematic of a typical SCRamjet engine process.

The dual mode SCRamjet engine process depicted in Figure 2-1 compresses the air through a shockwave process followed by either a supersonic or subsonic combustion process which eventually expands to produce thrust. The components of a typical SCRamjet includes the following:

- Inlet
- Isolator
- Burner
- Single expansion ramp nozzle

These components are discussed briefly to outline the operation of a typical dual mode SCRamjet engine. Upon discussing the components of SCRamjet engine, some of its existing reduced order models are also discussed as a part of the literature review.

2.1 Inlet

SCRamjet inlet compresses the air using shockwaves. These shock patterns depend on the inlet geometry and flight Mach number. The shock patterns govern vital parameters of the inlet performance such as mass flow rate, total pressure losses and temperature ratio. The inlet captures maximum mass flow rate at on-design conditions (or Shock on lip) and at off-design conditions the inlet flow field is complex and its performance changes drastically. Variable geometry of the inlet has the potential to operate over wide ranges but its feasibility in high speed flight remains a challenging task. When flight Mach numbers are low enough, the SCRamjet inlet unstarts by establishing a normal shockwave at the entrance of the internal inlet. This reduces mass flow rate due to spillage effect.

2.2 Isolator

The isolator shown in Figure 2-1, is typically a constant area duct which provides necessary pressure rise to prevent the burner from interfering with the inlet compression process. During supersonic combustion the pressure inside the burner increase. When the pressure rise is sufficiently large, the boundary layer inside the isolator separates causing pre-combustion shockwaves to balance the burner back pressure. During subsonic combustion, normal shock trains are established inside the isolator which provides favorable entrance Mach number for the burner to establish the thermal throat and operate in Ramjet mode. Therefore the inlet-isolator system essentially provides an interactive compression process for the burner operation.

2.3 Burner

SCRamjet burner is typically a diverging duct (Figure 2-1) that can operate in supersonic or subsonic mode. The supersonic mode is usually established at higher flight Mach numbers and/or with lower fueling conditions when compared to subsonic mode scenarios. The process of fuel-air mixing dictates the heat addition process for SCRamjet

flight. During supersonic mode the mixing of fuel-air is inhibited by compressible effects while for the subsonic mode the fuel-air mixing process is quicker. Therefore the injector system plays a vital role during supersonic combustion as it shapes the profile of the extent with which the fuel and air mix downstream of the burner. The burner when operating in the subsonic mode, establishes a thermal throat where the flow passes through the sonic point and becomes supersonic downstream. The thermal throat location depends on the fueling condition and the burner geometry. It is to be noted that at higher Mach numbers the heat addition process causes higher total pressure losses which affects the overall thermodynamic cycle of the engine.

2.4 Single Expansion Ramp Nozzle

The nozzle expands the hot gases from the burner and accelerates the flow to produce thrust. The total pressure losses caused in the compression and combustion process shapes the nozzle exit area (usually larger than the inlet capture area) for matched pressure expansion. This can be seen in Figure 2-1. The single expansion ramp nozzle (SERN) consist of a ramp and a cowl. At on-design condition the expansion waves originating from the nozzle entrance reflects on the cowl and eventually gets cancelled on the ramp side (Figure 2-1) matching the ambient external pressure. The SERN operating at off-design conditions can be either over expanded or under-expanded depending on the external pressure. The SERN adapts the expansion process at off-design providing a better performance than a closed nozzle.

2.5 Literature Review

Reduced order modelling of the SCRamjet engine is an important aspect of its initial design phase. It is intended to put the designers in a ball park from where higher fidelity analysis or experimental work can be carried out. A number of efforts has been

made to analyze SCRamjet at its design point for example stream-thrust model by Heiser and Pratt [25], however off-design reduced order modelling are limited.

The analysis of the burner using quasi-one dimensional flow is a classic example of both on-design and off-design analysis which is presented with different levels of detailing. For example Heiser and Pratt [25] provides a single Mach number based ODE which is integrated assuming the flow is calorically perfect, whereas some existing advanced models account for calorically imperfect flow such as the one proposed by Doolan [12] or Surzhikov [19].

Although the on-design reduced order models for inlet and nozzles are abundant for example using calorically perfect shock relations for inlet [25] or method of characteristics for nozzle [25], the number of reduced order models for inlet and nozzle off-design analysis remains limited. A notable work which presented reduced order models for inlet and nozzles at both on-design and off-design was carried out by Dalle [13]. An isolator model with zero-dimensional fidelity is presented by Heiser and Pratt [25].

The current research work aims to provide an improved reduced order model for a complete dual model SCRamjet analysis using MATLAB [27] platform. It aims to provide the flexibility to simulate a dual mode SCRamjet at on-design and off-design with parametrized geometry.

Chapter 3

Physics of High Speed Gas Flows

The laws governing the nature of gas flows comprise of conservation of mass, momentum and energy. These laws are valid under conditions which devoid of nuclear reaction or objects with relative velocities near the speed of light. The current work excludes these special scenarios and the laws of conservation of mass, energy and momentum are perfectly valid. The study of aerodynamics integrates these laws to represent the behavior of continuum of gases with engineering approximations. However some approximations made for low speed gas flows are not valid for high speed gas flows. This chapter introduces some standard techniques to mathematically model high speed gas flows.

3.1 Review of Thermodynamics

Subject of thermodynamics introduces conservation of energy and natural tendency or direction of nature's process by defining state variables and path variables [23]. In this chapter the first and the second law of thermodynamics are discussed skipping the zeroth law [23].

The first law of thermodynamics states that "*there exists for every thermodynamic system a property called the energy. The change in energy is equal to the heat added to the system plus the mechanical work done on the system*". Mathematically we introduce the energy of the system as E, which is a state variable, and the heat added to the system as δQ and the work done on the system as δW, which are path variables. Then the first law of thermodynamics can be mathematically represented by equation (3.1) as follows.

$$dE = \delta Q + \delta W \tag{3.1}$$

The second law of thermodynamics states that "*there exits for every thermodynamic system in equilibrium an extensive scalar property called entropy S, such that in an reversible change of state of the system, $dS = (dQ)_{rev}/T$ where T is the absolute temperature and $(dQ)_{rev}$ is the reversible amount of heat received by the system. The entropy of thermally insulated system cannot decrease and is constant if only if the all processes are reversible*". Mathematically we state the second law using equation (3.2). For an irreversible process $(dQ)_{rev}$ indicates equivalent reversible heat addition to get the same entropy change. Also, the change in entropy due to irreversibility is always greater than zero ($dS_{irrev} > 0$) and is equal to zero for a reversible process.

$$dS = \frac{(dQ)_{rev}}{T} = \frac{\delta Q}{T} + dS_{irrev} \tag{3.2}$$

The next step is to introduce a group of state variables which allows us to solve energy conservation in a gas flow process. The term dE introduced in equation (3.1) represents the change in internal energy of the system which comprises of change in kinetic and potential energy of all the elementary particles making up the system. Along with the internal energy to capture potential work that can be extracted from current state, we introduce another state variable termed as enthalpy H which is defined in equation (3.3).

$$H = E + p\forall \tag{3.3}$$

The state variables p and $\forall$ represents pressure and volume of the system. A more convenient form for propulsion analysis is to represent them in specific quantities or per unit mass of the system. The specific internal energy (e) and enthalpy (h) can be related using equation (3.4) with ρ as mass density of the system which is also a state variable.

$$h = e + \frac{p}{\rho} \tag{3.4}$$

To provide an insight into the change in entropy caused due irreversibility (dS_{irrev}), we introduce a state variable called Gibbs free energy in equation (3.5). This variable will be particularly useful in estimating thermodynamics properties at chemical equilibrium.

$$G \equiv H - TS \tag{3.5}$$

3.2 Characterization of Gas

Gas is a state of matter in which the molecules comprising the gas are constantly in a state of random motion. This random motion from kinetic theory of gases [23] allows us to build a relationship between state variables such as pressure, density and temperature. The quantity temperature measures the scale of internal energy of the system. A brief discussion linking pressure, density and temperature is carried out in section 3.2.1.

3.2.1 Real and Ideal Gases

The gases in which the intermolecular forces play a significant role during intermolecular collisions are denoted as real gasses. If the intermolecular force does not play a significant role then the gases are defined to be an ideal gas. The ideal gas relationship that links pressure, temperature and density from kinetic theory of gases is given in equation (3.6).

$$p = \frac{\rho R_{univ} T}{\mathcal{M}} \tag{3.6}$$

The constant $R_{univ} = 8.314$ [J/kg-mol] is the universal gas constant, M_w is the molecular mass. For a real gas the compressibility factor (Z) is introduced making the modified state equation as $p = Z\rho RT$, where R is the gas constant given by $R_{univ}/\mathcal{M}$. The compressibility factor $Z(p,T)$ can be computed using viral coefficients. In the current study focused on air-breathing propulsion, the highest static pressure is expected to be 100atm and lowest static temperature associated with atmosphere is 217K. Within this range it can

be seen that the compressibility factor Z remains close to unity [23]. This allows us to approximate gas to an ideal gas behavior [23].

3.2.2 Specific Heat Capacities and Classification of Gases

Temperature is a measurable quantity which scales with static internal energy. To develop an explicit relationship between them we begin by defining specific internal energy (e) as the sum of random translational kinetic energy (e_{trans}), rotational kinetic energy (e_{rot}), vibrational energy (e_{vib}), electronic energy (e_{elec}) and the reference energy (e^0) of all the individual molecules in the system considered per unit mass.

$$e = e_{trans} + e_{rot} + e_{vib} + e_{elec} + e^0$$

The distribution of energy into each of the modes is governed by statistical law of thermodynamics [23] which provides an explicit relation between internal energy and temperature in equation (3.7). The number of rotational degrees of freedom is given by f_{rot} and rest of the symbols carry standard meaning in equation (3.7). It is to be noted that during a chemical reaction or excitation process e_{elec} and R become functions of both pressure and temperature.

$$e = \frac{3}{2}RT\Big)_{trans} + \frac{f_{rot}}{2}RT\Big)_{rot} + \frac{h\upsilon/kT}{e^{h\upsilon/kT}-1}RT\Big)_{vib} + e_{elec} + e^0 \qquad (3.7)$$

With the explicit relationship between e and T the specific heat capacity can be introduced which represents sensitivity with which specific heat content varies with temperature. This is done by defining specific heat capacities at constant pressure (c_p) and at constant volume (c_v) in equations (3.8, 3.9). In general both c_p and c_v depend on temperature, pressure and type of gas. Their ratio holds a particular importance in gas dynamics and it is given by $\gamma = c_p/c_v$.

$$c_p = \left(\frac{\delta q}{dT}\right)_p = \left(\frac{\partial h}{\partial T}\right)_p \qquad (3.8)$$

$$c_v = \left(\frac{\delta q}{dT}\right)_v = \left(\frac{\partial e}{\partial T}\right)_v \tag{3.9}$$

When the specific heat capacities are invariant of pressure and temperature, the gas is said to be calorically perfect gas (CPG). Air which is mainly a mixture of nitrogen and oxygen behaves calorically perfect until temperatures are about 800K. Once the temperature of the air exceeds 800K, the distribution trends of internal energy at quantum level changes causing the variation of specific heats as shown in Figure 3-1.

When the specific heat capacities depend only on temperature then the gas is said to be a thermally perfect gas (TPG). Air above 800K behaves as a thermally perfect gas and it can be treated like an equivalent one species gas in both CPG and TPG regimes.

Approximately beyond 1500K the air becomes chemically reactive where the concentrations of individual species depend on pressure and temperature making c_p and c_v function of both pressure and temperature. This can be seen in Figure 3-1 where the bifurcation of c_p with pressure is observed at approximately 1500K.

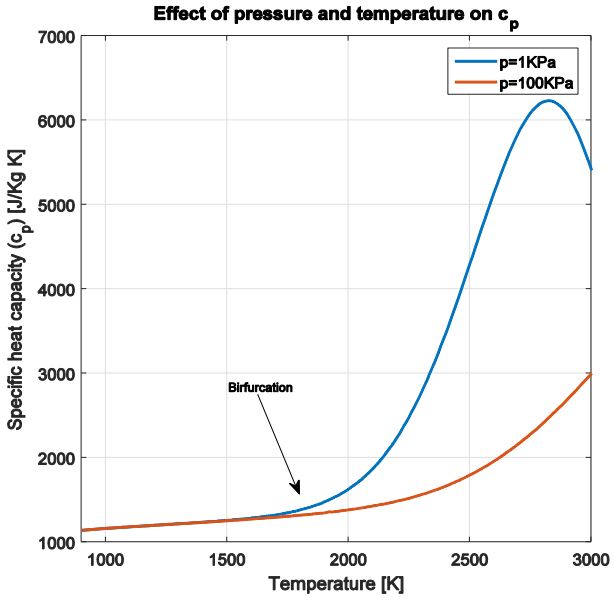

Figure 3-1: Variation of c_p of air with temperature and pressure.

3.3 Chemically Reacting Gases in Equilibrium

High speed gas flows are associated with high temperatures during re-entry of atmosphere by ballistic projectiles or during supersonic flight when subjected to shockwaves or combustion processes. Under these circumstances the air heats up considerably and becomes chemically reactive. In the scope of the current work, gases are assumed to be in chemical equilibrium and their mixture properties are used to calculate aerothermodynamic properties of the flow. However it is important to note that the actual physical process in nature involves non-equilibrium processes but the justification for equilibrium assumption will made at a later stage.

Consider air which is approximately 80% N_2 and 20% O_2 by moles at room temperature. But when temperature of air goes up considerably beyond >2000K, the air becomes a mixture of O_2, O, N_2, N and NO. To represent the concentration of these species we use mass fraction Y_k which is defined as mass of the species 'k' per unit mass of the mixture. Similarly we define mole fraction as X_k which represents moles of species 'k' in a unit mole of mixture. Once these fractions are known then it is possible to calculate thermochemical and transport properties of the mixture.

3.3.1 Chemical Equilibrium

Chemical equilibrium of species essentially means the rate of formation of each species is equal to rate of depletion of each species. At constant temperature and pressure a unique equilibrium concentration of species exist. To compute this concentration it is required to have thermodynamic equilibrium where there is no change in entropy due to irreversibility ($dS_{irrev} = 0$). From equations (3.2, 3.3, 3.5) the following equation (3.10) can be derived by considering change in state variables.

$$dG = -SdT + \forall dp - TdS_{irrev} \tag{3.10}$$

For chemical equilibrium at constant temperature ($dT = 0$), constant pressure ($dp = 0$) and with the condition $dS_{irrev} = 0$, we can see that equation (3.10) reduces to $(dG)_{T,p} = 0$. Therefore the condition $(dG)_{T,p} = 0$ essentially represents the minima of Gibbs free function G of a mixture as shown in equation (3.11).

$$G = \sum_{k=1}^{N} n_k \left(G_k^0 + RT \ln\left(\frac{p_k}{p_0}\right)\right) \tag{3.11}$$

$$G_k^0(T, p_0 = 1atm) = H^0(T) - TS^0(T, p_0 = 1atm) \tag{3.12}$$

The term G_k^0 is the standard state [Gibbs free energy for individual species which can be obtained from equation (3.12) where the enthalpy $H^0(T)$ and entropy $S^0(T)$ at standard state ($p_0 = 1atm$) are calculated from NASA polynomials [10] as a function of temperature alone. The pressure p_k is the partial pressure (atm) of each species and n_k represents the number of moles of each species. Therefore finding equilibrium requires minimization of Gibbs free energy with atom balance constraint. In the interest of current work to solve combustion chemistry for high speed propulsion systems involving hydrogen and air, the method of solution to find equilibrium is discussed here in detail.

Consider the following chemical reaction between hydrogen and air.

$$\phi H_2 + \frac{1}{2}\left(O_2 + \frac{79}{21}N_2\right) \longrightarrow n_{H_2O}H_2O + n_{N_2}N_2 + n_{O_2}O_2 + n_{NO}NO + n_{H_2}H_2 + n_H H + n_O O + n_{OH}OH$$

The right hand side of the chemical reaction indicates significant product species which are in chemical equilibrium with each other. By evaluating G_k^0 of species, the Gibbs free energy of the mixture from equation (3.11) can be minimized by appropriate values for species mole n_k with atom balance constraint. The atom balance of N, O and H in the chemical reaction between reactants and products can be written in matrix form as following:

$$\begin{bmatrix} 2 & 0 & 0 & 2 & 1 & 1 & 0 & 0 & 0 \\ 0 & 0 & 2 & 1 & 1 & 0 & 1 & 0 & 1 \\ 0 & 2 & 0 & 0 & 0 & 0 & 0 & 1 & 1 \end{bmatrix} \begin{bmatrix} n_{H_2} \\ n_{N_2} \\ n_{O_2} \\ n_{H_2O} \\ n_{OH} \\ n_H \\ n_O \\ n_N \\ n_{NO} \end{bmatrix} = \begin{bmatrix} 2\phi \\ 1 \\ 79/21 \end{bmatrix} \begin{matrix} H - Balance \\ O - Balance \\ N - Balance \end{matrix} \quad (3.13)$$

To perform minimization of the Gibbs function, the MATLAB optimization tool 'fmincon' [27] is used with global minimization function as equation (3.11) and constraint equation (3.13). By performing the minimization using 'interior point algorithm' [27] we get the number of moles of each species n_k from which the mass fraction Y_k can be determined using $Y_k = n_k\mathcal{M}_k/\sum n_k\mathcal{M}_k$ and mole fraction X_k using $X_k = n_k/\sum n_k$. It can now be concluded that equilibrium species concentration Y_k or n_k are functions of the pressure p, temperature T and equivalence ratio ϕ.

3.3.2 Thermochemical Properties of Mixture

The state variables are usually measured from a reference state (different from standard state). Here we consider the reference state as $p^0 = 1$[atm] and $T^0 = 298.15$[K] which is consistent with NASA polynomial [10] data. Let us now define the specific enthalpy of mixture with N species as following.

$$h = \sum_{k=1}^{N} Y_k h_k \quad (3.14)$$

$$h_k = \int_{T^0}^{T} c_{pk} dT + \Delta_f^0 h_k \quad (3.15)$$

The specific enthalpy of individual species h_k is sum of sensible enthalpy and the formation enthalpy at reference state $\Delta_f^0 h$. The sensible enthalpy is enthalpy above the reference state which is defined by only the integral part in the equation (3.15). The specific internal energy of the mixture is defined in equation (3.16).The species specific internal energy e_k

carries a similar definition to h_k and defined as sum of sensible internal energy and internal energy at reference state e_k^0.

$$e = \sum_{k=1}^{N} Y_k e_k \tag{3.16}$$

$$e_k = \int_{T^0}^{T} c_{vk} dT + e_k^0 \tag{3.17}$$

To build the relationship between reference enthalpy $\Delta_f^0 h_k$ and internal energy e_k^0, we apply equations (3.4, 3.6) at reference conditions which gives us $e_k^0 = \Delta_f^0 h - RT^0$. The equilibrium mixture enthalpy h can now be computed from equation (3.14) by first evaluating the mass fraction $Y_k(p, T, \phi)$ using minimization of Gibbs free energy and then evaluating individual species enthalpy h_k from NASA polynomials [10] which are an explicit function of temperature. The mixture gas constant is given by $R = R_{univ}/\mathcal{M}$, where the mixture molecular mass $\mathcal{M} = 1/\sum(Y_k/\mathcal{M}_k)$. Once the mixture molecular mass and enthalpy is known the mixture internal energy can be given by $e = h - RT$.

To evaluate the mixture specific heat capacities given in equations (3.18, 3.19) the numerical partial derivative with respect to temperature is computed using central difference scheme. The heat capacities are computed as follows.

$$c_p = \left(\frac{\partial h}{\partial T}\right)_{p,\phi} \approx \frac{h(p, T + \Delta T, \phi) - h(p, T - \Delta T, \phi)}{2\Delta T} \tag{3.18}$$

$$c_v = \left(\frac{\partial e}{\partial T}\right)_{v,\phi} \approx \frac{e(p + \rho\bar{R}\Delta T, T + \Delta T, \phi) - e(p - \rho\bar{R}\Delta T, T - \Delta T, \phi)}{2\Delta T} \tag{3.19}$$

Although the mixture properties in general depend on two other state variable, the individual species gas properties depends only on one state variable behaving as a TPG and follow Dalton's law of partial pressure [23].

3.4 Boundary Layer and Heat Transfer

Hypersonic flights are associated with high temperature flows along the walls of the vehicle where viscous effects dominate the inertial effects, causing thick boundary layers to grow [23]. Therefore it is important to study the boundary layer flow in a high speed flight, particularly the phenomenon of transition from laminar boundary layers to turbulent boundary layer becomes very important.

In the scope of the current work we study the boundary layer and associated heat transfer from an engineering perspective using basic results of boundary layer over a flat plate [23]. Let us first consider a qualitative description of boundary layer growth over a flat plate.

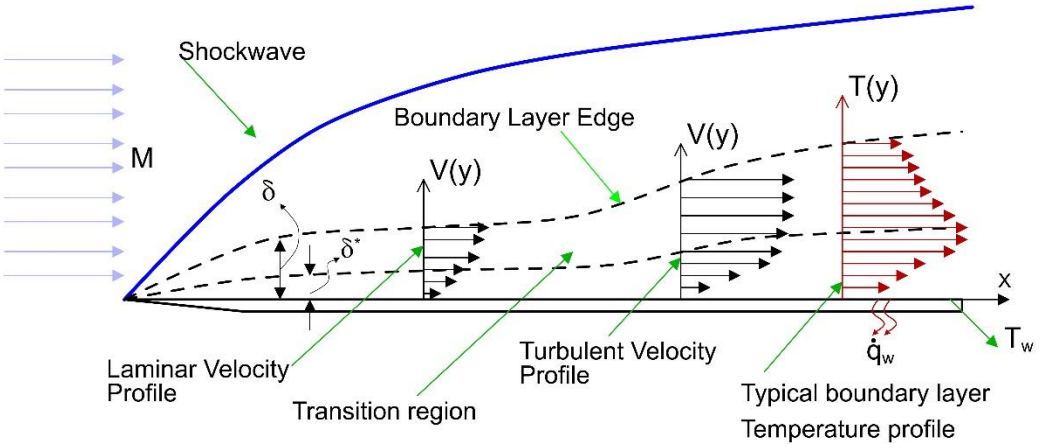

Figure 3-2: Characterization of supersonic flow over flat plate.

The flow over flat plate is characterized with the boundary layer growth with thickness $\delta(x)$ across which velocity and temperature varies appreciably as depicted in Figure 3-2. The displacement thickness [23, 24] $\delta^*(x)$ represents mass deficient region in an equivalent inviscid flow across the plate. The trace of $\delta^*(x)$ acts as a pseudo compression surface which creates the fore shockwave. Another important variable in the boundary layer is the temperature. The slope of the temperature at the wall drives the

amount of heat flux ($\dot{q_w}$) that occurs into the surface. The study of heat transfer in hypersonic boundary layer is essential to choose the right materials which can withstand the thermal loads in a high speed flight.

Before we start analyzing the boundary layer let us introduce some non-dimensional numbers such as Reynolds number (Re), skin friction coefficient (c_f), Stanton number (C_H) and Prandtl number (Pr) in equations (3.20-3.23). The subscript 'e' represents the conditions at the edge of the boundary layer, h_w and h_{aw} represents the wall enthalpy and adiabatic wall enthalpy respectively, L_{char} represents characteristic length and the rest of the symbols carry standard meaning.

$$Re = \frac{\rho_e u_e L_{char}}{\mu} \tag{3.20}$$

$$c_f = \frac{\tau_w}{\frac{1}{2}\rho_e u_e^2} \tag{3.21}$$

$$C_H = \frac{\dot{q_w}}{\rho_e u_e (h_{aw} - h_w)} \tag{3.22}$$

$$Pr = \frac{\mu c_p}{k} \tag{3.23}$$

Although a hypersonic vehicle is not exactly a flat plate, we use some of the results from flat plate boundary analysis [23] to predict the skin friction and heat transfer on the walls of the vehicle. First, to identify whether the boundary layer flow is laminar or turbulent we consider a Reynolds number based criteria [23] detailed in equation (3.24). This criteria uses an empirical correlation based on flow over a cone [23] which can be applied to waverider configuration [23]. If the Reynolds number exceeds the transition Reynolds number Re_T then the flow is considered turbulent.

$$\log_{10} Re_T = 6.421 \exp(1.209 \times 10^{-4} M_e^{2.641}) \tag{3.24}$$

An engineering approach to compute the skin friction and heat transfer detailed by Anderson [23] called the reference temperature method is used in the current work. This method provides a technique to evaluate the skin friction and heat transfer coefficients for a compressible boundary layer by utilizing incompressible boundary layer theory with thermodynamic and transport properties evaluated at a representative temperature value (T^*) inside the boundary layer. At first the Reynolds number at the edge of the boundary layer ($Re_{e,x}$) is evaluated and compared with Re_T to determine whether the flow is turbulent ($Re_{e,x} \geq Re_T$) or laminar ($Re_{e,x} < Re_T$). Once the nature of flow is determined the reference temperature is defined using the Meador-Smart method [41] detailed in equation (3.25).

$$T^* = \begin{cases} 0.45T_e + 0.55T_w + \dfrac{0.16r(\gamma-1)T_e}{2}M_e^2, & Re_{e,x} < Re_T \\ 0.50T_e + 0.50T_w + \dfrac{0.16r(\gamma-1)T_e}{2}M_e^2, & Re_{e,x} \geq Re_T \end{cases} \tag{3.25}$$

The recovery factor (r) is defined as $r = (h_{aw} - h_e)/(h_{te} - h_e)$ and can be related to the Prandtl number (Pr) using equation (3.26) [23]. For compressible flows generally Prandtl number taken as a constant $Pr = 0.715$ [23] with no more than 3% error between the temperature range $300 < T^* < 2000$.

$$r = \begin{cases} Pr^{1/2}, & Re_{e,x} < Re_T \\ Pr^{1/3}, & Re_{e,x} \geq Re_T \end{cases} \tag{3.26}$$

As pressure across the boundary layer is fairly constant, the corresponding reference density using state relation is given by $\rho^* = \rho_e T_e/T^*$ and the corresponding Reynolds number at a distance x from the nose can be calculated using $Re^*_{e,x} = \rho^* u_e x/\mu^*$. The estimation of viscosity μ^* is detailed in section 3.4.1. Using $Re^*_{e,x}$ the skin friction at a distance x from the nose can be defined using equation (3.27). Note that the wall stress is given by $\tau_w = \rho^* u_e^2 c_f/2$ when reference temperature method is used.

$$c_f = \begin{cases} \dfrac{0.664}{\left(Re^*_{e,x}\right)^{0.5}}, & Re_{e,x} < Re_T \\ \dfrac{0.02296}{\left(Re^*_{e,x}\right)^{0.139}}, & Re_{e,x} \geq Re_T \end{cases} \tag{3.27}$$

The Stanton number or the heat transfer coefficient C_H is defined using Reynolds analogy factor R_f and c_f as follows.

$$C_H = \frac{c_f R_f}{2} \tag{3.28}$$

The Reynolds analogy factor R_f for a flat plat laminar and turbulent flow is given by equation (3.29). At far downstream it is to be noted that $C_H \sim c_f$.

$$R_f = \begin{cases} Pr^{-\frac{2}{3}}, & Re_{e,x} < Re_T \\ Pr^{-\frac{1}{3}}, & Re_{e,x} \geq Re_T \end{cases} \tag{3.29}$$

The boundary layer thickness (δ), momentum thickness (θ_m) and displacement thickness (δ^*) from Blasius flat plate solution [23] using reference temperature method is detailed in equation (3.30-3.32).

$$\delta = \begin{cases} \dfrac{4.91\,x}{(Re^*_x)^{0.5}}, & Re_x < Re_T\ (Laminar) \\ \dfrac{0.37\,x}{(Re^*_x)^{0.2}}, & Re_x \geq Re_T\ (Turbulent) \end{cases} \tag{3.30}$$

$$\theta_m = \begin{cases} \dfrac{0.664\,x}{(Re^*_x)^{0.5}}, & Re_x < Re_T\ (Laminar) \\ \dfrac{0.037\,x}{(Re^*_x)^{0.2}}, & Re_x \geq Re_T\ (Turbulent) \end{cases} \tag{3.31}$$

$$\delta^* = \begin{cases} \dfrac{1.72\,x}{(Re^*_x)^{0.5}}, & Re_x < Re_T\ (Laminar) \\ \dfrac{0.048\,x}{(Re^*_x)^{0.2}}, & Re_x \geq Re_T\ (Turbulent) \end{cases} \tag{3.32}$$

The method of predicting heat transfer coefficient C_H and skin friction coefficient c_f presented in this section is only from an engineering perspective but is subjected to limitations [23].

3.4.1 Estimating Viscosity

To complete the discussion on boundary layers it is required to discuss the evaluation of viscosity at a given reference condition say $T = T^*$ and $p = p^*$. For thermally perfect regime of the air where no chemical reactions takes place, Sutherland's law can be used for evaluating the viscosity which is expressed as an explicit function of temperature T[K] given in equation (3.33). The constants are given by $\mu_{ref} = 1.789 \times 10^{-5}$[kg/m s], $T_{ref} = 288$[K], and $S = 110$K.

$$\mu = \mu_{ref}\left(\frac{T}{T_{ref}}\right)^{\frac{3}{2}}\frac{T_{ref} + S}{T + S} \tag{3.33}$$

To compute the viscosity of a mixture Wilke's [8] procedure is used. The viscosity of a mixture in equilibrium at a given pressure p and temperature T is given by equation (3.34), where the term $\emptyset_{ij}$ is a dimensionless constant defined in equation (3.35)

$$\mu_{mix} = \sum_{i=1}^{N}\frac{\mu_i}{1 + \frac{1}{X_i}\sum_{\substack{j=1 \\ j\neq i}}^{j=N} X_j \emptyset_{ij}} \tag{3.34}$$

$$\emptyset_{ij} = \frac{\left(1 + \left(\mu_i/\mu_j\right)^{\frac{1}{2}}\left(\mathcal{M}_j/\mathcal{M}_i\right)^{\frac{1}{4}}\right)^2}{\left(\frac{4}{\sqrt{2}}\right)\left(1 + \mathcal{M}_i/\mathcal{M}_j\right)^{\frac{1}{2}}} \tag{3.35}$$

The individual viscosity μ_i is obtained from NASA transport properties coefficient [10] which is purely a function of temperature. The mole fraction X_i is a function of both pressure and temperature making the μ_{mix} function of both pressure and temperature.

3.5 Governing Equations for Gas flows

In the current work the integral form of equations governing the gas flows are discussed. Consider a control volume in Eulerian reference frame (or fixed in space, inertial reference frame) [26] in Figure 3-3.

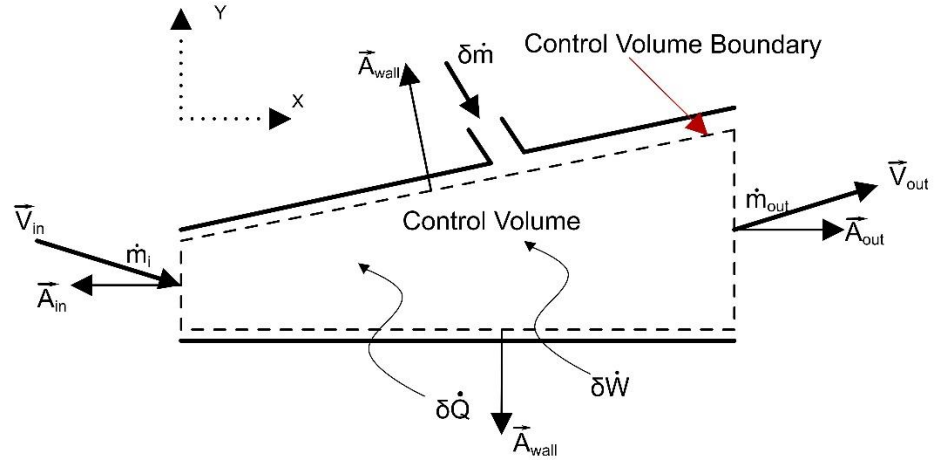

Figure 3-3: Schematic diagram of control volume in a typical internal flow.

3.5.1 Mass Conservation

The mass conservation equation conveys that mass can neither be created nor be destroyed. Therefore the rate of accumulation of mass inside a control volume should be equal to the difference of rate of mass flowing in and out. This can be represented in a mathematical equation as follows.

$$\frac{\partial}{\partial t}\left(\iiint \rho d\forall\right) + \iint \rho \boldsymbol{V} \cdot d\boldsymbol{A} = 0 \tag{3.36}$$

The area vector $d\boldsymbol{A}$ is given by $d\boldsymbol{A} = \boldsymbol{n}dA$ with vector $\boldsymbol{n}$ being the unit outward normal along the surface enclosing the control volume and dA being the magnitude.

3.5.2 Momentum Conservation

Newton's second law states that "*the sum of the external force acting on a body is equal to its rate of change of momentum observed from an inertial reference frame*". When

Newton's second law is applied to the gas flows inside a control volume it can be mathematically represented in vectorial form as following.

$$\frac{\partial}{\partial t}\left(\iiint \rho \boldsymbol{V} d\forall\right) + \oiint \rho(\boldsymbol{V}\cdot d\boldsymbol{A})\boldsymbol{V} = -\oiint p d\boldsymbol{A} + \iint d\boldsymbol{F_s} + \iiint \rho \boldsymbol{f_b} d\forall \qquad (3.37)$$

The left hand side of equation (3.37) represents the total rate of momentum change inside the control volume and the right hand side specifies the cause of this change which arise due to pressure p, surface force $\boldsymbol{F_s}$ and body forces per unit mass $\boldsymbol{f_b}$.

3.5.3 Energy Conservation

The conservation of energy which was discussed in section 3.1 as first law of thermodynamics is applied for total quantities which includes the kinetic energy of the flow along with static internal energy. The integral form of energy equation is presented in equation (3.38) which conserves total specific internal energy (e_t) inside the control volume defined as $e_t = e + \frac{V^2}{2}$.

$$\begin{aligned}\frac{\partial}{\partial t}\left(\iiint \rho e_t d\forall\right) + \oiint \rho e_t \boldsymbol{V}\cdot d\boldsymbol{A} \\ = -\oiint p\boldsymbol{V}\cdot\boldsymbol{dA} + \iint \boldsymbol{V}\cdot d\boldsymbol{F_s} + \iiint \rho \boldsymbol{f_b}\cdot\boldsymbol{V} d\forall \\ + \dot{W}_{shaft} - \iint \dot{\boldsymbol{q}}_{\boldsymbol{flux}}\cdot d\boldsymbol{A} + \iiint \rho \dot{q}_{vol} d\forall\end{aligned} \qquad (3.38)$$

The heat can be added to the control volume through heat flux ($\dot{\boldsymbol{q}}_{\boldsymbol{flux}}$) or volumetric heat addition per unit mass ($\dot{q}_{vol}$). The work on the control volume is done by the forces acting on it and work done by shaft $\dot{W}_{shaft}$. It is important to note that different forms of energy equation can be written making use of total enthalpy, or static enthalpy, or static internal energy but all represent the first law of thermodynamics.

In the current work as the SCRamjet is analyzed for steady operation, the governing equations used are time-independent equations. Therefore the conservation

equations (3.36-3.38) in steady state form appropriate for SCRamjet analysis are reduced to equations (3.39-3.40), where the work due to shaft doesn't exist and work due to surface forces (typically viscous forces) are neglected [28] due to high total enthalpy of the flow.

$$\oiint \rho \boldsymbol{V} \cdot d\boldsymbol{A} = 0 \tag{3.39}$$

$$\oiint \rho(\boldsymbol{V} \cdot d\boldsymbol{A})\boldsymbol{V} = -\oiint p d\boldsymbol{A} + \iint d\boldsymbol{F_s} + \oiiint \rho \boldsymbol{f_b} d\forall \tag{3.40}$$

$$\oiint \rho e_t \boldsymbol{V} \cdot d\boldsymbol{A} = -\oiint p\boldsymbol{V} \cdot \boldsymbol{dA} + \oiiint \rho \boldsymbol{f_b} \cdot \boldsymbol{V} d\forall - \iint \dot{\boldsymbol{q}}_{\boldsymbol{flux}} \cdot d\boldsymbol{A} + \oiiint \rho \dot{q}_{vol} d\forall \tag{3.41}$$

Along with the equations (3.39-3.41), to obtain closed form of solution, the state relationship is used by incorporating equation (3.6).

Chapter 4

Dual Mode SCRamjet Analytical Model

An analytical model for investigating steady operation of the Dual Mode SCRamjet (DMSJ) is presented in this chapter. The model hopes to reduce analysis complexity and duration to carry out parametric sweep studies of geometry and flight conditions. Carrying out such fast parametric studies at on-design and off design conditions are of particular interest at the initial design phase of a high speed propulsion system. Using different levels of fidelity, the DMSJ is analyzed by keeping the characterization of flow field as close as possible to real physical phenomena. The DMSJ model is broken down into five sub-models namely; inlet, isolator, fuel injector, burner and single expansion ramp nozzle. Each of the individual sub-models are carefully stitched together to mimic the SCRamjet operation at different design and off-design conditions. The analytical model presented here is for a specific parametrized geometry which covers a wide range of typical designed flow paths for experimentation and flight test.

4.1 Parametrized SCRamjet Geometry

The framework to construct the analytical model for SCRamjet is built on the foundation of typical SCRamjet 2D cross-section. The cross-section is parametrized to capture different possible configurations as shown in Figure 4-1. The SCRamjet's third dimension is assumed to be prismatic extrusion of the parametrized cross-section in Figure 4-1 with engine depth d_z.

A right handed Cartesian co-ordinate reference frame is defined along the body axis denoted by [X_{BODY},Y_{BODY}]. This frame is the global reference frame used in the current study while a local reference frame is defined along the burner axis called [X_{BURN},Y_{BURN}].

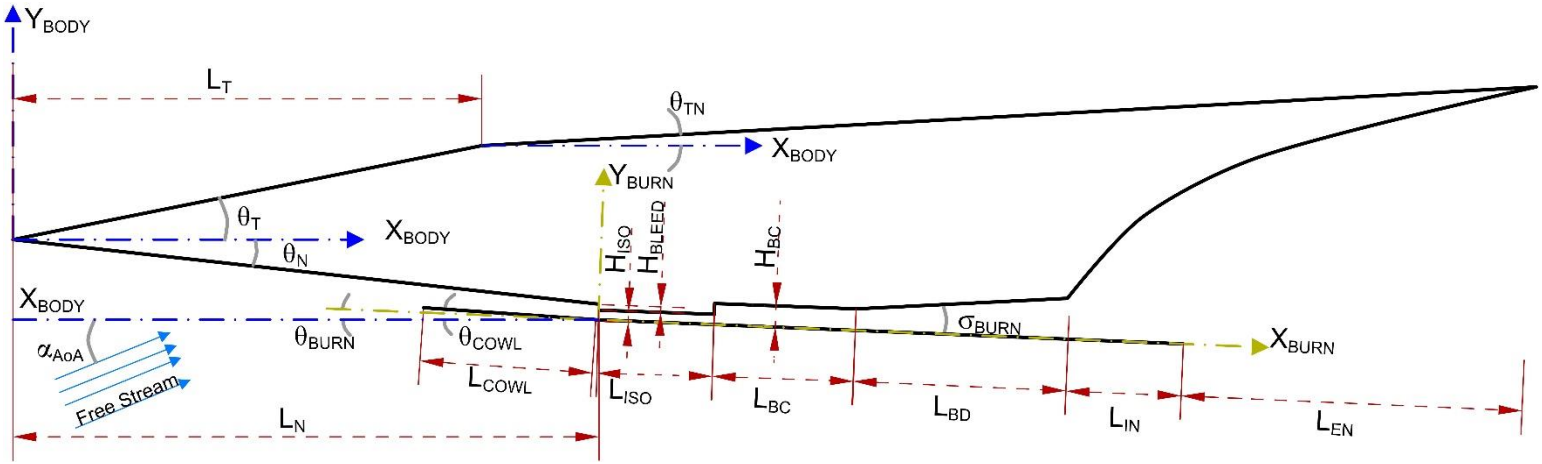

Figure 4-1: Parametrized 2D cross-section of SCRamjet.

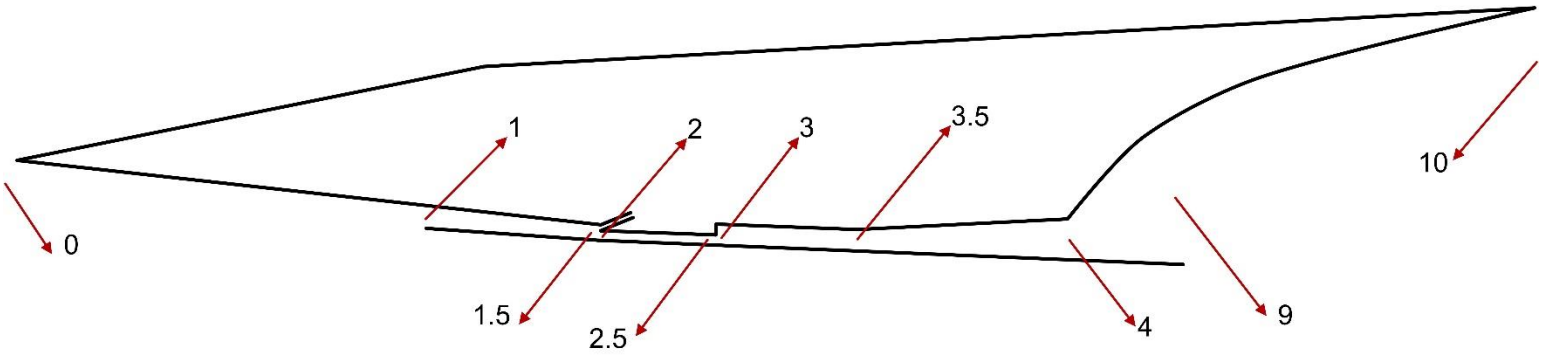

Figure 4-2: Station numbering of SCRamjet.

From Figure 4-1 it can be seen that the inlet consist of single ramp which is inclined at an angle θ_N with respect to X_{BODY}. The cowl of the engine inlet is oriented at an angle θ_{COWL} with respect to X_{BODY}. The rest of the flow path which includes isolator, burner and nozzle are oriented along the burner axis [X_{BURN},Y_{BURN}]. The burner X-axis [X_{BURN}] is inclined at an angle of θ_{BURN} with respect to X_{BODY}. It is assumed that a bleed exist near the entrance of isolator with bleed height H_{BLEED}. The burner is divided into two regions, a constant area burner with length L_{BC} followed by a diverging area burner with length L_{BD}. The diverging area burner has a wall slope of $\tan(\sigma_{BURN})$ with resepect to the local co-ordinate axis [X_{BURN}]. The nozzle is split into two parts, namely; internal nozzle and external nozzle. The internal nozzle has an axial length of L_{IN} and the external nozzle has L_{EN} measured from burner axis. The rest of the geometrical parameters can be interpreted from Figure 4-1. Note that the all the dimensions measured from global co-ordinates shown in Figure 4-1 are positive, any measurement made in the opposite sense is taken as a negative quantity.

The station numbering of the engine is consistent with the method used by Heiser and Pratt [25]. Some additional stations are defined to help evaluate flow parameters at important locations. The station numbering of the engine is depicted in Figure 4-2.

4.2 Inlet Model

The flow process in a Dual Mode SCRamjet (DMSJ) inlet is dominated by a series of oblique shockwaves through which considerable variation in air temperature is observed. The temperature usually varies from 200K to 1500K inside a typical inlet making the air to behave as a thermally perfect gas (TPG). The inlet is analyzed by constructing the oblique shockwave reflections for a thermally perfect gas process. At first a thermally perfect flow process through an oblique shockwave is discussed.

4.2.1 Thermally Perfect Oblique and Normal Shockwaves

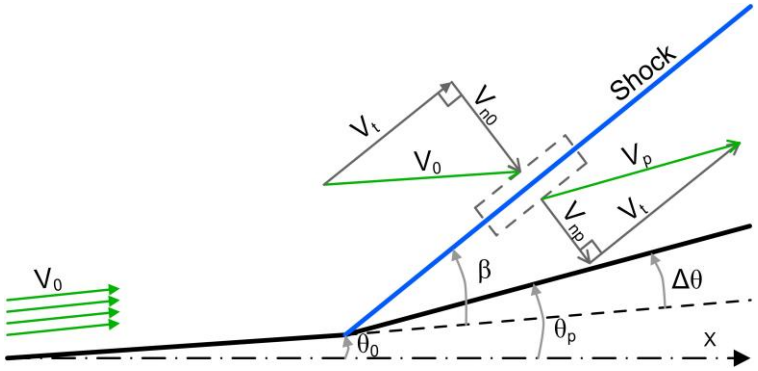

Figure 4-3: The schematic represents a supersonic flow over a wedge.

Consider the following schematic in Figure 4-3. The flow turns across the shock through an angle given by $\Delta\theta = \theta_p - \theta_0$. The subscript '0' is associated with upstream condition and 'p' with post shock condition. Across the shockwave a control volume is constructed and conservation equations for an inviscid adiabatic flow are applied by using equations (3.39-3.41). It is to be noted that the tangential component of the velocity (V_t) is conserved across the shock. The conservation equation with five variable can be reduced to one variable (β) governed by non-linear equation (4.1) as derived in Appendix A.

$$2\left(h_{t0} - \int_{T^0=298.15K}^{\sigma(\beta)} c_p dT\right)\cos^2(\beta - \Delta\theta) - V_0^2\cos^2(\beta) = 0 \qquad (4.1)$$

The integral term in equation (4.1) is evaluated using specific heat capacity as function of temperature given by:

$$\frac{c_p(T)}{R} = \sum_1^8 a(i)\, T^{i-2}$$

Where $a(1)$, $a(2)$ ... are coefficients for air detailed in Appendix A. The $\sigma(\beta)$ in the integral term in equation (4.1) is expressed in equation (4.2).

$$\sigma(\beta) = \left(\frac{RT_0 + V_0^2\sin^2(\beta)}{R\tan(\beta)}\right)\tan(\beta - \Delta\theta) - \frac{V_0^2\cos^2(\beta)\tan^2(\beta - \Delta\theta)}{R} \qquad (4.2)$$

It is to be noted that across an adiabatic shock, the total enthalpy h_t is conserved ($h_{t0} = h_{tp}$) and it can be evaluated as following:

$$h_{tp} = h_{t0} = \int_{T^0=298.15K}^{T_0} c_p dT + \frac{V_0^2}{2}$$

The shock angle β measured from the free-stream direction is solved from non-linear equation (4.1) for the weak-shock case using MATLAB inbuilt non-linear solver 'fsolve' [27]. Once the shock angle β is solved the remaining flow variables are obtained by back substitution using equations (4.3-4.8).

$$V_p = V_0 \cos(\beta)/\cos(\beta - \Delta\theta) \tag{4.3}$$

$$T_p = \sigma(\beta) \tag{4.4}$$

$$\gamma_p = c_p(T_p)/(c_p(T_p) - R) \tag{4.5}$$

$$M_p = V_p/\sqrt{\gamma_p R T_p} \tag{4.6}$$

$$\rho_p = \rho_0 \tan(\beta)/\tan(\beta - \Delta\theta) \tag{4.7}$$

$$p_p = \rho_p R T_p \tag{4.8}$$

Similar to the analysis of the oblique shock, the equations governing normal shock can be reduced to two non-linear simultaneous equations (4.9, 4.10) with unknowns (V_{np}, T_p).

$$RT_0 V_{np} + V_{n0}^2 V_{np} - RT_p V_{n0} - V_{np}^2\, V_{n0} = 0 \tag{4.9}$$

$$\frac{V_{np}^2}{2} - h_{t0} + \int_{T^0=298.15K}^{T_p} c_p dT = 0 \tag{4.10}$$

Upon evaluating V_{np} and T_p using MATLAB inbuilt non-linear solver 'fsolve', the remaining flow variables can be obtained by back substitution using equation (4.11-4.13).

$$p_p = (p_0 + \rho_0 V_{n0}^2) - \rho_0 V_{n0} V_{np} \tag{4.11}$$

$$\rho_p = \rho_0\, V_{n0}/V_{np} \tag{4.12}$$

$$M_{np} = V_{np}/\sqrt{\gamma_p R T_p} \tag{4.13}$$

4.2.2 Inlet Shock Reflection Model

The DMSJ inlet geometry considered in the current work consist of a single turning ramp with cowl (Figure 4-1). To analyze the inlet compression process, shock reflections are constructed using thermally perfect gas (TPG) analysis which provides 2D fidelity of the physical flow process. To understand the process of constructing the shock reflections, the analysis is split into two parts, namely; external compression and internal compression. The external compression is due to the fore shock arising at the nose of the inlet and the internal compression follows the external compression comprising of multiple shock reflections (Figure 4-4).

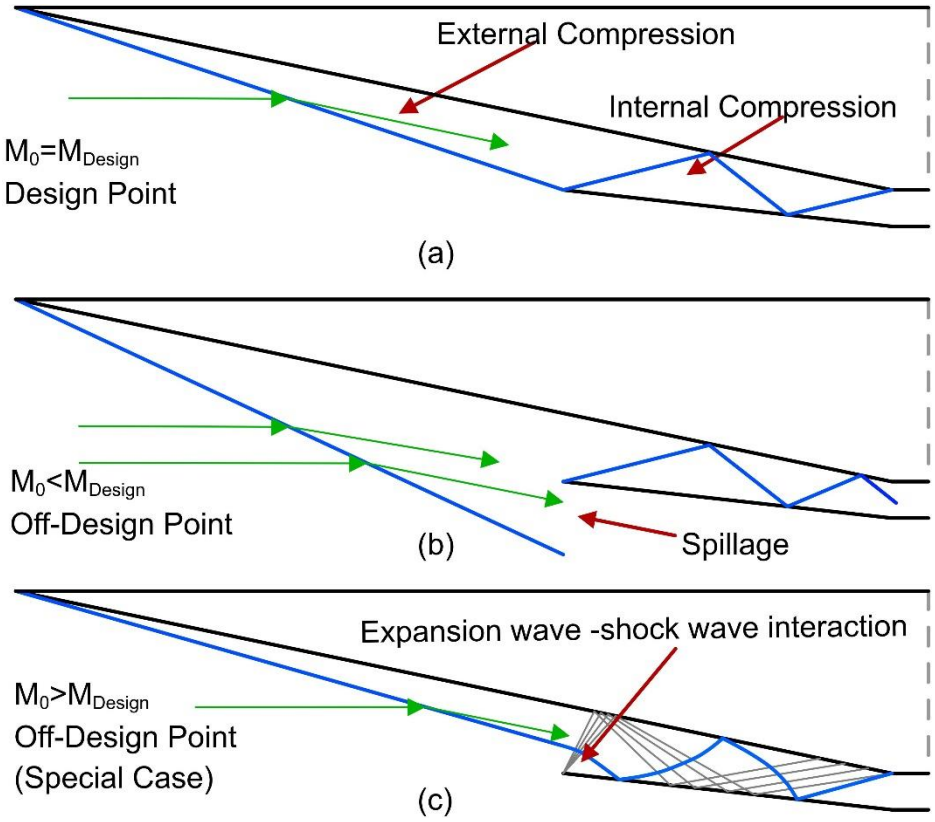

Figure 4-4: Schematic flow process of external and internal compression for: (a) On-design ($M_0 = M_{design}$) (b) Off-design ($M_0 < M_{design}$) (c) Special off-design ($M_0 > M_{design}$).

At the design point ($M_0 = M_{design}$), the fore-shock intersects the cowl lip (Figure 4-4 (a)), capturing maximum mass flow rate of the air. During off-design conditions ($M_0 < M_{design}$), the fore-shock is ahead of the cowl lip (Figure 4-4 (b)), causing spillage. Note that during on-design and off-design conditions, the cowl is completely submerged under the influence of the fore-shock. Special off design conditions are possible when $M_0 > M_{design}$ resulting in fore-shock being swallowed and the cowl being partially submerged under the influence of it (Figure 4-4 (c)).

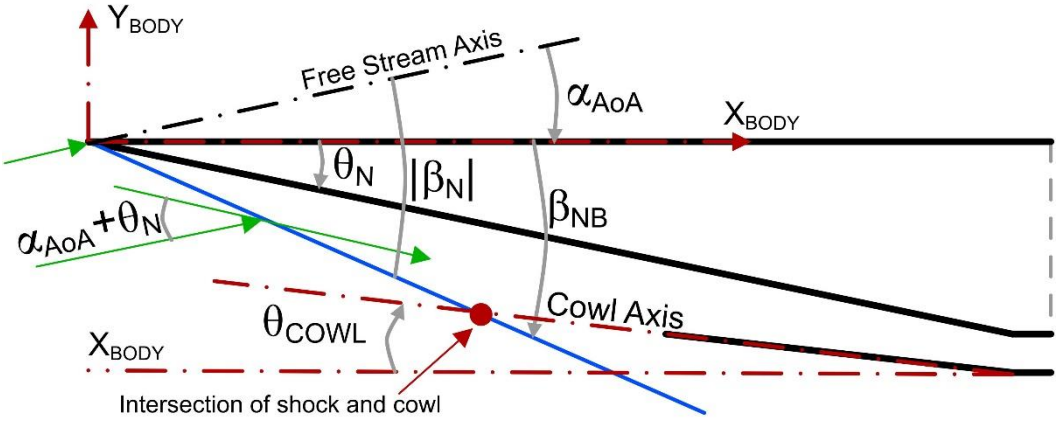

Figure 4-5: Schematic detailing of external compression and its geometrical parameters.

To start the inlet analysis consider Figure 4-5, the fore-shock with free stream Mach number M_0 is constructed with turn angle $\Delta\theta = \theta_N + \alpha_{AoA}$. Note that except the angle α_{AoA} which is measured from free-stream axis, all the other angles are measured from global co-ordinates. The corresponding post shock conditions are recorded. Note that both the turn angle ($\Delta\theta$) and shock angle ($|\beta_N|$) are positive quantities in the TPG shock calculation. The shock angle $|\beta_N|$ measured from free-stream is then mapped to global co-ordinates [X_{BODY},Y_{BODY}] which is at an angle β_{NB} with respect to the X-axis, and given by $\beta_{NB} = (|\beta_N| - \alpha_{AoA})$. Upon constructing the fore-shock in global coordinates, its intersection with cowl axis is determined. Based on the intersection, it is possible to determine whether the inlet is at on-design or off-design conditions. It has to be noted that

this procedure is implemented for cases with the following constraints: $\theta_{COWL} > 0, \alpha_{AoA} > 0, \theta_N > 0$ and $\theta_N > \theta_{COWL}$. It is worth to iterate here that all the following physical dimensions: β_{NB}, θ_N, α_{AoA} and θ_{COWL} (Figure 4-1 and Figure 4-5) are positive quantities (clockwise), any measurements made in the opposite sense (or anti-clockwise) are taken as negative quantities. Next, the procedure to analyze the internal compression at on-design and off-design conditions ($M_0 \leq M_{design}$) is addressed and the special off-design case ($M_0 > M_{design}$) is discussed at a later stage.

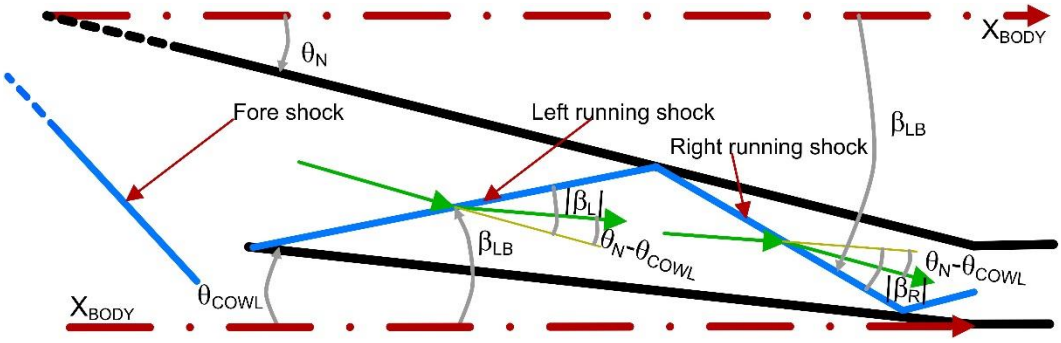

Figure 4-6: Schematic detailing of internal compression and its geometrical parameters.

To carryout internal compression analysis for ($M_0 \leq M_{Design}$) consider Figure 4-6 which involves multiple shock reflections inside a confined duct which is converging. The flow after passing through the fore-shock is oriented along the ramp at an angle θ_N with respect to X_{BODY}. The first shock inside the internal compression duct originates from the cowl lip for ($M_0 \leq M_{Design}$) which is a left running wave. The turn angle of the flow across a left running wave is given by $\Delta\theta = \theta_N - \theta_{COWL}$. The corresponding shock angle $|\beta_L|$ measured with respect to pre-shock flow direction is then mapped to global coordinates which makes an angle $\beta_{LB} = -(|\beta_L| - \theta_N)$ with respect to X_{BODY}. Using β_{LB} from the global frame, the shock is constructed and its intersection with the ramp side is recorded to obtain the reflection point. From this reflection point the next following right running shockwave with turn angle is $\Delta\theta = \theta_N - \theta_{COWL}$ and corresponding global shock angle $\beta_{RB} = (|\beta_R| +$

θ_{COWL}) is evaluated and constructed. This analysis of alternating left and right running shockwaves can be repeated until the nth shock crosses the inlet throat (station 1.5). To automate this procedure, the MATLAB tool was used and a brief description of the program is detailed in the flowchart depicted in Figure 4-10.

The analysis discussed so far yields a 2D flow field from the nose to throat. Beyond the throat, complex interaction between expansion waves and shockwaves takes place at off-design conditions. To carryout downstream analysis of the isolator a representative value for the flow entering it is computed by taking a control volume and mapping the 2D flow field to an equivalent 1D flow field. This method circumvents the analysis required to carry out shock and expansion wave interaction (Figure 4-7).

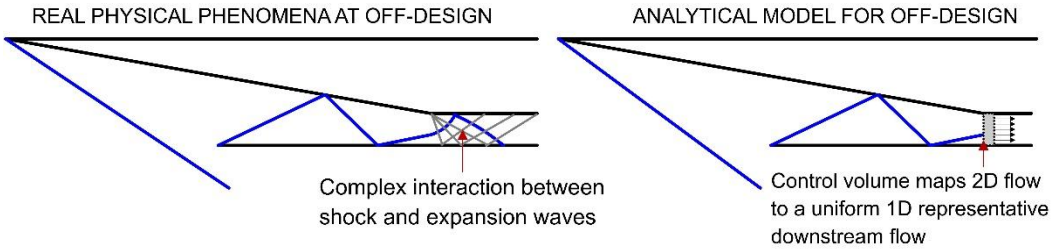

Figure 4-7: Schematic detailing method of mapping 2D complex flow field to equivalent 1D.

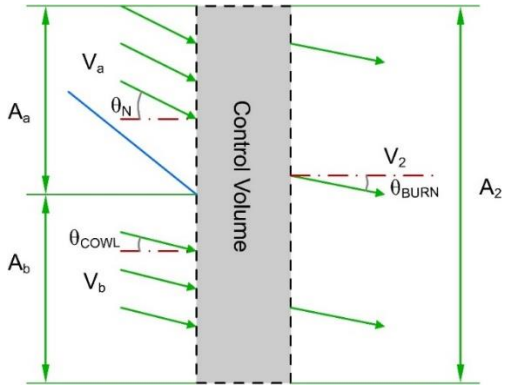

Figure 4-8: Control Volume to map 2D flow to 1D flow.

To carryout mapping of 2D flow to 1D flow consider a control volume shown in Figure 4-8. The last shock splits the inflow into with two areas $A_{\mathrm{a}}$and A_{b}. The subscript ‘a’ represents

the ramp side conditions, ‘b’ represents the cowl side conditions and ‘2’ represents the downstream outflow conditions. Note that the downstream flow is oriented along the burner axis X_{BURN}. The conservation equations (3.39-3.41, 3.6) with five unknowns are applied to the control volume in Figure 4-8 which is then reduced to one unknown (V_2) governed by non-linear equation (4.14). The equation (4.14) is solved in MATLAB platform using non-linear solver ‘fsolve’.

$$\left(\int_{T^0}^{\sigma_c(V_2)} c_p dT + \frac{V_2^2}{2}\right) C_{mass} - C_{energy} = 0 \tag{4.14}$$

The function $\sigma_c(V_2)$ in equation (4.14) is given by:

$$\sigma_c(V_2) = \frac{1}{R}\left(\frac{C_{momentum}}{C_{mass}} V_2 \cos(\theta_{BURN}) - V_2^2 \cos^2(\theta_{BURN})\right)$$

The constants C_{mass}, $C_{momentum}$ and C_{energy} depend only on the upstream conditions ‘a’ and ‘b’ and are given by:

$$C_{mass} = \rho_a V_a A_a \cos(\theta_N) + \rho_b V_b A_b \cos(\theta_{COWL})$$

$$C_{momentum} = (p_a + \rho_a V_a^2 \cos^2(\theta_N))A_a + (p_b + \rho_b V_b^2 \cos^2(\theta_{COWL}))A_b$$

$$C_{energy} = \left(\int_{T^0}^{T_a} c_p dT + \frac{V_a^2}{2}\right)\rho_a V_a A_a \cos(\theta_N) + \left(\int_{T^0}^{T_b} c_p dT + \frac{V_b^2}{2}\right)\rho_b V_b A_b \cos(\theta_{COWL})$$

Note that $A_2 = A_a + A_b$ and c_p is evaluated with procedure detailed in section 4.2.1. From equation (4.15) the velocity V_2 is computed following which other flow variables are computed as follows:

$$T_2 = \sigma_c(V_2)$$

$$\rho_2 = C_{mass}/A_2 V_2 \cos(\theta_{BURN})$$

$$p_2 = \rho_2 R T_2$$

The next step is to analyze the special off-design condition when $M_0 > M_{design}$, $\alpha \neq 0$ and $\theta \neq 0$. It can be seen from Figure 4-9 that complex interactions between expansion waves and shockwaves arise at the cowl lip. To accommodate this special case

in the analytical model, a control volume method at the cowl lip is used for mapping 2D flow to 1D flow using equation (4.14). Once the 1D flow at station '1' is evaluated, the internal compression is solved using quasi-one dimensional TPG flow.

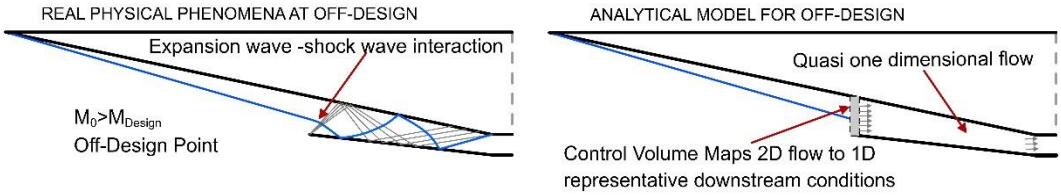

Figure 4-9: Schematic detailing method of mapping 2D complex flow field to equivalent 1D.

The physical process inside the internal compression for $M_0 > M_{design}$ is approximated to an isentropic quasi one-dimensional TPG flow along X_{BODY}. Although approximating the internal compression to quasi-one-dimensional flow reduces the fidelity, it gives a closure to the model by handling special off-design cases. The isentropic quasi-one dimensional flow is governed by differential equations (4.15, 4.16) which were derived from conservations equations (3.6, 3.39-3.41). The simultaneous ODE in equations (4.15, 4.16) were numerically integrating using 4th order Runge-Kutta method.

$$\frac{du}{dx} = \frac{u}{A}\left(\frac{\gamma RT}{u^2 - \gamma RT}\right)\frac{dA}{dx} \tag{4.15}$$

$$\frac{dT}{dx} = -\frac{u^2}{c_p A}\left(\frac{\gamma RT}{u^2 - \gamma RT}\right)\frac{dA}{dx} \tag{4.16}$$

In the equations (4.15, 4.16), the velocity u and temperature T are numerically integrated from which density, and pressure are found using mass conservation and state relationship respectively. The integration is performed till the throat after which control volume technique is used to orient the flow along burner axis. Note that c_p and γ are functions of temperature and are evaluated using procedure detailed in section 4.2.1.

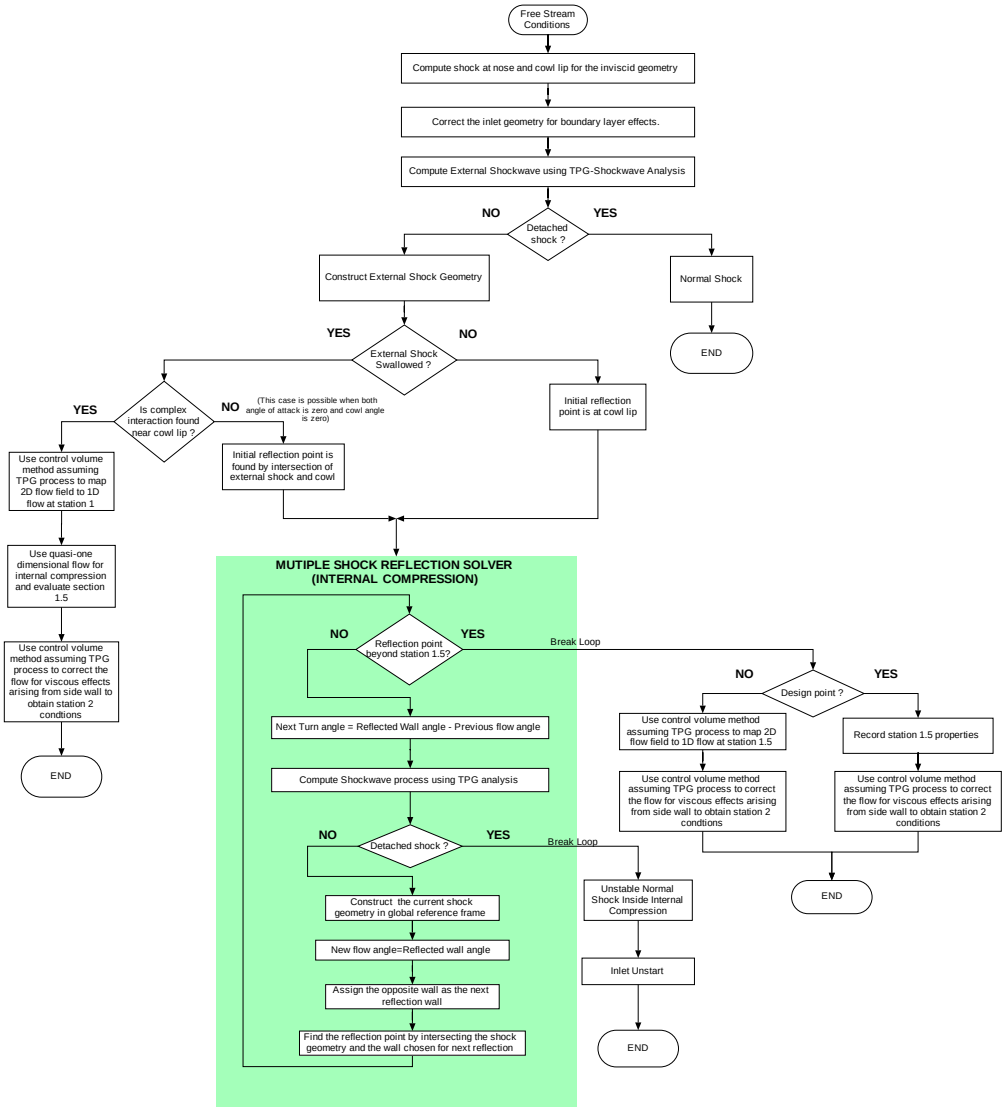

Figure 4-10: Flow chart of program implemented in MATLAB to perform inlet analysis.

To conclude the inlet shock reflection model, inlet-unstart must be addressed. We start with an assumption that a normal shock is formed when the oblique shockwave detaches, this is substantiated by Mattingly [29]. In a flow process when a normal shockwave is formed inside a converging section, it is unstable in nature and the inlet unstarts (Mattingly [29]). Therefore the model assumes the inlet to unstart if an oblique shockwave detaches during internal compression of the inlet (Figure 4-10).

4.2.3 Inlet Viscous Correction Model

In the previous section an inviscid model is presented to analyze the inlet. To model the viscous effects as a correction to the inviscid solution, theories governing flow over a flat plate (section 3.4) are used. Before discussing the viscous correction consider a brief discussion on flow inside confined ducts which will enable us to build the thought process to model the viscous effects. A constant area duct as shown in Figure 4-11 is subjected to a free stream supersonic flow. The flow process inside the duct involves boundary layer growth which produces blockage creating shockwaves inside it. This can be modelled in two ways. The first method is to construct an equivalent wedge with height that of displacement thickness δ^* obtained from flat plate boundary layer analysis (equation (3.32)). Following which the shock reflections in the inviscid region can be solved as described in section 4.2.2. The second alternative is to use a control volume with an equivalent frictional force evaluated using equation (3.27). The governing equations (3.39-3.41) inside the control volume can then be solved to obtain a representative downstream condition.

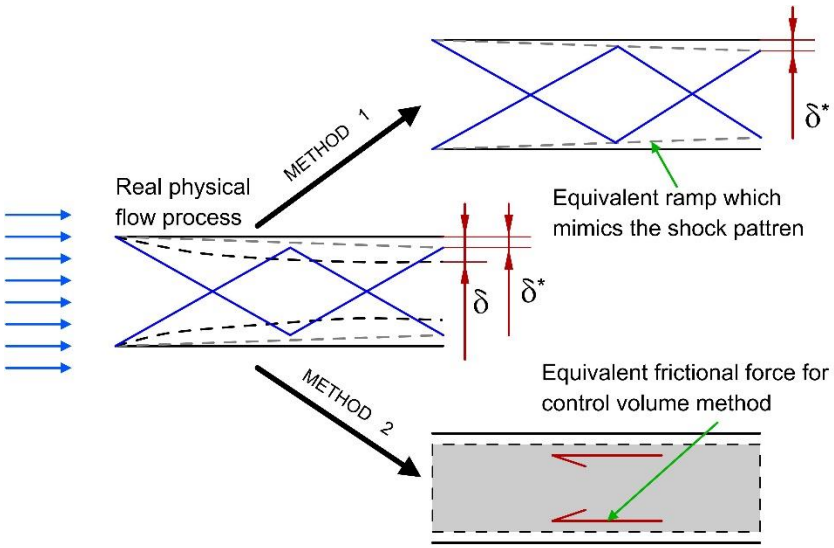

Figure 4-11: Models of evaluating flow inside constant area duct.

A combination of models presented in Figure 4-11 is used to model viscous correction for the inlet. Consider the schematic shown in Figure 4-12. At station 2, or throat of the inlet, the displacement thickness on the ramp side is δ_r^* and on the cowl side is δ_C^*. To compute δ_r^* and δ_C^*, first the inviscid fore shock and cowl lip shock are computed. The corresponding post shock conditions are then used to evaluate the displacement thickness using equation (3.32). Upon evaluating δ_r^* and δ_C^*, the viscous corrected geometry can be obtained as shown in Figure 4-12 and the corresponding shock reflections followed by its equivalent 1D downstream flow are obtained (section 4.2.2). The viscous corrected geometrical parameters are given in equations (4.17-4.19)

$$H_{TH}^* = H_{TH} - \frac{\delta_r^*}{\cos(\theta_N)} - \frac{\delta_C^*}{\cos(\theta_{COWL})} \tag{4.17}$$

$$\theta_N^* = \theta_N + \tan^{-1}\left(\frac{\delta_r^*}{L_N}\cos(\theta_N)\right) \tag{4.18}$$

$$\theta_{COWL}^* = \theta_{COWL} - \tan^{-1}\left(\frac{\delta_c^*}{L_{COWL}}\right) \tag{4.19}$$

To capture the side wall viscous effects, an average skin friction coefficient is computed between station 1 and 1.5 using equation (3.27) from which the viscous forces are computed. A control volume process with viscous forces is then used to obtain the corrected 1D downstream flow as detailed in Appendix B.

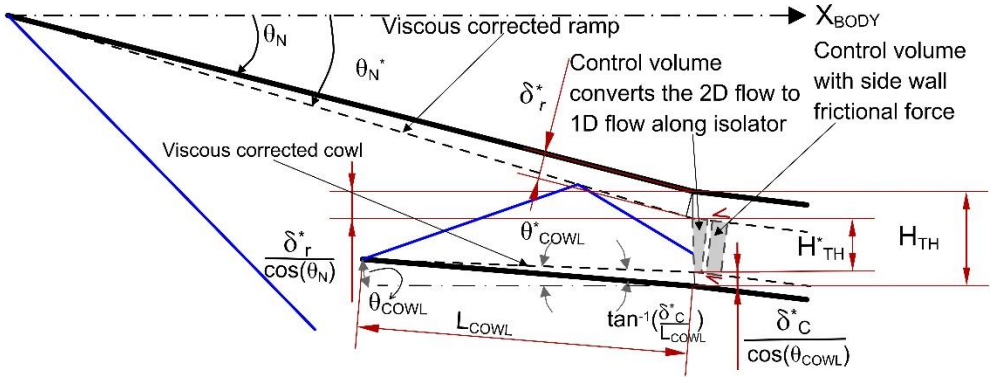

Figure 4-12: Schematic diagram depicting inlet viscous correction for model.

4.3 Isolator Model

The isolator is a duct which prevents the downstream combustion process from interacting with the upstream inlet compression process. Based on the burner conditions, the isolator mainly operates in three steady modes namely; shock-free mode, oblique shock-train mode and normal shock-train mode. In this section the analytical model for each mode of isolator operation is presented while the bifurcation model for these modes is discussed later. As the physical flow process inside the isolator is different for each operating mode, they are modelled uniquely assuming a thermally perfect gas process.

The DMSJ isolator considered in the current work is an insulated constant area rectangular duct oriented along the burner axis X_{BURN}. The schematics of isolator modes of operation are presented in Figure 4-13.

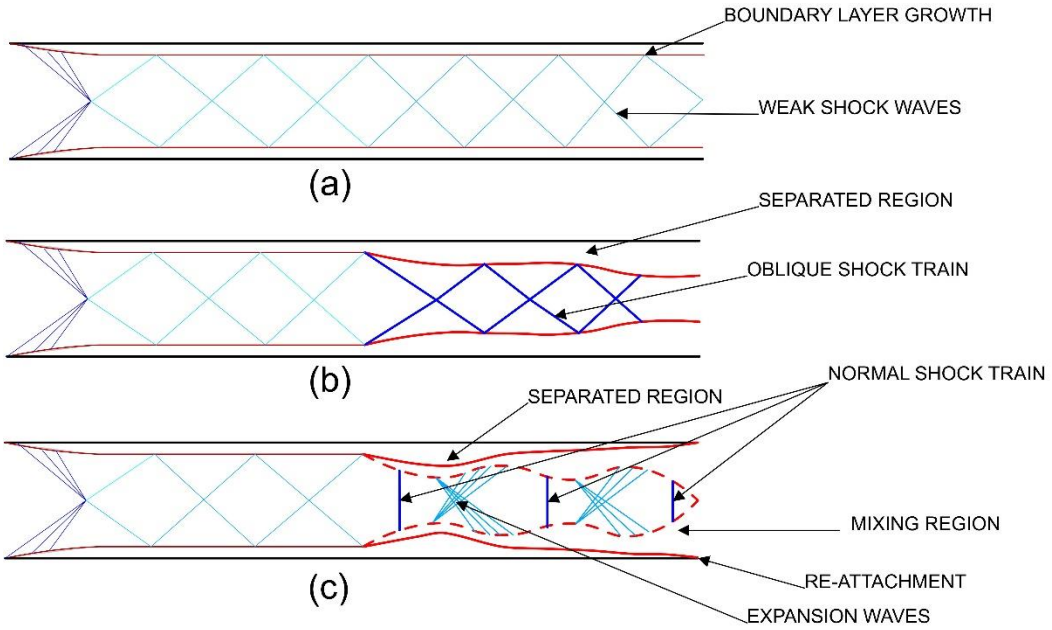

Figure 4-13: Schematic diagram depicting flow characteristics at different modes of isolator operation. (a) Shock free isolator mode. (b) Oblique shock train mode. (c) Normal shock train mode.

The shock free isolator mode (Figure 4-13(a)) is characterized with a thin boundary layer growth along the walls producing a system of weak oblique shocks inside the core flow. The pressure rise in the shock free isolator mode is of same order of magnitude predicted by a one dimensional Fanno flow [26].

The oblique shock train mode (Figure 4-13(b)) is established when the burner back pressure is high enough to cause boundary layer separation inside the isolator. This essentially is a mechanism in which the “excess pressure” leaks up-stream of the burner through the subsonic part of boundary layer. Therefore, the burner back pressure is imposed on the isolator exit. When the flow inside the isolator separates, it creates substantial blockage for the supersonic core flow by compressing it through a system of oblique shock waves.

The normal shock train mode (Figure 4-13(c)) inside the isolator is established when the burner operates in ramjet mode (or subsonic combustion) to provide appropriate burner entry conditions. The flow behind each normal shockwave is subjected to a CD-nozzle type flow facilitated by separated boundary layer in which the subsonic flow behind the normal shockwave is converted to supersonic flow. This supersonic flow is again compressed through a normal shockwave and so on until the burner imposed entry conditions are satisfied. Note that in Figure 4-13(c), the mixing region is characterized by subsonic flow which encloses the supersonic core-flow. The separated region usually re-attaches near the entrance of the burner as the pressure starts dropping when subsonic combustion is initiated [26].

4.3.1 Shock Free Isolator Model

The isolator operates in shock-free mode when the burner back pressure is not sufficient to cause any flow separation. Therefore the only physical process which occurs in the isolator is boundary layer growth along its walls. This causes weak compression

waves to slightly increase the pressure through the duct. The model proposed to analyze shock free mode uses a one-dimensional TPG flow process with friction. The analytical model corresponding to the shock free mode is depicted in Figure 4-14.

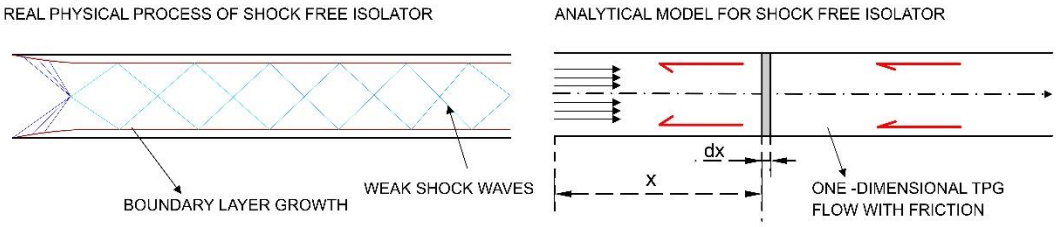

Figure 4-14: Schematic diagram of analytical model for shock free isolator.

The one dimensional flow with friction is governed by differential equations (4.15, 4.16) which were derived from conservations equations (3.6, 3.39-3.41). The simultaneous ODE in equations (4.15, 4.16) are numerically integrating using 4th order Runge-Kutta method [30].

$$\frac{du}{dx} = -\frac{1}{2}\frac{u}{\left(1-\frac{RT}{u^2}-\frac{R}{c_p}\right)}\left(\frac{4}{D_h}c_f\ \frac{T}{T^*}\right) \tag{4.20}$$

$$\frac{dT}{dx} = \frac{1}{2c_p}\frac{u^2}{\left(1-\frac{RT}{u^2}-\frac{R}{c_p}\right)}\left(\frac{4}{D_h}c_f\ \frac{T}{T^*}\right) \tag{4.21}$$

In equations (4.15, 4.16), the velocity u and temperature T are numerically integrated from which density and pressure are found using mass conservation and state relationship respectively. The variable D_h represents the hydraulic diameter of the duct and the skin friction coefficient c_f defined in equation 3.27 is a function of average distance from the fore edge of all the four isolator walls. Note that c_p is function of temperature and evaluated using procedure detailed in section 4.2.1. If the flow chokes before the exit of the isolator it is considered as unstart of the engine. The flow chart for shock free mode is detailed in Figure 4-18.

4.3.2 Oblique Shock Train Isolator Model

The isolator operates in oblique shock-train mode when the boundary layer possess insufficient momentum to flow against burner back-pressure. To model the oblique shock train, the separated region is modelled as two confined wedges as depicted in Figure 4-15. As shock reflections between the confined wedges are symmetric about the center axis, it can be solved using similar methods implemented in the inlet shock reflection model (refer section 4.2.2).

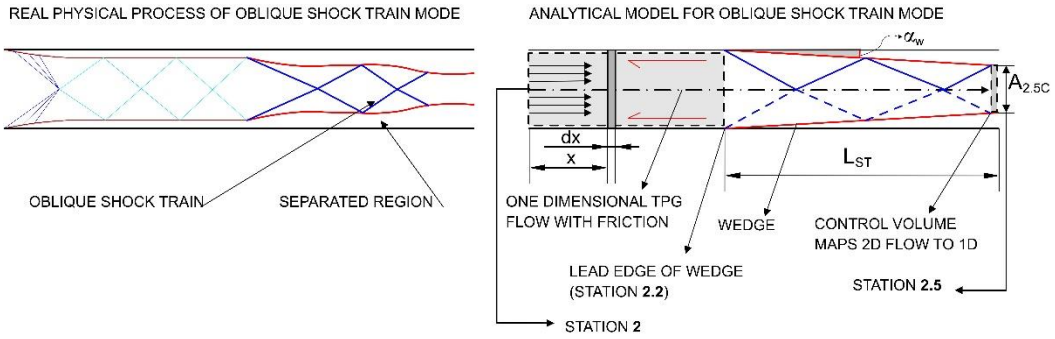

Figure 4-15: Schematic diagram of analytical model for oblique shock train mode.

To construct the wedge, (which is equivalent to the separated region) its length (L_{ST}) and inclination angle (α_w) should be determined. The wedge length (L_{ST}) represents the shock train length which is obtained from semi-empirical models. These semi-empirical relations are provided by Waltrup and Billig [25] for $M_2 < 2.5$ (equation 4.22) and Ortwerth [11, 18] for $M_2 > 2.5$ (equation 4.23).

$$L_{ST}|_{M_2<2.5} = \left(\frac{\theta_m^{\frac{1}{2}}}{Re_{\theta_m}^{\frac{1}{4}}}\right)\frac{\sqrt{D_h}}{M_2^2-1}\left[50\left(\frac{p_{2.5}}{p_2}\right)+170\left(\frac{p_{2.5}}{p_2}-1\right)^2\right] \qquad (4.22)$$

Where,θ_m depicts the entrance momentum thickness at station 2 and the corresponding Reynolds number is given by $Re_{\theta_m} = \rho_2 u_2 \theta_m/\mu$. Note that the pressure $p_{2.5}$ at the isolator exit is fixed by the burner.

$$L_{ST}|_{M_2>2.5} = \frac{D_h}{4K}\frac{g_2^2}{\gamma f_2}\left[\frac{\left(\frac{p_{2.5}}{p_2}-1\right)}{\left(f_2-\frac{p_{2.5}}{p_2}\right)(f_2-1)}+\frac{1}{f_2}\ln\left(\frac{\frac{p_{2.5}}{p_2}(f_2-1)}{f_2-\frac{p_{2.5}}{p_2}}\right)\right] + \frac{\gamma-1}{2\gamma}\ln\left(\frac{p_{2.5}}{p_2}\right) \quad (4.23)$$

where, $K = 44.5\bar{c}_f$, $g_2 = \dot{m}\sqrt{(\gamma-1)h_t}/p_2A_2$ and $f_2 = (p_2A_2 + \rho_2u_2A_2)/p_2A_2$. The ratio of specific heats (γ) is evaluated for temperature T_2. Note that $\bar{c_f}$ is the skin friction co-efficient near the entrance of the isolator.

Once the wedge length (L_{ST}) is set, the region upstream of the wedge (which is shock free) is analyzed using TPG one-dimensional flow with friction as detailed in section 4.3.1. This analysis yields conditions at station 2.2 which are then used as upstream conditions for the wedge (Figure 4-15). The wedge angle (α_w) is then incremented in small steps producing different patterns of shock reflections until a detached shock is formed. These patterns are then stored in MATLAB and a control volume at station 2.5 for each of these patterns is used to map the 2D flow to an equivalent 1D flow by conserving the fluxes using similar methods detailed Figure 4-8. From all the possible wedge inclinations, the corresponding isolator exit 1D flow pressure ($p_{2.5}$) which matches the imposed back pressure is selected. The wedge angle α_w for the corresponding case which matches the back pressure is the required wedge inclination to mimic the separated region.

The isolator model proposed in this section retains the flow characterization as close as possible to physical processes in order to capture accurate total pressure losses. It is important to note that the physical flow process may produce unsymmetrical shock systems due to distorted boundary layer entering the isolator. However the current model assume symmetrical shock systems which provides approximate insight into total pressure losses. The flow chart for oblique shock train mode is detailed in Figure 4-18.

4.3.2 Normal Shock Train Isolator Model

A series of normal shockwaves are formed in the isolator to match the burner entry Mach number in ramjet mode. The flow behind each normal shockwave is subjected to an expansion regime, where the subsonic flow behind the normal shockwave turns to supersonic flow. This process is facilitated by the separated boundary layer region which acts like a CD-nozzle. After expanding the flow to the supersonic regime, the flow is again compressed through another normal shockwave and it is followed by an expansion process. This process of normal shock compression and expansion to supersonic flow repeats until the burner imposed entry Mach number is satisfied.

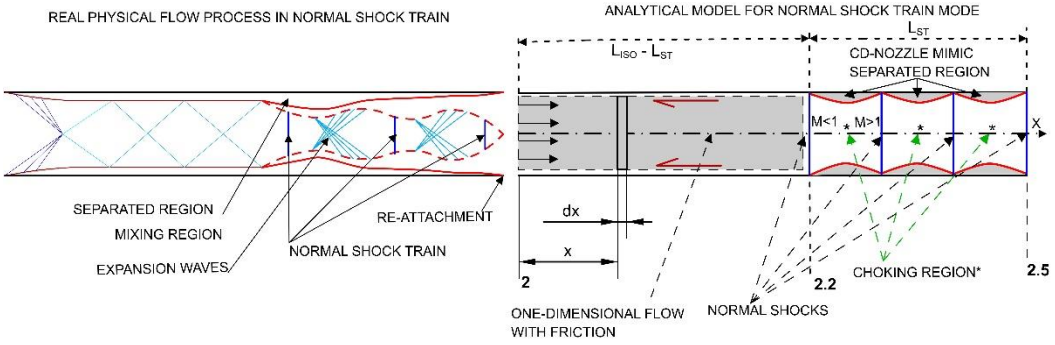

Figure 4-16: Schematic diagram of analytical model for normal shock train mode.

To model the normal shock-train mode, (Figure 4-15) repeating pairs of normal shock and CD-nozzle flow are used. The flow behind each normal shock is subsonic and the corresponding CD-nozzle converts the flow to supersonic flow. The number of shock-nozzle pairs (n) required to create the $(n+1)^{th}$ post shock Mach number as close as possible to the requested Mach number by the burner is calculated. Note that by choosing the post shock Mach number (and not intermediate Mach number inside the CD-nozzle), we can achieve reattachment criteria [25]. As the pairs of shock-nozzle causes the discrete results for Mach number, the closest Mach number to the burner requested condition is chosen.

The length of the shock train L_{ST} is computed using experimental correlation provided by Heiser and Pratt [25]. It is to be noted that the minimum Mach number (or maximum pressure rise) that an isolator can provide is through one single normal shockwave.

Before the TPG analysis of the normal shock train model is carried out, consider the analysis from CPG perspective. If a point inside a flow is picked, the corresponding isentropic CPG choking area is say A^*. The A^* across a normal shock changes and can be determined using equation (4.24) [26], where subscript 'u' and 'p' represents upstream and down-stream conditions of a normal shock.

$$A_u^* p_{t_u} = A_p^* p_{t_p} \tag{4.24}$$

The variation of total pressure across a normal shock is given by:

$$\frac{p_{t_p}}{p_{t_u}} = \exp\left(-\frac{\Delta s}{R}\right) < 1 \tag{4.25}$$

As the entropy always increases, it can be seen from equations 4.24 and 4.25 that A^* across a normal always increases. Consider isentropic relationship for quasi-one dimensional flow which relates Mach number and A/A^*[26] given by:

$$\left(\frac{A}{A^*}\right)^2 = \frac{1}{M^2}\left[\frac{2}{\gamma+1}\left(1+\frac{\gamma-1}{2}M^2\right)\right]^{\frac{\gamma+1}{\gamma-1}} \tag{5.26}$$

The CPG perspective of the normal shock train model is understood using Figure 4-17, where equation 4.26 is plotted. Across the shock A^* increases therefore, for the same flow area A, the ratio A/A^*reduces. Once the supersonic flow becomes subsonic across the shock, it is then converted to supersonic flow through an isentropic nozzle with same entrance and exit area A. When the shock-nozzle process is repeated, we can see that the post shock Mach number asymptotically reaches Mach 1 from Figure 4-17. Note that in Figure 4-17, the jumps across the shock and isentropic expansion are not computed values and are meant only for illustration purposes.

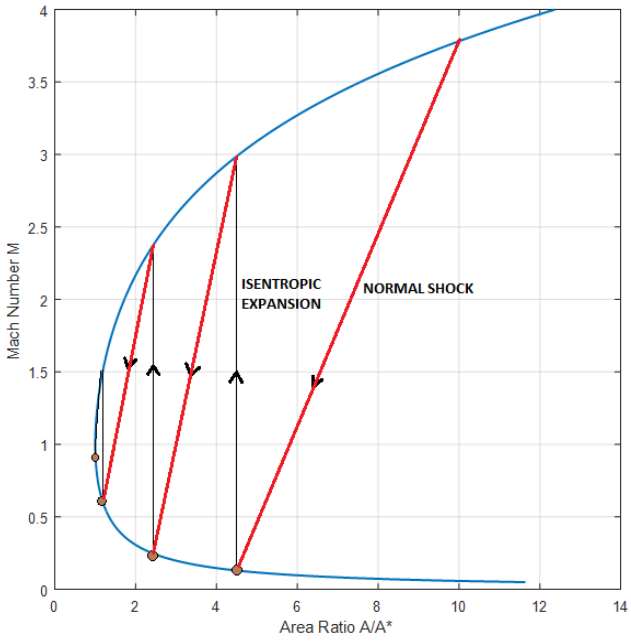

Figure 4-17: Schematic of CPG normal shock train model mapped on area-Mach number relationship.

Now that the CPG analysis of the normal shock train model is seen, let us consider the TPG analysis of the same. The normal shocks for TPG flow are analyzed using equations 4.9 to 4.13 presented in section 4.2.1. The quasi-one dimensional flow in the nozzle is analyzed by integrating equations 4.15 and 4.16 presented in section 4.2.2. Note that while integrating equation 4.15 and 4.16, the singularity near the choke point is avoided by using CPG equation (4.26) near the throat. This analysis is repeated inside a loop using MATLAB to generate different post shock Mach numbers until it asymptotically reaches Mach ~1. This data is stored in MATLAB and the corresponding closest post shock Mach number to the burner imposed Mach number is selected. Therefore the number of normal shocks required is calculated. The flow chart for the isolator model details the normal shock train mode in Figure 4-18.

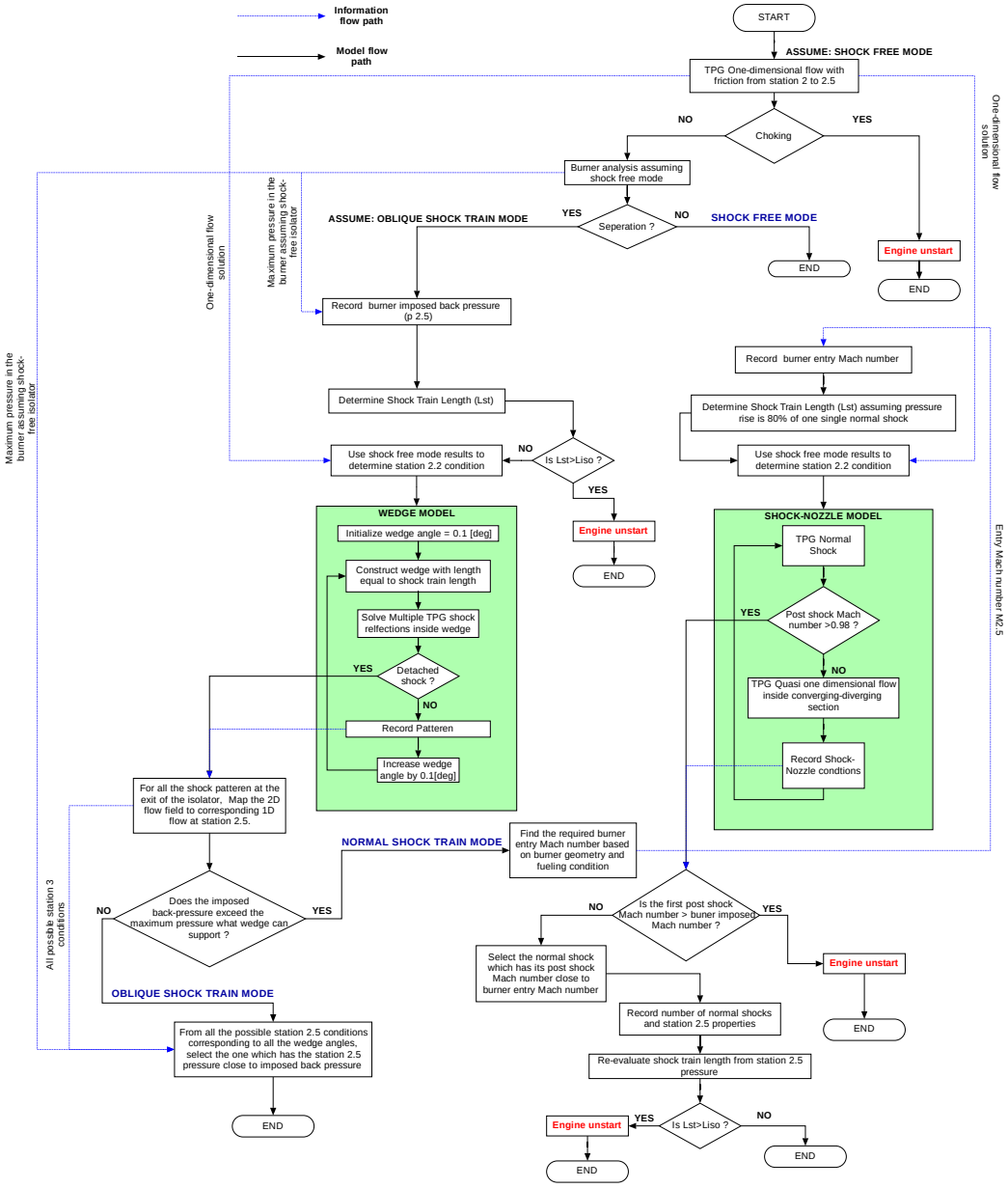

Figure 4-18: Flow chart of program implemented in MATLAB to perform isolator analysis.

The flow chart of the isolator model proposed in the current work is presented in Figure 4-18, where the engine unstart scenarios are depicted. Note that the mode determination technique through iterative burner analysis is discussed in isolator burner interaction model presented in section 4.5.3.

4.4 Fuel Injector Model

The SCRamjet injector plays a vital role in shaping the performance of the engine. The injector is expected to provide the right amount of fuel flow to sustain combustion with minimum total pressure losses. In this section a generalized model to analyze typical SCRamjet injectors is introduced.

The model proposed for analyzing the SCRamjet injector broadly divides it into two types namely, intrusive and non-intrusive injection. Intrusive injectors, for example, ramp or strut injectors, consist of solid object inside the flow field to add fuel; whereas, non-intrusive, for example wall injector or step injector, doesn't contain any solid structure inside the flow field during injection. Consider a generalized control volume analysis for both intrusive and non-intrusive type injection as shown in Figure 4-19.

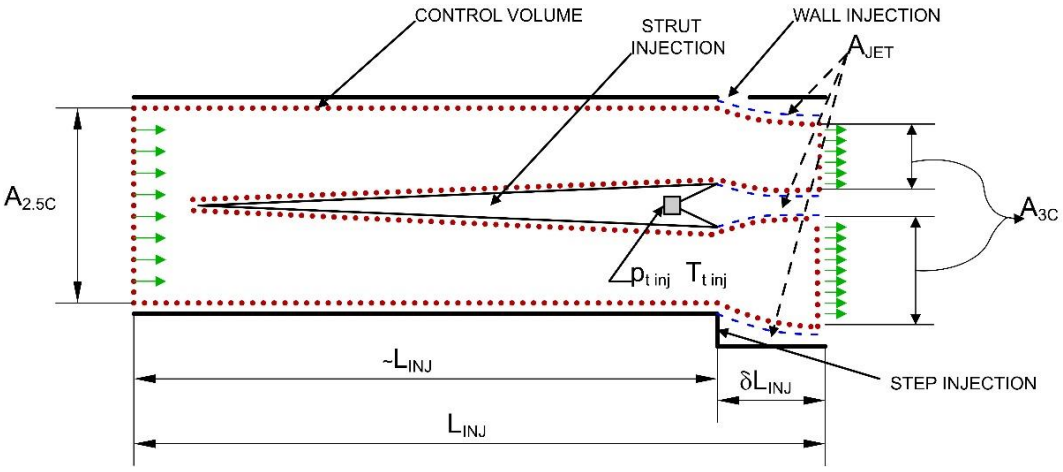

Figure 4-19: Control volume analysis of a generalized SCRamjet injector.

Depending on whether the flow is separated or not, the upstream of the injector system (station 2.5) has a core area of $A_{2.5C}$ or $A_{2.5}$ respectively. The separated area at the injector entrance is given by:

$$A_{sep} = A_{2.5} - A_{2.5C} \tag{4.27}$$

In Figure 4-19, consider fuel injection from all the possible injector systems with final wall area A_3. The core flow at station 3 or injector exit is assumed to have an area A_{3C} which excludes the fuel jet area and the separated area. Therefore the core flow area at station 3 is given by:

$$A_{3C} = A_3 - A_{sep} - A_{jet} \tag{4.28}$$

In the control volume analysis of the injector, a "near downstream flow region" is considered with flow length of δL_{inj} such that $(\delta L_{inj}/L_{inj}) \ll 1$. This flow regime is assumed to facilitate the pressure balance across the slip line dividing the air stream and fuel jet without any mixing between them. The control volume analysis for the generalized injector is introduced with mass conservation equation (4.29) which is derived from equation (3.39).

$$\rho_{2.5C} u_{2.5C} A_{2.5C} = \rho_{3C} u_{3C} A_{3C} = \dot{m} \tag{4.29}$$

The momentum conservation can be derived using equation (3.40) as follows:

$$-\dot{m}(u_{2.5C} - u_{3C}) = p_{2.5C} A_{2.5C} - p_{3C} A_{3C} - \int\int_{wall+jet} p dA_x \tag{4.30}$$

In the above equation the pressure integral part evaluated on the wall and fuel jet can be approximated as:

$$\int\int_{wall+jet} p dA_x \approx F_{DRAG} + \frac{p_{3C} + p_{2.5C}}{2}(A_{3c} - A_{2.5C}) \tag{4.31}$$

In equation 4.31, F_{DRAG} represents the injector pressure drag and can be modelled using the drag coefficient (C_D) of the intrusive part with reference area S_{ref}. Therefore the pressure integral term in equation 4.30 mainly represents the drag due to intrusive solid object (strut, ramp etc.) and effect of net core area change. From equations 4.27, 4.28, 4.30 and 4.31, the momentum equation reduces to the following:

$$\begin{aligned}(p_{3C} A_{3C} + \dot{m} u_{3C}) - (p_{2.5C} A_{2.5C} + \dot{m} u_{2.5C}) \\ = -F_{DRAG} - \frac{p_{3C} + p_{2.5C}}{2}(A_3 - A_{2.5} - A_{jet})\end{aligned} \tag{4.32}$$

The energy conservation for the control volume using equation (3.41) is detailed in equation (4.33).

$$h_{2.5C} + \frac{1}{2}u_{2.5C}^2 = h_{3C} + \frac{1}{2}u_{3C}^2 = h_t \tag{4.33}$$

Recall equation 4.28, the only unknown in the equation is the jet area A_{jet}. To evaluate A_{jet}, it is required to match the pressure across the slip stream (p_{3C}). Therefore, consider the chamber pressure and temperature of the fuel as $p_{t\ inj}$ and $T_{t\ inj}$ respectively as shown in Figure 4-20. Note that in Figure 4-20 only the strut A_{jet} is depicted whereas the A_{jet} used in the generalized control volume includes the jet area from all the other injectors as well.

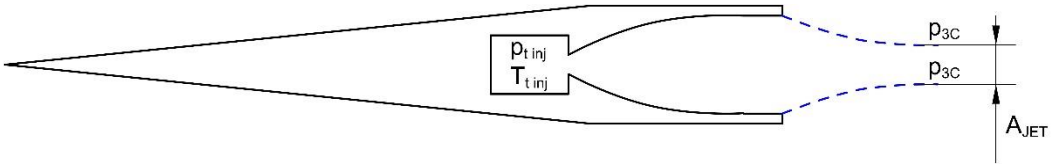

Figure 4-20: Schematic of strut injector and the corresponding downstream jet area.

Assuming the flow process of fuel is isentropic, the total pressure of the fuel can be used for expressing its Mach number as follows:

$$M_{jet} = \sqrt{\frac{2\left(\left(\frac{p_{t\ inj}}{p_{3C}}\right)^{\frac{\gamma_f - 1}{\gamma_f}} - 1\right)}{\gamma_f - 1}} \tag{4.34}$$

Where, γ_f represents fuel ratio of specific heats chosen at a representative temperature. Using mass flow parameter (MFP) [29], the jet area can be computed as follows:

$$A_{jet} = \frac{\dot{m}_f\sqrt{T_{t\ inj}}}{p_{t\ inj}MFP(\gamma_f, M_{jet})} = A_{jet}(p_{t\ inj}, T_{t\ inj}, p_{3C}) \tag{4.35}$$

From equation 4.35, it can be seen that the jet area (A_{jet}) is a function of injector chamber properties ($p_{t\ inj}, T_{t\ inj}$) and the pressure at station 3 or p_{3C}. Therefore, the generalized

injector control volume is governed by equations 4.28, 4.29, 4.32, 4.33 and 4.35. These five equations can be simplified into two non-linear equations with unknowns p_{3C} and T_{3C} in equations 4.36 and 4.37.

$$\dot{m}\sqrt{2\left(h_t - \int_{T_{ref}}^{T_{3C}} C_p dT\right)} - I_{2.5} + \frac{1}{2}\rho_{2.5C} u_{2.5C}^2 C_D S_{ref} + \frac{3p_{3C} + p_{2.5C}}{2}\left(A_3 - A_{2.5} - \frac{\dot{m}_f\sqrt{T_{t\,inj}}}{p_{t\,inj} MFP(\gamma_f, M_{jet})}\right) = 0 \tag{4.36}$$

$$\frac{p_{3C}}{RT_{3C}}\left(\sqrt{2\left(h_t - \int_{T_{ref}}^{T_{3C}} C_p dT\right)}\right)\left(A_3 - A_{2.5} - \frac{\dot{m}_f\sqrt{T_{t\,inj}}}{p_{t\,inj} MFP(\gamma_f, M_{jet})}\right) - \dot{m} = 0 \tag{4.37}$$

Where, $I_{2.5} = (p_{2.5C}A_{2.5C} + \dot{m}u_{2.5C})$ and M_{jet} is a function of p_{3C} given in equation 4.34. The equation 4.36, 4.37 are solved simultaneously using MATLAB inbuilt solver 'fsolve' [27]. Once the pressure and temperature are obtained all the remaining flow parameters can be evaluated using equations (4.33, 4.29, and 3.6). Note that the effect of vectored injection $\overrightarrow{u_f} = u_{fx}\hat{\imath} + u_{fy}\hat{\jmath}$ or flame holders (example, Cavity holder) are captured in the mixing process in burner analysis and not explicitly in the injector analysis.

4.5 Burner Model

The combustion process in a dual mode SCRamjet can be either supersonic or subsonic. The supersonic mode is established at a higher entrance Mach number for a given fueling condition while, the subsonic mode is established at relatively lower entrance Mach number with specific fueling condition to establish the thermal throat [25]. The burner model proposed in this section to analyze SCRamjet dual mode combustion is of one-dimensional fidelity. The theory of generalized quasi-one-dimensional flow with the fuel-air

mixing is used to model the burner and internal nozzle (Figure 4-1). Consider the generalized burner-internal nozzle geometry in Figure 4-21.

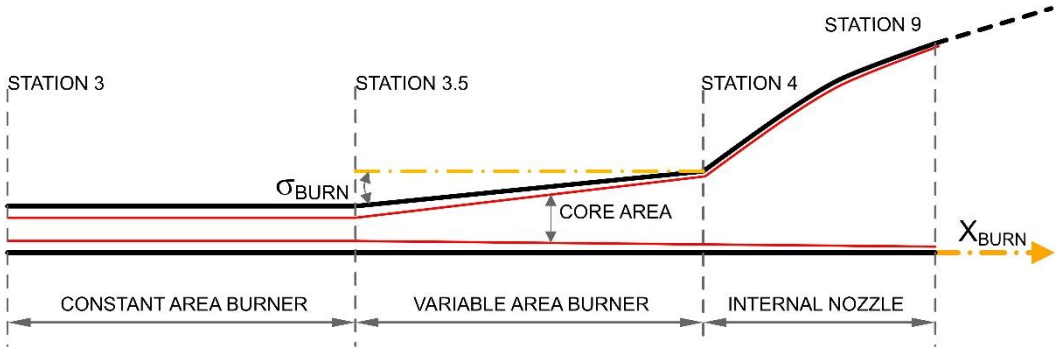

Figure 4-21: Schematic of generalized burner internal nozzle and their station nomenclature.

From Figure 4-1 and 4-21, the constant area burner is followed by variable area burner with constant diverging angle σ_{BURN} at station 3.5. The internal nozzle is also considered as a part of the burner for the analysis until the nozzle cowl lip at station 9. The core area for which the analysis is carried out excludes the separated region and unmixed fuel jet. Consider an elemental control volume inside the burner which consist of unmixed air and mixed fuel-air as shown in Figure 4-22.

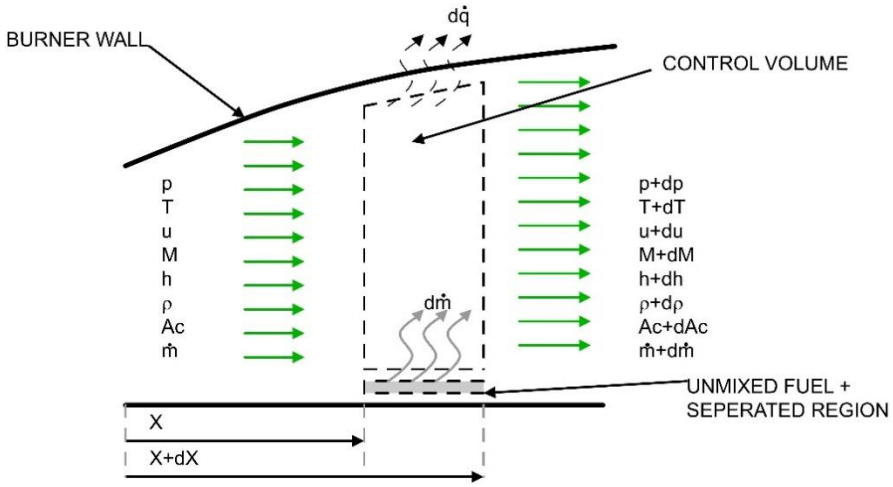

Figure 4-22: Schematic of elemental control volume for burner analysis.

The integral conservation equations (3.39 to 3.41) are applied to the elemental control volume shown in Figure 4-22 and the corresponding differential forms are obtained. The differential equations are then integrated using 4th order Runge-Kutta method [30] from station 3 to 9. The burner model is presented in three parts namely; supersonic combustion, subsonic combustion and isolator-burner interaction.

4.5.1 Supersonic Combustion

When the isolator operates in shock free or oblique shock train mode, the burner operates in supersonic combustion mode. The method of determining the operating mode is discussed in the isolator-burner interaction model presented in section 4.5.3. At first mass conservation and supersonic mixing is discussed.

4.5.1.1 Mass Conservation and Supersonic Mixing

The mass flow rate of the unmixed air and mixed fuel-air is given by:

$$\dot{m} = \rho u A \tag{4.38}$$

where, A (or A_c) represents the core area defined as:

$$A = A_{wall} - A_{sep} - A_{jet} \tag{4.39}$$

The mass flow rate defined in equation (4.38) can be split into the following components:

$$\dot{m} = \dot{m}_{air} + \dot{m}_f \eta_m \tag{4.40}$$

where, η_m represents mixing efficiency. The mixing efficiency is defined as the ratio of mass flow rate of mixed fuel to total fuel added.

$$\eta_m = \frac{\dot{m_{fm}}}{\dot{m}_f}$$

The mass conservation given in equation (3.39) when applied to the control volume in Figure 4-22 yields the following differential equation.

$$\frac{1}{\rho}\frac{d\rho}{dx} + \frac{1}{u}\frac{du}{dx} + \frac{1}{A}\frac{dA}{dx} = \frac{1}{\dot{m}}\frac{d\dot{m}}{dx} \tag{4.41}$$

The rate of change of mass flow rate ($d\dot{m}/dx$) in equation 4.41 is solely due to mixing process. This means that change in mass flow rate ($d\dot{m}$) is equal to change in mass flow rate of mixed fuel inside the control volume ($d\dot{m}_{fm}$). Therefore, from equation 4.40, the rate of change of mass flow rate can be related to mixing efficiency as follows:

$$\frac{1}{\dot{m}}\frac{d\dot{m}}{dx} = \frac{1}{\dot{m}}\frac{d\dot{m_{fm}}}{dx} = \frac{\dot{m}_f}{\dot{m}}\frac{d\eta_m}{dx} = \frac{F_{AR}}{1 + F_{AR}\eta_m}\frac{d\eta_m}{dx} \tag{4.42}$$

Where, F_{AR} represents fuel to air ratio ($\dot{m}_f/\dot{m}_a$) injected into the burner. Now, a brief discussion on supersonic mixing is made in order to introduce $\eta_m(x)$.

The supersonic mixing depends on a type of injector system which doesn't have a universal closed form solution so far. An engineering approach to model supersonic mixing involves semi-empirical relations based on experimental data fits. A brief summary of mixing models available in the literature [25, 5, 18] is presented here:

- Parallel injection model (ex. strut):

$$\eta_m = \frac{x}{L_{mix}}$$

$$L_{mix} \simeq 0.179\, H\, C_m\, e^{1.72\phi}$$

  where, H represents the scale of segregation and the values of C_m typically varies from 25 to 60. An average value $C_m = 46$ is considered [25].

- Perpendicular hydrogen injection model (Example: Normal injector):

$$\eta_m = 1.01 + 0.176 \ln\left(\frac{x}{x_\phi}\right)$$

$$x_\phi = 0.179 L_{mix} \exp(1.72\phi)$$

$$L_{mix} \approx 60G$$

  Where, G represents the spacing of normal injectors. Note that this mixing model is only valid for hydrogen based fuel injection [18].

- Axial vortex mixing model (Example: Ramp, Hypermixer):

$$\eta_m = \frac{1 - e^{-\frac{Ax}{L_m}}}{1 - e^{-A}}$$

$$L_{mix} \simeq 0.179\, H\, C_m\, e^{1.72\phi}$$

where, H represents the scale of segregation. The values of C_m typically varies from 25 to 60. The variable A is a fit-parameter which varies from $1.77 < A < 3.4$. The higher values of A are usually used for swept ramps and lower for upswept ramps [25].

- Strut mixing model for hydrogen

$$\eta_m = a\left(1 - e^{-\left(\frac{kx}{L_{mix}}\right)^d}\right)$$

$$L_{mix} = \frac{D_f K^*}{f(M_c)}\left[\frac{\rho_f u_f}{\rho_a u_a}\right]^{1/2}$$

The constants are given by $a = 1.06492$, $k = 3.69639$ and $d = 0.80586$. The term $f(M_c)$ is compressible correction factor given by $f(M_c) = 0.25 + 0.75e^{-3M_c^2}$. The fuel jet diameter or thickness is given by D_f. The convective Mach number M_c is given by:

$$M_c = \frac{u_f - u_a}{a_f + a_a}$$

where u_f and u_a are the fuel injection velocity and the air velocity respectively. The acoustic velocity of air and fuel are given by a_a and a_f respectively. For slot type injection, $K^* = 390$ and varies with different injection configurations. Note that this mixing model is only valid for hydrogen fuel injection [5].

- Generalized parametric fit mixing models:
    - Exponential fit model:

$$\eta_m = 1 - \exp(-ax)$$

where the variable a is the fit parameter.

- Algebraic fit model:

$$\eta_m = \eta_b \left(\frac{\nu \frac{x}{L_c}}{1 + (\nu - 1)\frac{x}{L_c}} \right)$$

The term η_b is the maximum mixing efficiency and the term L_c is the characteristic length which is usually the mixing length or length of the burner. The variable ν is the fit parameter.

- Linear fit model:

$$\eta_m = a \frac{x}{L_{mix}}$$

where the variable a is the fit parameter and L_{mix} is the mixing length.

The supersonic mixing models described are coded as a subroutine in MATLAB platform [27] and are used while performing the burner computation. To conclude the mass conservation discussion, the core area derivative in equation (4.41) is given as:

$$\frac{dA}{dx} = \frac{dA_{wall}}{dx} - \frac{dA_{sep}}{dx} - \frac{dA_{jet}}{dx} \tag{4.43}$$

In the equation 4.43, the wall area variation is known from geometry and the jet area variation is assumed as $A_{jet} = \left(A_{jet}\right)_3 (1 - \eta_m)$ and the separation area and its variation is discussed in section 4.5.3.

5.5.1.2 Momentum Conservation

The momentum conservation in equation (4.44) for the control volume shown in Figure 4-22 is derived from equation (3.40). The rate of change in momentum is caused due to the effect of fuel addition with x-component velocity u_{fx}, effect of skin friction from

wetted surface with perimeter C_w and body force $\rho f_{bx} d\forall$. For most of the cases, the body force is zero except when an electro-magnetic force arise in MHD-type flows [31] or non-inertial forces due to accelerated flight conditions. Note that the momentum equation is written in the frame attached to burner walls.

$$\frac{dp}{dx} = -\frac{\dot{m}}{A}\frac{du}{dx} - \frac{\left(u - u_{fx}\right)}{A}\frac{d\dot{m}}{dx} - \frac{1}{2}\rho u^2 c_f \left(\frac{C_w}{A}\right) + \rho f_{bx} \tag{4.44}$$

4.5.1.3 Energy Conservation

The conservation of energy in equation (4.45) for the control volume shown in Figure 4-22 is derived from equation (3.41). The rate of change of energy inside the control volume depends on the energy added by the mixed fuel entering the control volume with total internal energy $e_{tf} = h_{fsens} + \Delta_f^0 h + (u_f^2/2) - (p_3/\rho_f)$, heat flux from wall $\dot{q}_{nf}$, volumetric heat addition $\dot{q_v}$ and work done by body force. Note that work done by frictional force is neglected.

$$\frac{dh}{dx} = -u\frac{du}{dx} - \left(h + \frac{u^2}{2} - e_{tf}\right)\frac{1}{\dot{m}}\frac{d\dot{m}}{dx} + \frac{\dot{q}_{nf} C_w}{\dot{m}} + f_{bx} + \frac{\dot{q_v}}{u} \tag{4.45}$$

4.5.1.4 State Relationship

The state relation in equation (4.46) is expressed in its derivative form. As the formulation considers flow in chemical equilibrium, the variation of mixture molecular weight ($\boldsymbol{\mathcal{M}}$) is also considered.

$$\frac{1}{p}\frac{dp}{dx} = \frac{1}{\rho}\frac{d\rho}{dx} + \frac{1}{T}\frac{dT}{dx} - \frac{1}{\boldsymbol{\mathcal{M}}}\frac{d\boldsymbol{\mathcal{M}}}{dx} \tag{4.45}$$

4.5.1.4 Burner Analysis

The aim of this sub-section is to derive burner equations which are compatible with 4th order Runge-Kutta integration [30] and the equilibrium solver. The chemical equilibrium model for hydrogen-air discussed in section 3.3.1 makes use of pressure, temperature and equivalence ratio as its input. Therefore, the burner ODE governing pressure and temperature variation compatible with 4th order Runge-Kutta integration scheme is derived. Consider compact form of momentum and energy conservation equations here.

Momentum conservation:

$$\frac{dp}{dx} = -\frac{\dot{m}}{A}\frac{du}{dx} + I_m \tag{4.46}$$

Energy conservation:

$$\frac{dh}{dx} = -u\frac{du}{dx} + I_e \tag{4.47}$$

Where,

$$I_m = -\frac{(u - u_{fx})}{A}\frac{d\dot{m}}{dx} - \frac{1}{2}\rho u^2\left(\frac{4c_f}{D_{Hb}}\right) + \rho f_{bx} \tag{4.48}$$

$$I_e = -\left(h + \frac{u^2}{2} - e_{tf}\right)\frac{1}{\dot{m}}\frac{d\dot{m}}{dx} + \frac{\dot{q}_{nf}C_w}{\dot{m}} + f_{bx} + \frac{\dot{q}_v}{u} \tag{4.49}$$

Note that D_{Hb} is the hydraulic diameter given by $4A/C_w$. Now to express the temperature derivative of enthalpy $h(\phi, T, p)$.

$$\frac{dh}{dx} = \left(\frac{\partial h}{\partial p}\right)_{T,\phi}\frac{dp}{dx} + \left(\frac{\partial h}{\partial T}\right)_{p,\phi}\frac{dT}{dx} + \left(\frac{\partial h}{\partial \phi}\right)_{p,T}\frac{d\phi}{dx} \tag{4.50}$$

Using equation 4.50, 4.46 and 4.47 we can have the following temperature derivative

$$\frac{dT}{dx} = \frac{1}{c_p}\left(\left(\left(\frac{\partial h}{\partial p}\right)_{T,\phi}\frac{\dot{m}}{A} - u\right)\frac{du}{dx} - \left(\frac{\partial h}{\partial p}\right)_{T,\phi} I_m - \left(\frac{\partial h}{\partial \phi}\right)_{p,T}\frac{d\phi}{dx} + I_e\right) \tag{4.51}$$

In the equation 5.51 the heat capacity at constant pressure (c_p) is defined as $\left(\frac{\partial h}{\partial T}\right)_{p,\phi}$.

Before deriving the pressure and temperature derivatives as a function of independent derivatives, the molecular mass derivative $d\boldsymbol{\mathcal{M}}/dx$ is expressed in terms of pressure and temperature derivatives. Consider the definition of mixture molecular mass $\mathcal{M} = 1/\sum(Y_k/\mathcal{M}_k)$. Taking the derivative of this expression give us:

$$\frac{d\boldsymbol{\mathcal{M}}}{dx} = -\boldsymbol{\mathcal{M}}^2 \sum \frac{1}{\mathcal{M}_k}\frac{dY_k}{dx} \tag{4.52}$$

where the mass fraction ($Y_k(\phi, T, p)$) derivative is given by:

$$\frac{dY_k}{dx} = \left(\frac{\partial Y_k}{\partial p}\right)_{T,\phi}\frac{dp}{dx} + \left(\frac{\partial Y_k}{\partial T}\right)_{p,\phi}\frac{dT}{dx} + \left(\frac{\partial Y_k}{\partial \phi}\right)_{p,T}\frac{d\phi}{dx} \tag{4.53}$$

Now using equations 4.46, 4.51 we can derive (Appendix C) the following equation:

$$\frac{d\boldsymbol{\mathcal{M}}}{dx} = \left(-\boldsymbol{\mathcal{M}}^2 \sum \frac{\sigma_{1k}}{\mathcal{M}_k}\right)\frac{du}{dx} + \left(-\boldsymbol{\mathcal{M}}^2 \sum \frac{\sigma_{2k}}{\mathcal{M}_k}\right)\frac{d\phi}{dx} + \left(-\boldsymbol{\mathcal{M}}^2 \sum \frac{\sigma_{3k}}{\mathcal{M}_k}\right) \tag{4.54}$$

where,

$$\sigma_{1k} = \left(\left(\frac{\partial Y_k}{\partial T}\right)_{p,\phi}\frac{1}{c_p}\left(\left(\frac{\partial h}{\partial p}\right)_{T,\phi}\frac{\dot{m}}{A} - u\right) - \left(\frac{\partial Y_k}{\partial p}\right)_{T,\phi}\frac{\dot{m}}{A}\right) \tag{4.55}$$

$$\sigma_{2k} = \left(\left(\frac{\partial Y_k}{\partial \phi}\right)_{p,T} - \left(\frac{\partial Y_k}{\partial T}\right)_{p,\phi}\frac{1}{c_p}\left(\frac{\partial h}{\partial \phi}\right)_{p,T}\right) \tag{4.56}$$

$$\sigma_{3k} = \left(\frac{\partial Y_k}{\partial p}\right)_{T,\phi} I_m + \left(\frac{\partial Y_k}{\partial T}\right)_{p,\phi}\frac{1}{c_p}\, I_e - \left(\frac{\partial Y_k}{\partial T}\right)_{p,\phi}\frac{1}{c_p}\left(\frac{\partial h}{\partial p}\right)_{T,\phi} I_m \tag{4.57}$$

The equivalence ratio is defined as fuel to air ratio (by mass or mole) to fuel to air ratio (by mass or mole) at stoichiometric conditions. Therefore, ϕ and its derivative are given by:

$$\phi = \frac{\left(\frac{F}{A}\right)_{mixed}}{\left(\frac{F}{A}\right)_{stoic}} = \frac{F_{AR}}{F_{AR_{st}}}\eta_m \tag{4.58}$$

$$\frac{d\phi}{dx} = \frac{F_{AR}}{F_{AR_{st}}}\frac{d\eta_m}{dx} \tag{4.59}$$

Using equation (4.59, 4.54, and 4.51) in 4.41, 4.45, 4.46 and 4.47 we obtain the ODE governing u,p and T as a function of independent derivatives (Appendix C) as follows:

$$\frac{du}{dx} = \frac{1}{\alpha}\left(-\frac{1}{A}\frac{dA}{dx} + \beta\frac{F_{AR}}{F_{AR_{st}}}\frac{d\eta_m}{dx} + \omega\right) \tag{4.60}$$

$$\frac{dp}{dx} = -\frac{\dot{m}}{A}\left(\frac{1}{\alpha}\left(-\frac{1}{A}\frac{dA}{dx} + \beta\frac{F_{AR}}{F_{AR_{st}}}\frac{d\eta_m}{dx} + \omega\right)\right) + I_m \tag{4.61}$$

$$\frac{dT}{dx} = \frac{1}{c_p}\left(\left(\left(\frac{\partial h}{\partial p}\right)_{T,\phi}\frac{\dot{m}}{A} - u\right)\frac{du}{dx} - \left(\frac{\partial h}{\partial p}\right)_{T,\phi} I_m - \left(\frac{\partial h}{\partial \phi}\right)_{p,T}\frac{F_{AR}}{F_{AR_{st}}}\frac{d\eta_m}{dx} + I_e\right) \tag{4.62}$$

where,

$$\alpha = \left(\frac{u}{c_pT} + \frac{1}{u} - \frac{1}{c_pT}\left(\frac{\partial h}{\partial p}\right)_{T,\phi}\frac{\dot{m}}{A} - \frac{\dot{m}}{pA} - \left(\boldsymbol{\mathcal{M}}\sum\frac{\sigma_{1k}}{\mathcal{M}_k}\right)\right)$$

$$\beta = \left(-\frac{1}{c_pT}\left(\frac{\partial h}{\partial \phi}\right)_{p,T} + \left(\boldsymbol{\mathcal{M}}\sum\frac{\sigma_{2k}}{\mathcal{M}_k}\right)\right)$$

$$\omega = \left(-\frac{I_m}{p} - \frac{\left(\frac{\partial h}{\partial p}\right)_{T,\phi} I_m}{c_pT} + \frac{I_e}{c_pT} + \left(\boldsymbol{\mathcal{M}}\sum\frac{\sigma_{3k}}{\mathcal{M}_k}\right) + \frac{\dot{m}_f}{\dot{m}}\frac{d\eta_m}{dx}\right)$$

Any two of the ODE's proposed in equations (4.60, 4.61 and 4.62) are integrated simultaneously using 4th order Runge-Kutta. The pressure and temperature ODE (4.61 and 4.62) are chosen for the integration as it is compatible with the chemical equilibrium solver (similar methods were used by [32]). For a typical SCRamjet burner, the following conditions are used:

- Volumetric heat addition $\dot{q_v} = 0$.
- Body force $f_{bx} = 0$.
- Constant wall temperature $\dot{q}_{nf} = -\dot{m}(c_f R_f(h_{aw} - h_w))/2A$, where h_w is evaluated using average c_p and $h_{aw} = h + r\frac{u^2}{2}$.

The derivatives without closed form expression and computed numerically (refer equations 3.18 and 3.19) are listed as follows:

$$\left(\frac{\partial h}{\partial p}\right)_{T,\phi} \quad ; \quad \left(\frac{\partial h}{\partial \phi}\right)_{p,T} \quad ; \quad \left(\frac{\partial Y_k}{\partial T}\right)_{p,\phi} \quad ; \quad \left(\frac{\partial Y_k}{\partial p}\right)_{T,\phi} \quad ; \quad \left(\frac{\partial Y_k}{\partial \phi}\right)_{p,T}$$

The MATLAB [27] implementation of the burner computation is detailed in the flowchart shown in Figure 4-23.

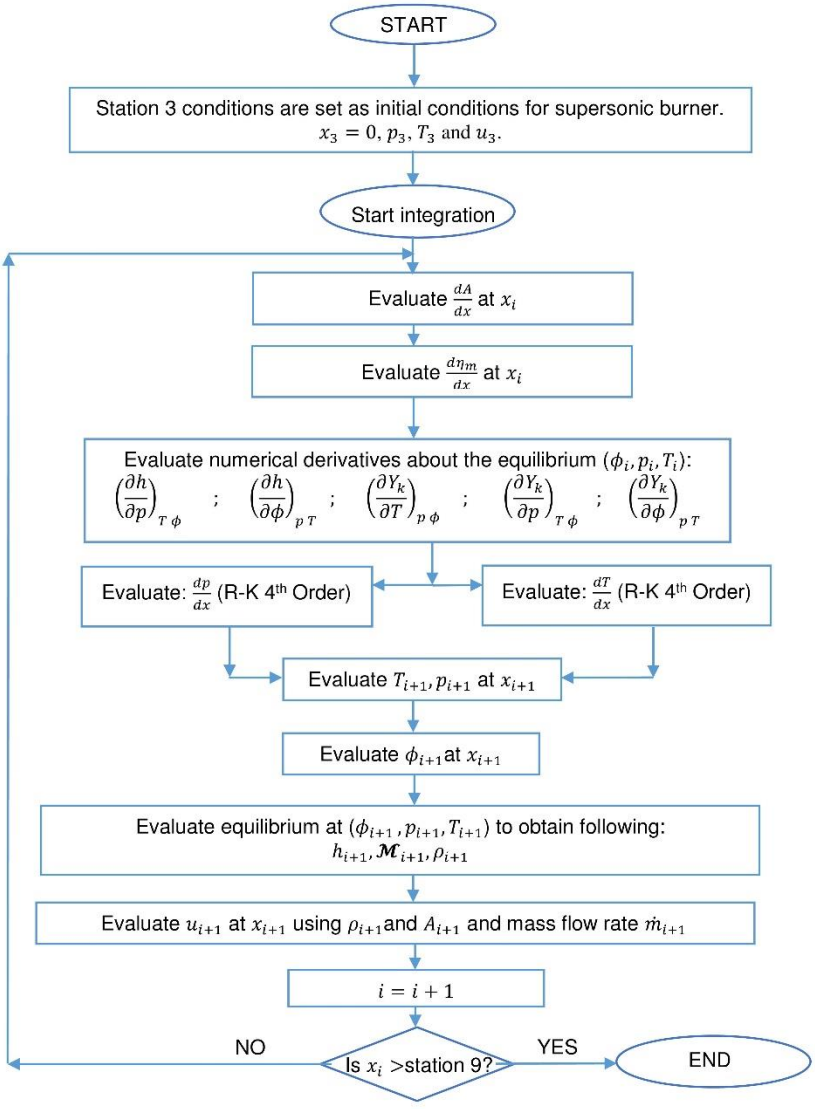

Figure 4-23: Flowchart for supersonic burner computation in MATLAB.

4.5.1.5 Non-Equilibrium Approximation

The non-equilibrium effects can be approximately captured using a method called "sudden freezing" of the equilibrium solution which was introduced by K.N.C. Bray [16]. Consider for example variation of a species concentration (Y_k) through a nozzle.

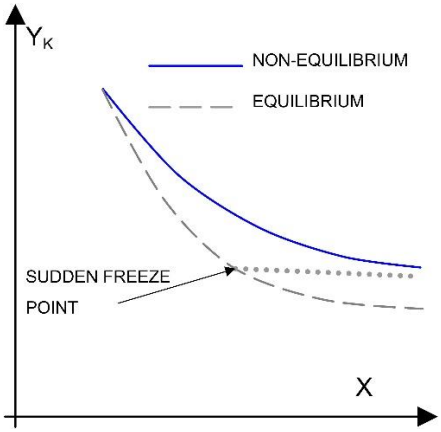

Figure 4-24: Schematic of sudden freezing technique for non-equilibrium approximation.

A schematic plot in Figure 4-24 provides insight into the "sudden freeze" method, where at some point in the nozzle the chemical equilibrium flow is switched to frozen flow wherein the species concentration remains constant downstream of the flow. This provides an approximate method to capture non-equilibrium effects. The non-equilibrium effects become predominant when the flow timescales are comparable to chemical timescales. Therefore the "sudden freeze" methodology provides a reduced order approach to obtain non-equilibrium effects without solving for chemical kinetics which drastically reduces computational load. An extension of "sudden freeze" for chemical non-equilibrium analysis can also be applied to thermodynamic non-equilibrium.

The next logical step is to find appropriate conditions for freezing (or locating the freeze point). In the current work, "sudden freeze" for chemical non-equilibrium analysis and thermodynamic non-equilibrium effects are carried out at different points. At first consider the "sudden freeze" technique for chemical non-equilibrium analysis.

When the flow time scale (τ_{FLOW}) is greater than chemical time scale (τ_{CHEM}), then the flow is approximately at chemical equilibrium. Whereas, when $\tau_{CHEM} \gg \tau_{FLOW}$, then the non-equilibrium effects are predominant making the flow almost chemically frozen. Therefore this can be summarized using the Damkohler number (Da_{chem}) defined as the ratio of flow time scale to chemical time scale.

$$Da_{chem} = \frac{\tau_{FLOW}}{\tau_{CHEM}} = \begin{cases} \gg 1, & Equilibrium \\ \ll 1, & Frozen \end{cases}$$

From the above definition, it can be seen that approximately when $Da_{chem} \approx 1$ becomes the appropriate point to initiate freezing. In the current work, individual mass flow rate of each species is frozen except the fuel's mass flow rate as it is changing due to mixing process. Therefore strictly the mass fraction is not frozen but species mass flow rates are frozen. The flow time scale is defined as:

$$\tau_{FLOW} = \frac{L_{CHAR}}{u} \tag{4.63}$$

where, L_{CHAR} represents the characteristic length (usually chosen as length of the burner and nozzle) and u being local velocity at each point in the flow. The chemical time scale is defined as the time required to reach 95% of the products starting with the reactants alone. For each reaction it is unique and a collective time scale for the combustion process is given as:

$$\tau_{CHEM} = \tau_{IGN} + \tau_{REAC} \tag{4.63}$$

where, τ_{IGN} is the ignition time delay and τ_{REAC} is the reaction time. For H_2-air combustion process, the ignition time delay and reaction time [14, 21] as a function of local pressure [Pa] and temperature [K] is given as:

$$\tau_{IGN} = 4.5 \times 10^{-9}(101325/p)\exp(10^4/T) \ \ [sec]$$

$$\tau_{CHEM} = 325 \times 10^{-6}(p^{-1.6})\exp(-0.8T/1000) \ \ [sec]$$

When the flow is frozen, the individual species are assumed to behave as a thermally perfect gas with their corresponding mass flow rates are frozen.

Apart from chemical non-equilibrium effects, thermodynamic non-equilibrium effects come into effect if flow times scales are really small when compared to relaxation time scales to reach thermodynamic equilibrium. When the sensible energy of the molecules in gas changes it continuously gets redistributed among different quantum modes and the time it takes to complete most of these redistributions is called the relaxation time (τ_{THERM}). For example, vibrational relaxation time is of particular interest as the specific heats change during the process of relaxation. So, to define Damkohler number (Da_{therm}) for the thermodynamic process, consider following definition:

$$Da_{therm} = \frac{\tau_{FLOW}}{\tau_{THERM}} = \begin{cases} \gg 1, & Equilibrium \\ \ll 1, & Frozen \end{cases}$$

From the above definition, it can be seen that approximately when $Da_{Therm} \approx 1$ becomes the appropriate point to initiate freezing. When the flow is frozen from thermodynamic equilibrium, the individual species are assumed to behave as calorically perfect gas. It is most likely that the thermodynamic timescales are less than chemical time scales. Therefore the flow gets first chemically frozen and then gets thermodynamically frozen. In the current work as most of the fluid flow is nitrogen (N_2), the vibrational relaxation time for N_2 in air [23] is used as thermodynamic time scale at local pressure [Pa] and temperature [K].

$$\tau_{THERM} = (1.2 \times 10^{-10}) \left(\left((9.86923267 \times 10^{-6}) p \right)^{-1} \right) \exp\left(130/T^{\frac{1}{3}} \right) \quad [sec]$$

The burner model implements both chemical “sudden freeze” and thermodynamic “sudden freeze” with appropriate calculations of flow parameters and thermodynamic variables (h, c_p, e, c_v, γ etc.). Using logical and loop statements in MATLAB platform, the burner model using chemical equilibrium with non-equilibrium approximation is implemented.

4.5.2 Subsonic Combustion

The subsonic combustion process inside a dual mode SCRamjet flow path is associated with a normal shock train inside the isolator. This shock train is unique for each fueling condition. Unlike the supersonic combustion where the core flow doesn't directly interact with the upstream flow, the subsonic combustion process involves interaction of upstream and downstream flow. The analysis detailed in this section for subsonic combustion analysis is mainly borrowed from the procedure detailed by Heiser and Pratt [25] with a few modifications.

At first the characterization of the typical subsonic (or ramjet) combustion mode in SCRamjet burner is discussed. Consider Figure 4-25, the schematic represents typical characterization of a subsonic burner and its corresponding Mach number variation along the burner axis.

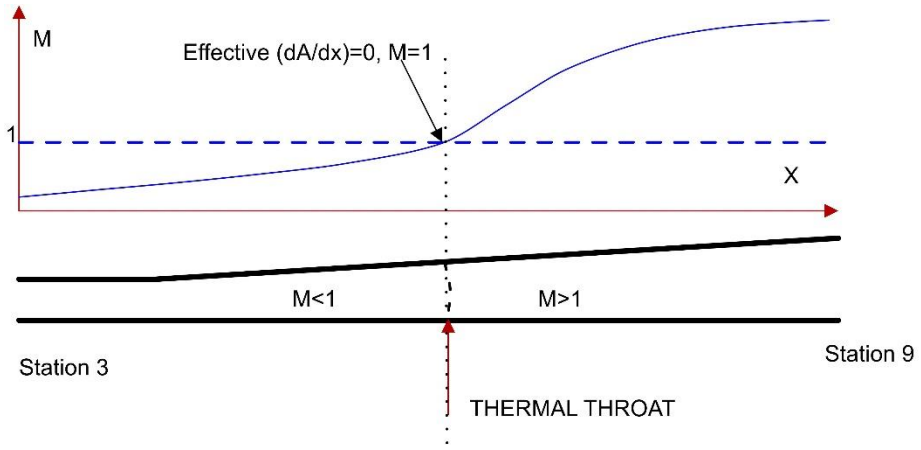

Figure 4-25: Schematic of subsonic combustion mode in SCRamjet burner.

The entrance Mach number at station 3 and the location of the thermal throat ($M = 1$) is decided by the flow path geometry and the fueling condition. As the subsonic mode involves interaction between upstream and downstream flow an iterative procedure using

chemical equilibrium solution will be time consuming. Therefore CPG assumptions are made with a representative γ_b for the flow being carefully chosen. The CPG equation governing the subsonic combustion mode operation (also valid for downstream supersonic flow beyond thermal throat) in terms of Mach number alone [25] is given in equation 4.64. Equation 4.64 only considers the effect of area and total temperature variation neglecting friction.

$$\frac{dM}{dx} = M\left(\frac{1+\frac{\gamma_b-1}{2}M^2}{1-M^2}\right)\left(-\left(\frac{1}{A}\frac{dA}{dx}\right)+\frac{1+\gamma_b M^2}{2}\left(\frac{1}{T_t}\frac{dT_t}{dx}\right)\right) \tag{4.64}$$

where,T_t represents the total temperature variation along the flow for which Heiser and Pratt [25] provide an algebraic fit. On the similar lines a modified analytical expression for total temperature variation is derived starting from energy conservation as follows:

$$c_p T_t = c_p T_{t3} + F_{AR} h_{pr}\, \eta_{mix} + q_{wall} \tag{4.65}$$

where, h_{pr} represents the specific heat of the reaction. Now differentiating the above equation gives:

$$c_p \frac{dT_t}{dx} = F_{AR} h_{pr} \frac{d\eta_{mix}}{dx} + \frac{dq_{wall}}{dx} \tag{4.66}$$

Therefore, by assuming the adiabatic wall temperature (T_{aw}) as the total temperature of the flow and using Stanton number relation for wall heat transfer term $\frac{dq_{wall}}{dx}$ with $R_f = 1$, we obtain the ODE equation for total temperature variation given by:

$$\frac{dT_t}{dx} = \frac{F_{AR} h_{pr}}{c_p}\frac{d\eta_{mix}}{dx} + \frac{2c_f(T_w - T_t)}{D_{Hb}} \tag{4.67}$$

An analytical solution to the above ODE using integrating factor method gives:

$$T_t(x) = \frac{1}{e^{\int_{x_0}^{x}\frac{2c_f}{D_{HB}}dx}}\int_{x_0}^{x} e^{\int_{x_0}^{x}\frac{2c_f}{D_{HB}}dx}\left(\frac{f h_{pr}}{c_p}\frac{d\eta_{mix}}{dx} + \frac{2c_f}{D_{Hb}}T_w\right)dx \tag{4.68}$$

Now using equation (4.64) with a known T_t distribution using equation (4.68), the solution procedure to evaluate ramjet mode is discussed in the following paragraphs.

To begin the subsonic (or ramjet) mode analysis, the location of the thermal throat is first determined. To find the thermal throat location, the effective area derivative is defined in equation (4.69), which represents the net effect of physical area variation and total temperature variation.

$$\left(\frac{1}{A_{eff}}\frac{dA_{eff}}{dx}\right)=\left(-\left(\frac{1}{A}\frac{dA}{dx}\right)+\frac{1+\gamma_b M^2}{2}\left(\frac{1}{T_t}\frac{dT_t}{dx}\right)\right) \tag{4.69}$$

At the thermal throat ($*$) there is eclipse of two following conditions:

$$\left(\frac{1}{A_{eff}}\frac{dA_{eff}}{dx}\right)_*=0$$

$$M_*=1$$

This gives the following algebraic equation which has to be solved to find the location of thermal throat at a distance x_* from station 3.

$$\left(\frac{1}{A}\frac{dA}{dx}\right)_*-\frac{1+\gamma_b}{2}\left(\frac{1}{T_t}\left(\frac{dT_t}{dx}\right)\right)_*=0 \tag{4.70}$$

Note that in the above equation the area variation term is obtained from the geometry of the burner-internal nozzle flow path. The total temperature term can be obtained from equations 4.68 and 4.67. Note that in the equations 4.68 and 4.67, a generalized parametric fit for subsonic mixing efficiency can be used as follows:

$$\eta=\eta_b\left(\frac{\nu\frac{x}{L_c}}{1+(\nu-1)\frac{x}{L_c}}\right)$$

The term η_b is the maximum mixing efficiency and the term L_c is the characteristic length which is usually the length of the combustion chamber. The variable ν is the fit parameter which for subsonic combustion varies from 40-50 [25]. The next step is to find the Mach

number distribution through the burner. The starting point for the evaluation would be the thermal throat where the Mach number (=1) is known. At first a short discussion on singularity treatment at $M = 1$ in governing equation 4.64 is discussed. It can be seen that from equation 4.64 the $(1 - M^2)$ in the denominator drives the Mach number derivative to indeterminate value when close to thermal throat ($M \sim 1$). Therefore L'hospital's rule is applied to the governing ramjet mode equation (4.64) near thermal throat and the following equation (4.71) [25] is obtained. Note that equation (4.71) is a replacement for equation 4.64 only near the vicinity of the thermal throat say $0.99 < M < 1.01$.

$$\left.\frac{dM}{dx}\right|_* = \frac{1}{4}\left(-\Omega^* + \sqrt{\Omega^{*2} - 4\Psi^*}\right) \tag{4.71}$$

where,

$$\Omega^* = \gamma_b \left(\frac{1}{A}\frac{dA}{dx}\right)_*$$

$$\Psi^* = (\gamma_b - 1)\left(\frac{1}{A}\frac{dA}{dx}\right)_*^2 - (1 + \gamma_b)\left(\frac{1}{A}\frac{d^2A}{dx^2}\right)_* + \frac{(1 + \gamma_b)^2}{2}\left(\frac{1}{T_t}\frac{d^2T_t}{dx^2}\right)_*$$

With equation (4.64) for $M \neq 1$ and equation (4.70) for $(0.99 < M < 1.01)$ the governing equation for ramjet mode is complete. The next step is to discuss the solution method for ramjet mode. The integration starts from thermal throat where Mach number is known ($M = 1$). A back step integration using Runge-Kutta 4th order method [30] is carried out using equation (4.70) followed by equation (4.64) to find the entrance Mach number at station 3. Note that injector drag is neglected for the ramjet mode and the area variation across it is accounted using simple isentropic relationship, therefore, the station 3 Mach number obtained from back integration is used to find corresponding station 2.5 Mach number. With this Mach number at station 2.5 imposed, the isolator is solved for normal shock train mode as detailed in section 4.3.2 to obtain the corresponding pressure, temperature velocity and density.

To see the importance of entry Mach number imposed by back integration and to carryout successful forward integrating, consider Figure 4-26. If the entrance Mach number for forward integration is slightly less for the same fueling condition, the forward integration never chokes, whereas if it is slightly more the solution chokes with $dA_{eff}/dx \neq 0$. Therefore only one single solution for entrance Mach number exist which is obtained from back integration.

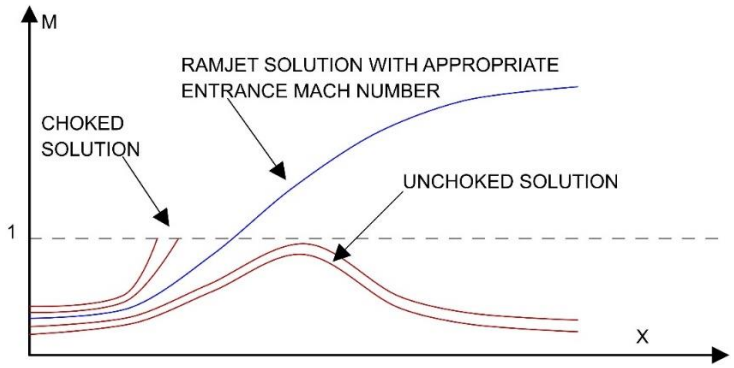

Figure 4-26: Schematic plot showing the effect of entry Mach number on ramjet mode computation.

It is clear at this point that the entrance Mach number should be exactly matched with back integration result. But the normal shock train model presented in section 4.3.2 provides a close match to the imposed Mach number but not an exact match. Therefore a small force (numerical correction) is added to match the exact imposed Mach number at station 3. This is done by using the impulse function concept and mass flow parameter as detailed in Appendix D. With the corresponding corrected conditions at station 3 matched exactly with back integration result, the forward integration is carried out using equation (4.64) and (4.70) Upon completing the forward integration by passing through the thermal throat, the Mach number distribution from station 3 to 9 is used to obtain distribution of temperature, pressure and velocity in equation (4.71), (4.72) and (4.73) respectively.

$$T(x) = T_3 \frac{T_t(x)}{T_{t3}} \left[\frac{\left(1 + \frac{\gamma_b - 1}{2} M_3^2\right)}{\left(1 + \frac{\gamma_b - 1}{2} M(x)^2\right)} \right] \tag{4.71}$$

$$p(x) = \frac{p_3 A_3}{A(x)} \frac{M_3}{M(x)} \sqrt{\frac{T(x)}{T_3}} \tag{4.72}$$

$$u(x) = \frac{u_3 M(x)}{M_3} \sqrt{\frac{T(x)}{T_3}} \tag{4.73}$$

The ramjet mode solution methodology proposed in this section is summarized in the following flow chart (Figure 4-27).

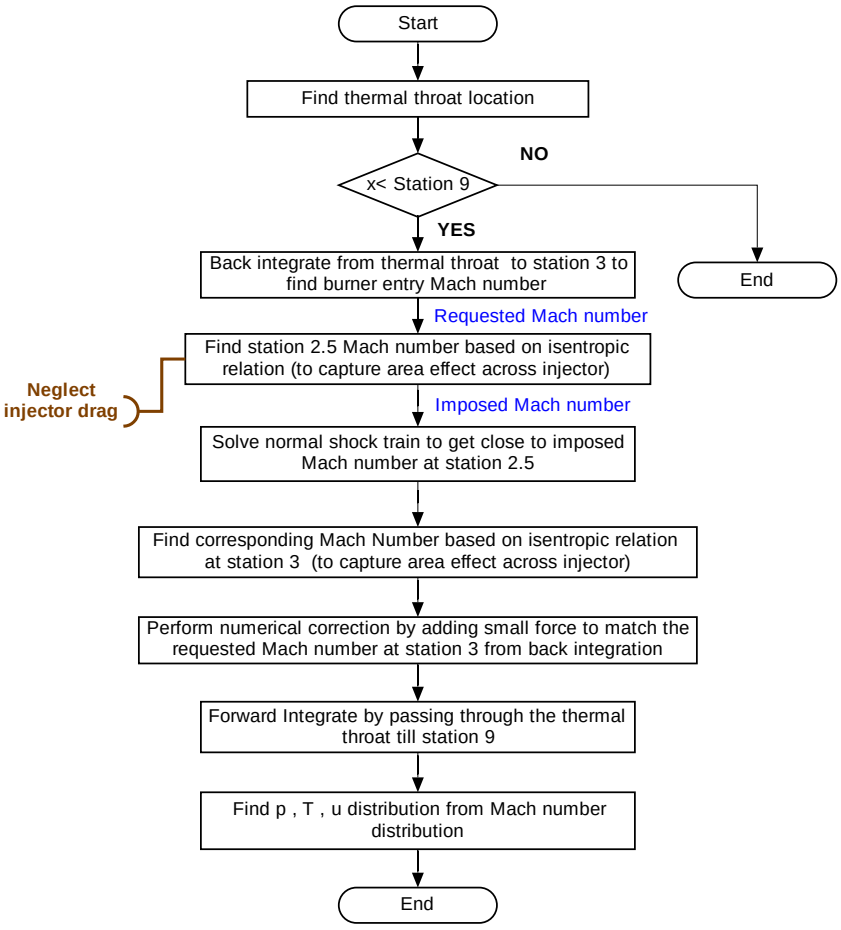

Figure 4-27: Flow chart for ramjet mode solution procedure.

4.5.3 Isolator Burner Interaction

In this section the solution method to determine the conditions at which the bifurcation of isolator-burner operating modes occur is discussed. Consider following flow chart as shown in Figure 4-28 implemented in MATLAB. At first the isolator-burner is solved assuming shock free mode (or mode A). The results of which are then inspected for separation. The separation criteria used is detailed in equation (4.74) [25].

$$\left(\frac{M_d}{M_3}\right) < \begin{cases} 0.898, & Laminar \\ 0.762, & Turbulent \end{cases} \tag{4.74}$$

Where, M_d represents the minimum downstream Mach number inside the burner obtained in mode-A solution. Also M_3 corresponds to the station 3 Mach number for shock-free isolator-burner solution. If the condition in equation (4.74) is met the oblique shock train inside the isolator is computed using the wedge model. The maximum pressure obtained from mode-A solution is used as back pressure for the oblique shock train model. If the back pressure imposed is less than the maximum back pressure that is supported by the wedge model with attached oblique shocks, then, the engine is assumed to operate in oblique shock train mode (or mode B). For mode-B operation the reattachment point is assumed to be at the location of maximum pressure in mode-A solution. The separated area (A_{sep}) is assumed to be constant until the burner section in which it reattaches with a linear curve fit. Say for example if the re-attachment point is located in the variable area section of the burner (Figure 4-21) then, A_{sep} is assumed to be constant till station 3.5 following which a linear curve fit from A_{sep} to $A_{sep} = 0$ is made between station 3.5 and the re-attachment point.

If the maximum pressure obtained from mode-A solution exceeds the maximum pressure that the wedge model can provide with attached oblique shocks, then the engine is assumed to operate in ramjet mode (or mode C). Following which the thermal throat is

located and back integration is carried out to impose appropriate entrance Mach number for the burner. If this imposed Mach number is less than minimum Mach number that normal shock train can provide, then the engine is assumed to be unstart.

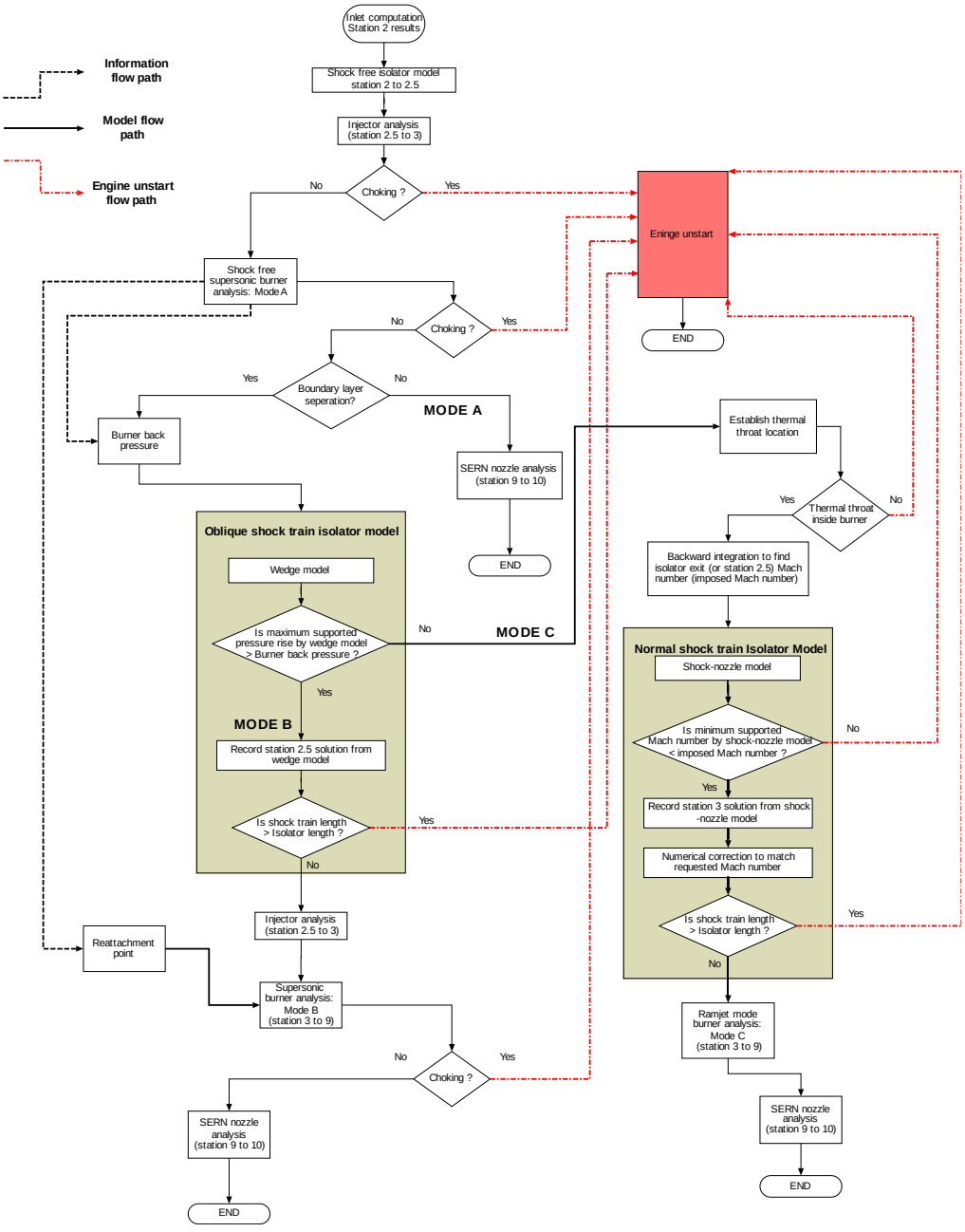

Figure 4-28: Flow chart of isolator-burner interaction model implemented in MATLAB.

4.6 External Nozzle Model

An analytical model for a single expansion ramp nozzle (SERN) at on-design and off-design conditions is presented in this section. The core flow of the nozzle is analyzed with one-dimensional fidelity similar to the burner model presented in section 4.5. The external aerodynamics is coupled with the internal flow inside the nozzle to analyze off-design conditions. Before presenting the details of the analytical model for SERN, consider a brief discussion on flow inside SERN as depicted in Figure 4-29.

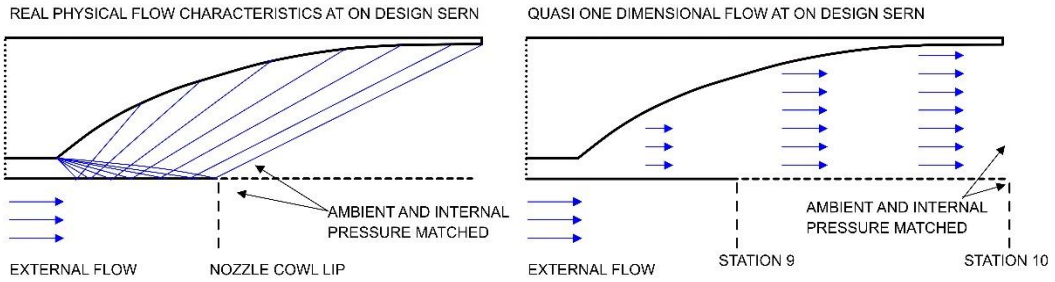

Figure 4-29: Schematic diagram comparing real physical flow field inside SERN to quasi one-dimensional equivalent.

At on-design condition, a series of Prandtl-Meyer expansion fans originates at station 4 as shown in Figure 4-29 which then reflects from cowl and finally gets cancelled at the ramp surface of the nozzle. It can be seen from Figure 4-29 that all the expansion process is complete at the cowl lip when the nozzle is operating at on-design and the slip line between internal flow and external flow is along the external flow undisturbed. An equivalent quasi-one dimensional flow provides average flow parameters at a distance 'x' from station 4. Therefore, the averaged pressure distribution at design point obtained from quasi one dimensional analysis is matched with the external pressure at station 10 and not at the cowl lip. It can be concluded that a quasi-one dimensional analysis with undisturbed slip line provides the station 10 pressure which can be compared with external pressure to determine whether the nozzle is operating at design point ($(p_{10})_{design} = p_{external}$), under-

expanded ($(p_{10})_{design} > p_{external}$) or over-expanded ($(p_{10})_{design} < p_{external}$)). Now, that a method for determining SERN operating mode is presented, the next step is to trace the slip line at off-design conditions (over/under-expanded).

In real phenomenon, the slip line is a curve whose structure is decided by complex interaction of shock and expansion waves on either side of it. To simplify the complexity the analytical model assumes the slip line to be a straight line that can be oriented along different directions to match the pressure at station 10. This provides us a starting point to model off-design conditions by reducing the complexity of the analysis. An iterative procedure is required to match the pressure at station 10 if the flow inside the nozzle is assumed to be at chemical equilibrium which is computationally expensive. Therefore to find the approximate orientation of the slip line, CPG analysis of is used. Upon finding the slip line orientation using CPG analysis, the internal flow can be re-computed with chemical equilibrium similar to the burner model presented in section 4.5. Note that the internal nozzle is a part of the burner analysis, therefore the analysis of external SERN from station 9 to 10 is presented in three parts as follows:

4.6.1 On-Design SERN Analysis

At on-design mode, the slip line is oriented along the external flow with the pressure internal pressure match at station 10 (p_{10}) matched with the external unaltered flow pressure (p_a). The height of the 2D cross-section at station 10 for design point is represented as $H_{10\,D}$ as shown in Figure 4-30. The core flow of external nozzle for mode-A and mode-B burner operation is analyzed similar to supersonic burner model presented in section 4.5.1 by neglecting wall friction and heat transfer effects. However, when the burner operates in mode-C, the flow inside external nozzle is analyzed with CPG formulation with representative ratio of specific heats (γ_b).

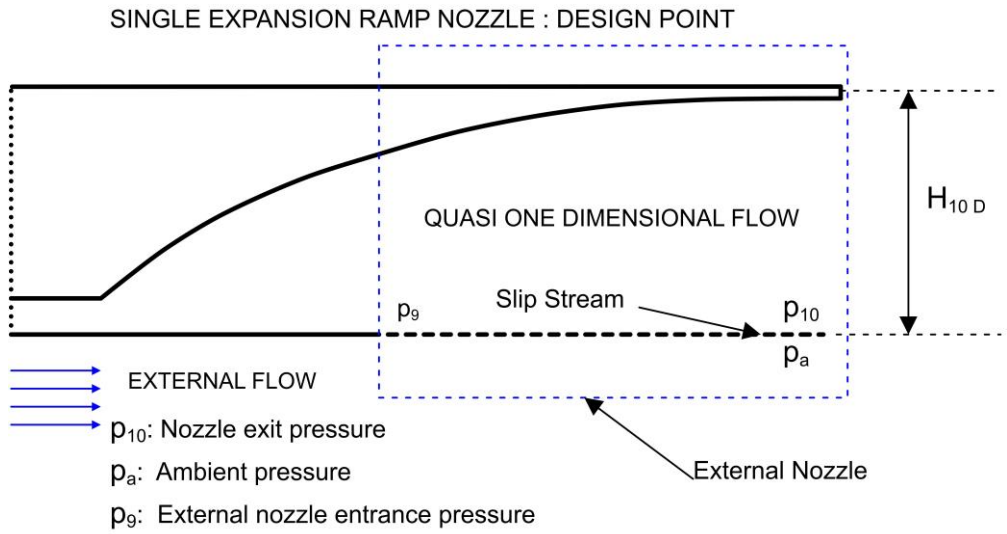

Figure 4-30: Schematic diagram of on-design analytical model of SERN.

4.6.2 Off-Design SERN Analysis: Over-Expanded Nozzle

At first, the SERN is analyzed at on-design using the procedure detailed in section 4.6.1 to determine whether or not the nozzle is operating at over-expanded mode. The over-expanded mode is established when the ambient pressure (p_a) is greater than design-point nozzle exit pressure $p_{10\,D}$. For the nozzle core flow an average representative $\bar{\gamma}$ to carry out CPG analysis is evaluated. The slip line orientation is determined by matching the nozzle exit pressure (p_{10}) and the external pressure (p_{ea}). This is done by using the CPG area-Mach number relationship [26] for the nozzle core flow and Prandtl-Meyer expansion for the external flow as shown in Figure 4-31. To mathematically present this model consider the CPG area-Mach number relation in equation (4.25) represented in functional form as follows:

$$\frac{A}{A^*} = f_{\frac{A}{A^*}}(M,\gamma) \qquad \text{or} \qquad M = f^{-1}_{\frac{A}{A^*}}\left(\frac{A}{A^*},\bar{\gamma}\right) \tag{4.75}$$

The Prandtl-Meyer function [26] to compute external aerodynamics is given as follows:

$$\nu(M) = \sqrt{\frac{\gamma+1}{\gamma-1}}\tan^{-1}\left(\sqrt{\frac{\gamma-1}{\gamma+1}(M^2-1)}\right) - \tan^{-1}\left(\sqrt{M^2-1}\right) \qquad (4.76)$$

The core flow area of the nozzle is given by $A = Hd_z$, where d_z is the depth of the nozzle and H is the 2D height of the nozzle flow.

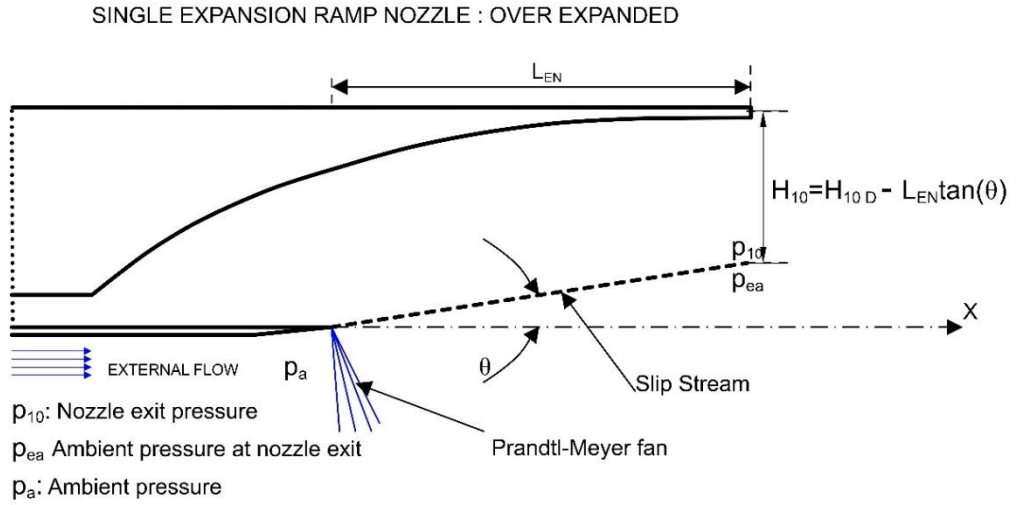

Figure 4-31: Schematic diagram of off-design over-expanded analytical model of SERN.

Consider the external flow pressure to be p_a. Upon Prandtl-Meyer expansion the final pressure is p_{ea}. To satisfy the condition $p_{ea} = p_{10}$, the CPG area-Mach number relation (equation 4.75) and the Prandtl-Meyer function (equation 4.76) are used to find appropriate nozzle exit area (A_{10}). If $A_{10\,D}$ is the design point exit core flow area then two non-linear simultaneous equations (4.77 and 4.78) are solved in MATLAB to obtain H_{10} and M_{ae}. When the exit flow 2D height is determined then the corresponding inclination of slip line is given by $\tan\theta = (H_{10\,D} - H_{10})/L_{EN}$. If the burner operates in mode-A or mode-B then, with the known θ, the external nozzle core flow can be recomputed using supersonic burner model presented in section 4.5.1 by neglecting wall friction and heat transfer effects.

However, if the burner operates in mode-C, the CPG solution is computed using area-Mach number relation.

$$p_a\left(\frac{1+\frac{\gamma_a-1}{2}M_a^2}{1+\frac{\gamma_a-1}{2}M_{ae}^2}\right)^{\frac{\gamma_a}{\gamma_a-1}} - p_9\left(\frac{1+\frac{\bar{\gamma}-1}{2}M_9^2}{1+\frac{\bar{\gamma}-1}{2}\left(f_{\frac{A}{A^*}}^{-1}\left(\frac{H_{10}d_z}{H^*d_z},\bar{\gamma}\right)\right)^2}\right)^{\frac{\bar{\gamma}}{\bar{\gamma}-1}} = 0 \quad (4.77)$$

$$\nu(M_{ae}) - \nu(M_a) - \tan^{-1}\left(\frac{H_{10\,D}-H_{10}}{L_{EN}}\right) = 0 \quad (4.78)$$

4.6.2 Off-Design SERN Analysis: Under-Expanded Nozzle

At first, the SERN is analyzed at on-design using the procedure detailed in section 4.6.1 to determine whether or not the nozzle is operating at under-expanded mode. The under-expanded mode is established when the ambient pressure (p_a) is less than design-point nozzle exit pressure $p_{10\,D}$. For the nozzle core flow an average representative $\bar{\gamma}$ to carry out CPG analysis is evaluated. The slip line orientation is determined by matching the nozzle exit pressure (p_{10}) and the external pressure (p_{ea}). This done by using CPG area-Mach number relationship (equation 4.75) [26] for the nozzle core flow and CPG shock relations ($\theta-\beta-M$) [26] for the external flow as shown in Figure 4-32. To mathematically present this model consider the pressure ratio (p_d/p_u) across CPG shock represented in functional form as follows:

$$\frac{p_d}{p_u} = f_{\theta\beta M}(\theta, M, \gamma) \quad (4.79)$$

Consider the external flow pressure to be p_a. The final pressure after the shock is p_{ea}. To satisfy the condition $p_{ea} = p_{10}$, the CPG area-Mach number relation (equation 4.75) and pressure ratio across CPG shock (equation 4.79) are used to find appropriate nozzle exit area (A_{10}). If $A_{10\,D}$ is the design point exit core flow area then the non-linear

simultaneous equations (4.80) is solved in MATLAB to obtain θ. If the burner operates in mode-A or mode-B then, with the known θ, the external nozzle core flow can be recomputed using supersonic burner model presented in section 4.5.1 by neglecting wall friction and heat transfer effects. However, if the burner operates in mode-C, the CPG solution is computed using the area-Mach number relation.

$$p_a\, f_{\theta\beta M}(\theta, M_a, \gamma_a) - p_9 \left(\frac{1 + \frac{\bar{\gamma}-1}{2} M_9^2}{1 + \frac{\bar{\gamma}-1}{2} \left(f_{\frac{A}{A^*}}^{-1} \left(\frac{H_{10} d_z}{H^* d_z}, \bar{\gamma} \right) \right)^2} \right)^{\frac{\bar{\gamma}}{\bar{\gamma}-1}} = 0 \qquad (4.80)$$

Where $H_{10} = H_{10\,D} + L_{EN} tan(\theta)$.

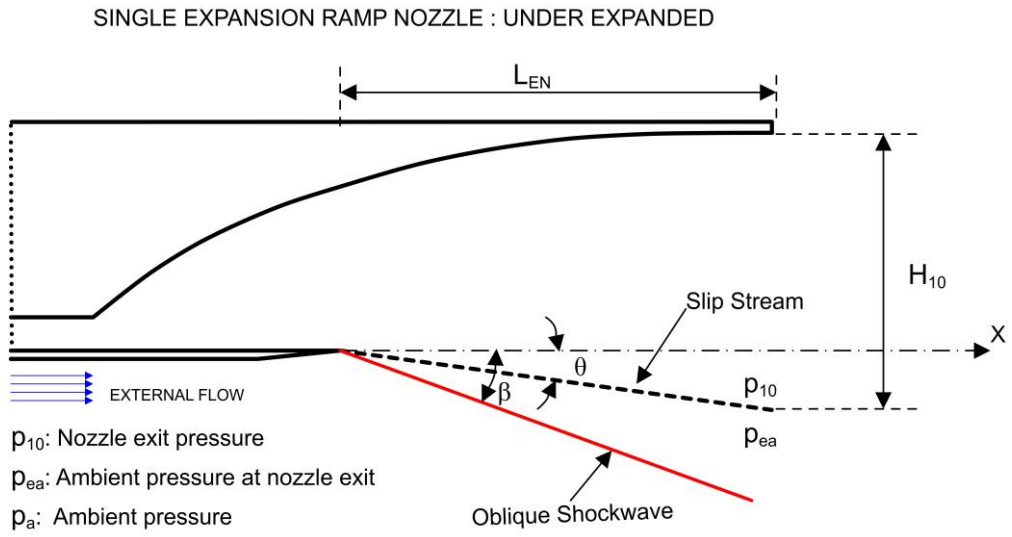

Figure 4-32: Schematic diagram of off-design under-expanded analytical model of SERN.

To conclude this section, a brief solution procedure of the analytical SERN model implemented in MATLAB [27] platform is presented in a flowchart in Figure 4-33.

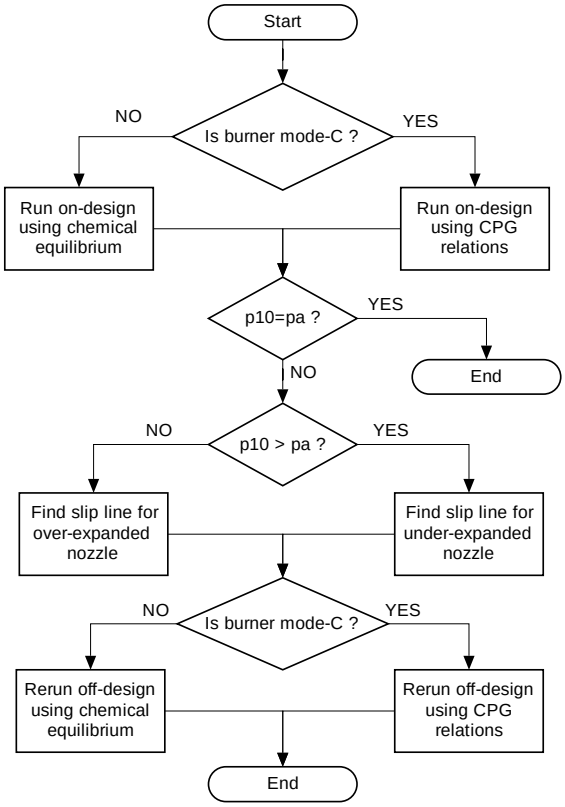

Figure 4-33: Flowchart of SERN analytical model implemented in MATLAB.

Chapter 5

Validation of Analytical Dual Mode SCRamjet Model

The model proposed for analyzing the SCRamjet flow path in Chapter 5 is validated in this chapter. The validation process first corroborates the physics used in the model following which the model is validated with both experimental and computational results available in the existing literatures [9, 2, 20].

5.1 SCRamjet Inlet Model Validation

The thermally perfect oblique shockwave model presented in section 4.2.1 is validated with the NASA report [40]. The upstream conditions used for validating the oblique shock model presented in section 4.2.1 are detailed in Table 5.1. The post shock Mach number M_p, shock angle β and temperature ratio across the shock $Tr = T_p/T_0$ are validated in Table 5-2, 5-3 and 5-4 respectively. The number of significant digits were limited to two and the corresponding percentage error in all the variables were less than 0.01%.

Table 5-1 Upstream Oblique Shock Conditions for Validation.

CASE ID	T_0[K]	M_0	$\Delta\theta$ [deg]
OS I	222.3	2.0	20.0
OS II	185.9	2.4	20.0
OS III	142.8	3.0	20.0
OS IV	120.7	3.4	20.0
OS V	95.2	4.0	20.0

Table 5-2 Validation of Post Shock Mach Number.

CASE ID	NASA M_p [40]	TPG Shock Model M_p	$\Delta\epsilon\%$
OS I	1.21	1.21	$< 10^{-2}$
OS II	1.57	1.57	$< 10^{-2}$
OS III	1.99	1.99	$< 10^{-2}$
OS IV	2.24	2.24	$< 10^{-2}$
OS V	2.57	2.57	$< 10^{-2}$

Table 5-3 Validation of Oblique Shockwave Angle.

CASE ID	NASA β [40]	TPG Shock Model β	$\Delta\epsilon\%$
OS I	53.42	53.42	$< 10^{-2}$
OS II	44.35	44.35	$< 10^{-2}$
OS III	37.77	37.78	$< 10^{-2}$
OS IV	35.15	35.15	$< 10^{-2}$
OS V	32.48	32.48	$< 10^{-2}$

Table 5-4 Validation of Temperature Ratio Across Oblique Shockwave.

CASE ID	NASA Tr [40]	TPG Shock Model Tr	$\Delta\epsilon\%$
OS I	1.39	1.39	$< 10^{-2}$
OS II	1.44	1.44	$< 10^{-2}$
OS III	1.56	1.56	$< 10^{-2}$
OS IV	1.65	1.65	$< 10^{-2}$
OS V	1.81	1.81	$< 10^{-2}$

The next step is to validate the inlet model with experimental and computational results [9, 20]. At first experimental data provided by NASA [9] is used for validation. The inlet geometry for experimental investigation by NASA [9] (Figure 5-1) exactly takes the form of parametrized inlet geometry considered in the current work (Figure 5-1). Note that the geometrical notations used by NASA is different from the ones used in the current work. The experiments by NASA [9] were carried out at free stream Mach number $M_0 = 4.03 \pm 0.02$ for different geometrical configurations of the inlet at 0^0 angle of attack.

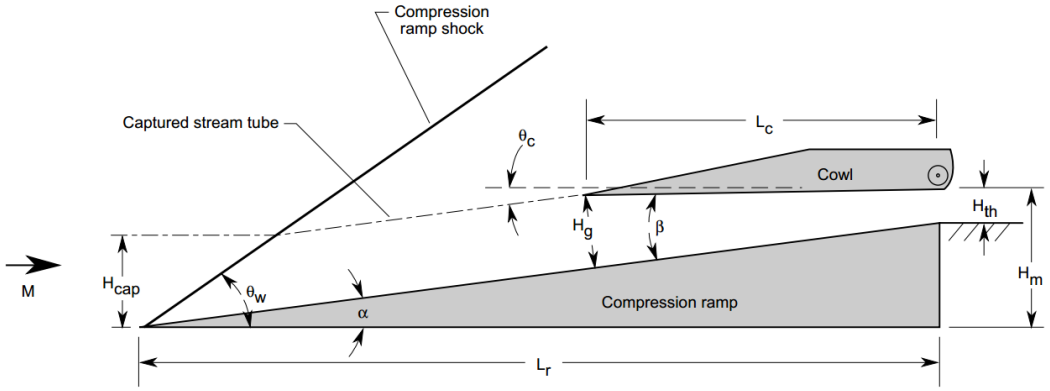

Figure 5-1 Inlet considered by NASA for experimentation [9].

The geometrical design parameters considered by NASA [9] (Figure 5-1) and its equivalent parameters in the analytical model are detailed in Table 5-5. The experimental work by NASA [9] provides the pressure variation along the ramp and cowl surfaces. For the validation, “thin boundary layer” case data is considered, where the experiments were carried out without a flat plate upstream of the inlet. Three cases were considered for experimental validation and their details are tabulated in Table 5-6.

Table 5-5 Geometrical Parameters of NASA’s Inlet [9].

NASA [9] geometrical parameter	Description of geometrical parameters	Equivalent analytical model parameter	Design values/range SI units
β	Inlet convergence angle	$\theta_N - \theta_{COWL}$	3.0^0 to 9.7^0 [deg]
L_c	Cowl length	L_{COWL}	0.11176 [m]
H_{th}	Inlet throat height	H_{TH}	0.01016 [m]
α	Compression ramp angle	θ_N	11^0 [deg]
L_r	Ramp total length	L_N	0.248158 [m]

Table 5-6 Validation Case Configuration Data [9].

CASE ID	M_0	p_0 [pa]	θ_{COWL}	L_{COWL}/H_{TH}
EIV I	4.03±0.02	8728±234	5^0	11.0
EIV II	4.03±0.02	8728±234	4^0	11.0
EIV III	4.03±0.02	8728±234	2^0	11.0

The cold flow free stream generated in experiments by NASA [9] had total temperatures varying from 300K to 277K. Therefore, at Mach 4.03, the static temperatures should have been really low (<100K). The normalized pressure on the ramp and cowl surfaces are obtained from the analytical model and compared with the corresponding experimental data [9] in Figure 5-2, 5-3 and 5-4. The x-axis of the plot is a measure of axial distance from the global axis normalized with respect to throat height H_{TH}.

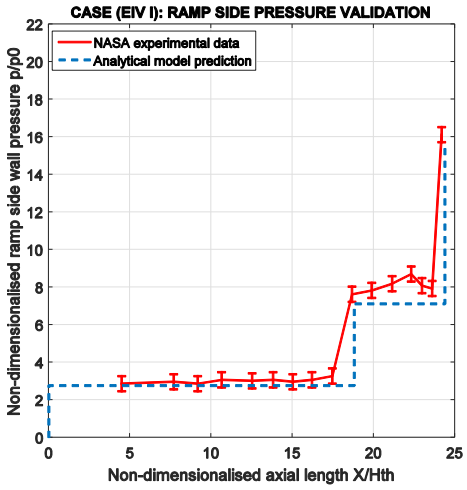

(a)

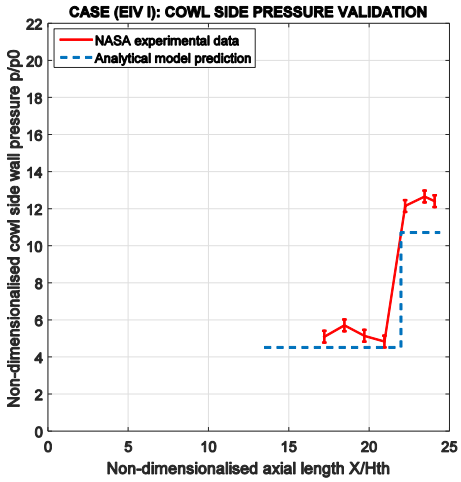

(b)

Figure 5-2 Validation of normalized pressure profile of EIV I case. (a) Ramp side wall pressure comparison. (b) Cowl side wall pressure comparison.

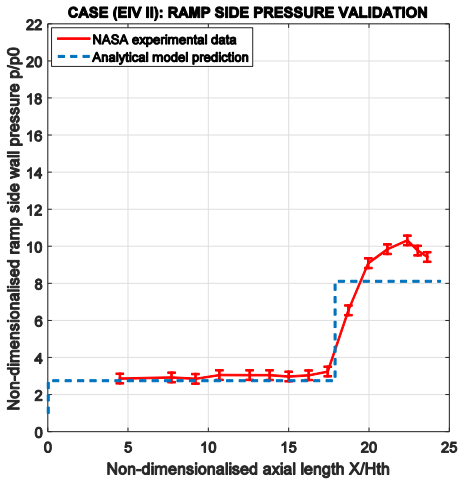

(a)

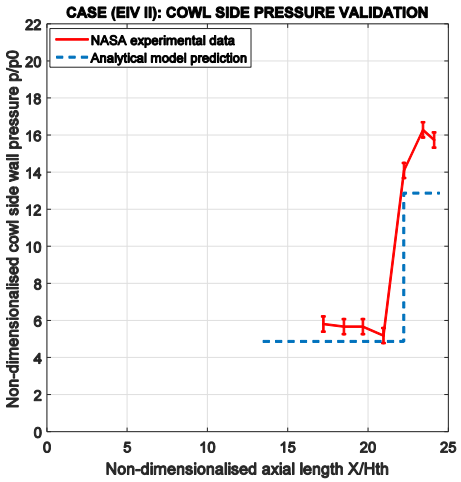

(b)

Figure 5-3 Validation of normalized pressure profile of EIV II case. (a) Ramp side wall pressure comparison. (b) Cowl side wall pressure comparison.

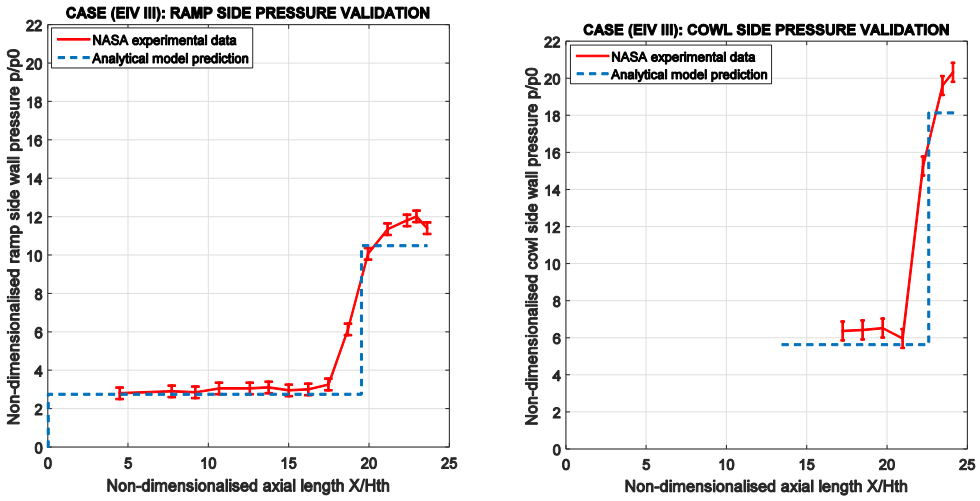

(a) (b)

Figure 5-4 Validation of normalized pressure profile of EIV III case. (a) Ramp side wall pressure comparison. (b) Cowl side wall pressure comparison.

From the Figures 5-2, 5-3 and 5-4, the analytical model predicts the location of the shock reflections and the corresponding pressure rise quite accurately. The average absolute error ($\%|\Delta\epsilon_p|$) between analytically predicted shock pressure profiles and the experimental data [9] is tabulated in Table 5-7.

Table 5-7 Average Error Between Analytical and Experimental Pressure Profiles.

CASE ID	$\%\left\|\Delta\epsilon_p\right\|_{RAMP\ SIDE}$	$\%\left\|\Delta\epsilon_p\right\|_{COWL\ SIDE}$
EIV I	7.79	13.19
EIV II	11.61	16.39
EIV III	8.99	9.99

From the Table 5-7 it can be seen that the analytical model predicts the shock pressure profiles with an accuracy of 83% to 92%. The pressure profile generated by the analytical model (Figure 5-2, 5-3 and 5-4) slightly under predicts the pressure rise. This is because it doesn't account for the side wall viscous effects while performing the shock reflections, however, the side wall viscous effects are taken into considerations at the throat

by correcting the flow using control the volume method detailed in section 4.2.3. Another reason that can be attributed to a lower pressure rise prediction by the analytical model is that the fore shock is affected by the bluntness of the nose and cowl lip which the analytical model ignores.

The experimental investigation by NASA [9] provides an estimate of throat Mach number at station 2 that was obtained indirectly from other measured quantities. The station 2 results obtained from analytical model with and without the viscous correction are compared with the estimated throat Mach number provided by NASA [9] in Table 5-8.

Table 5-8 Validation of Station 2 Mach Number.

CASE ID	NASA [9] estimated M_2	Analytical viscous model M_2	$\|\Delta\epsilon\|_{viscous}$ %	Analytical inviscid model M_2	$\|\Delta\epsilon\|_{inviscid}$ %
EIV I	2.37	2.42	2.11	2.65	11.81
EIV II	2.15	2.18	1.40	2.35	9.30
EIV III	1.81	1.88	3.72	2.04	12.7

From Table 5-8 it can been that the viscous correction model which comprises of δ^* correction and side wall viscous correction, predicts the Mach number at station 2 with ~98% accuracy. Also, the inviscid model prediction has lesser accuracy when compared to the viscid prediction. This substantiates the importance of viscous correction while performing super/hypersonic inlet calculations.

The next validation of the inlet is carried out with computational results provided by Vijayakumar and Wilson [20, 2]. The two-dimensional computational study of inlet-isolator carried out by Vijayakumar [2], simulated a flight envelope of Mach number 3.5 to 6 along a constant dynamic pressure trajectory $q_0 = 47800\ N/m^2$. The conditions at station 2 were provided by Vijayakumar [2] which were validated with the corresponding analytical model results. The validation pf off-design conditions ($M_0 = 4$ and M_0=5.5) and on-design condition ($M_0 = 6$) is carried out in Table 5-9.

Table 5-9 Validation Case Configuration Data.

Case ID	M_0	p_0[Pa]	T_0[K]	Altitude [km]
CIV I	4.0	4204	218.3	21.7
CIV II	5.5	2223	222.4	25.5
CIV III	6.0	1867	223.5	27.0

The inlet geometry considered by Vijayakumar [2] was a single ramp type inlet with cowl and its equivalent geometrical parameters for the analytical study are tabulated in Table 5-10.

Table 5-10 Validation Case Geometrical Data [2].

Equivalent analytical model parameter	Design values (SI units)
θ_{COWL}	0^0 [deg]
θ_N	3.65^0 [deg]
α_{AoA}	0^0 [deg]
L_{COWL}	6.083 [m]
H_{TH}	0.152 [m]
d_z	0.608[m]
L_N	9.687 [m]

To simulate Vijayakumar's [2] 2D-computational study, the analytical model was modified by disconnecting the side-wall viscous correction from the inlet model as there was no side wall effect. From the Table 5-10, it can be inferred that the cowl is completely open ($\theta_{COWL} = 0$) at zero angle of attack. By referring to equation 4.19, it can be observed that adding δ^* correction to the cowl makes the cowl angle negative ($\theta^*_{COWL} < 0$) which the analytical model cannot handle. Therefore, the viscous effect due to cowl is modelled using a correction force on a control volume located at the throat instead of δ^* type correction.

The shock patterns corresponding to Vijayakumar's [2] 2D-computational study are obtained from the analytical model and plotted in Figure 5-6, 5-7 and 5-8.

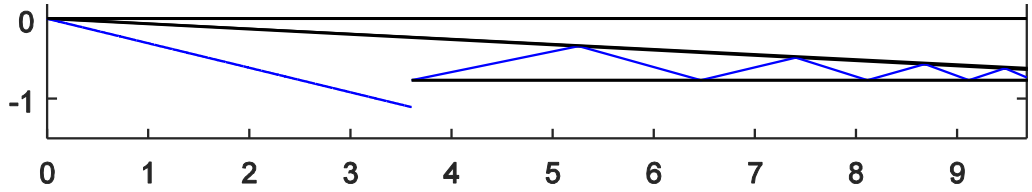

Figure 5-5 Shock pattern obtained from analytical model for (CIV I)-case.

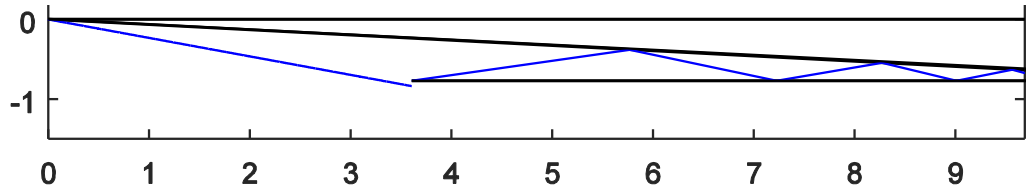

Figure 5-6 Shock pattern obtained from analytical model for (CIV II)-case.

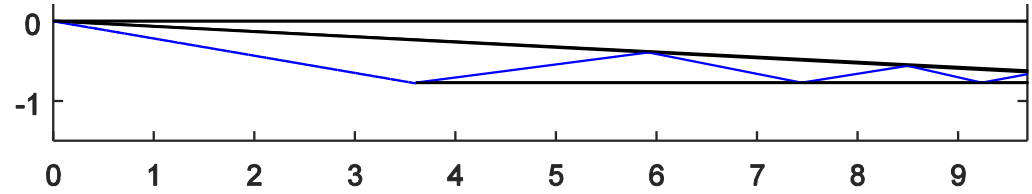

Figure 5-7 Shock pattern obtained from analytical model for (CIV III)-case.

The on-design condition claimed by Vijayakumar [2] in the inlet study is characterized in Figure 5-7. It can be seen that the shock on-lip criteria and shock cancellation near the throat is achieved by the analytical model. The number of shocks at on-design condition predicted by the analytical model is six and it is consistent with the number of shocks in the computational study [2]. This validates that the shock pattern prediction by the analytical model is consistent with the one obtained in the computational study by Vijayakumar [2].

The station 2 conditions of the inlet are validated by comparing the static pressure p_2, Mach number M_2 and mass flow rate $\dot{m}_2$ obtained from the analytical model and from the corresponding computational study [2]. The Mach number comparison is made in Table 5-11.

Table 5-11 Validation of Station 2 Mach Number.

Case ID	CFD [2] M_2	Analytical prediction M_2	% $\lvert\Delta\epsilon\rvert$
CIV I	1.88	2.08	9.6
CIV II	2.88	3.04	5.5
CIV III	3.15	3.31	5.0

The static pressure at station 2 obtained from the analytical model is compared with the results from computational study [2] in Table 5-12. The mass flow rate at station 2 is also compared in Table 5-13. At station 2 we immediately expect the mass flow rate for on-design to be more than off-design but the counter-intuitive trend in the Table 5-13 is due to the difference in the free stream density as the off-design cases are evaluated at different altitudes and velocities. An accurate estimate of mass flow rate by the analytical model indicates that the fore shock structure and the corresponding captured mass flow rate are predicted correctly.

Table 5-12 Validation of Station 2 Static Pressure.

Case ID	CFD [2] p_2 [Pa]	Analytical prediction p_2 [Pa]	%$\lvert\Delta\epsilon\rvert$
CIV I	65098	61819	5.0
CIV II	34879	36457	4.5
CIV III	31788	32619	2.5

Table 5-13 Validation of Station 2 Mass Flow Rate.

Case ID	CFD[2] $\dot{m}_2$ [kg/m^3]	Analytical prediction $\dot{m}_2$ [kg/m^3]	%$\lvert\Delta\epsilon\rvert$
CIV I	31.85	32.79	2.9
CIV II	25.55	25.88	1.2
CIV III	23.55	24.37	3.5

From Table 5-11 to 5-13, the analytical model predicts the computational results [2] of static pressure, mass flow rate and Mach number at station 2 with an accuracy >90%. With the validation of the inlet model with experimental [9] and computational results [2], we can confidently perform simulations to predict SCRamjet inlet operation.

5.2 SCRamjet Isolator Model Validation

The isolator model presented in section 4.3 is validated using experimental and computational data [20, 3]. The three modes of steady isolator operation namely: shock-free mode, oblique shock train mode and normal shock train mode are validated in this section.

5.2.1 Shock Free Mode Validation

The computational results provided by Vijayakumar and Wilson [20, 2] are used for validating the shock free mode. The two-dimensional computational study of inlet-isolator carried out by Vijayakumar [2] simulated flight conditions with Mach number 3.5 to 6 along a constant dynamic pressure trajectory $q_0 = 47800\ N/m^2$. The isolator geometry considered by Vijayakumar was a constant area duct and its equivalent geometrical parameters for the analytical study are tabulated in Table 5-14. The average conditions at station 2 provided by Vijayakumar are used as upstream conditions for isolator in the analytical model and are tabulated in Table 5-15.

Table 5-14 Validation Case Geometrical Data [2].

Isolator geometrical parameter by Vijayakumar [2]	Equivalent analytical geometrical parameter	Design values SI units
Isolator width	d_Z	0.608 [m]
Isolator length	L_{ISO}	2.02 [m]
Isolator height	H_{ISO}	0.152[m]

Table 5-15 Validation Case Configuration Data [2].

Case ID	M_2	p_2[Pa]	T_2[K]	$p_{2.5}$[Pa]	Mode Type
CISV I	3.15	31788	646	(no blockage)	Shock free
CISV II	2.58	41887	596.5	(no blockage)	Shock free
CISV III	1.88	65098	551	(no blockage)	Shock free
CISV IV	1.35	100201	545	(no blockage)	Shock free

The static pressure, temperature and Mach number at station 2.5 are compared in Table 5-16, 5-17 and 5-18 respectively. The computational results [2] at station 2.5 (or 3

according to Vijayakumar [2]), are obtained from the inlet-isolator coupled analysis. Therefore the coefficient of friction and other boundary layer parameters at station 2 in the analytical model are evaluated using an equivalent flat plate with average length of the inlet wetted surfaces.

Table 5-16 Validation of Station 2.5 Static Pressure.

Case ID	CFD [2] $p_{2.5}$ [Pa]	Analytical prediction $p_{2.5}$ [Pa]	%$\lvert\Delta\epsilon\rvert$
CISV I	36495	35869	1.71
CISV II	47112	46709	0.86
CISV III	70894	72075	1.67
CISV IV	110633	116122	4.96

Table 5-17 Validation of Station 2.5 Static Temperature.

Case ID	CFD [2] $T_{2.5}$ [K]	Analytical prediction $T_{2.5}$ [K]	%$\lvert\Delta\epsilon\rvert$
CISV I	716.9	709.2	1.07
CISV II	654.6	643.7	1.67
CISV III	587	583.0	0.61
CISV IV	582	576.5	0.95

Table 5-18 Validation of Station 2.5 Mach Number.

Case ID	CFD [2] $M_{2.5}$	Analytical prediction $M_{2.5}$	%$\lvert\Delta\epsilon\rvert$
CISV I	2.90	2.93	1.03
CISV II	2.37	2.41	0.71
CISV III	1.74	1.75	0.57
CISV IV	1.22	1.20	1.63

From Table 5-16 to 5-18, the analytical model predicts the computational results [2] of static pressure, temperature and Mach number at station 2.5 with an accuracy >90%. The cases CISV II to IV represent the inlet off-design mode, where flow inside the isolator is subjected to shock and expansion wave interactions. Although these complex interaction exist, their averaged flow parameters remains close to prediction by one-dimensional flow with friction. It can be seen that the analytical model slightly over-predicts the compression when compared to computation results [2].

5.2.2 Oblique Shock Train Mode Validation

The experimental work by C. M. Fischer at RWTH [3] is used for validating the oblique shock train model. The experimental setup consisted of a flat plate followed by an isolator (Figure 5-8). The angle of attack (AoA) of the plate-isolator system was varied by Fischer [3] to obtain different entrance Mach numbers for the isolator. The experimental work by Fischer at RWTH [3] used of TH2 facility [3] to generate supersonic helium free-stream flow. The walls (wetted surface) were heated to about 800-1000 Kelvin using electrical heaters to preserve (T_w/T_e) similarity. A wedge at the back of the isolator (Figure 5-8) mimics the combustion blockages which operates the isolator in different modes for the same entrance Mach number.

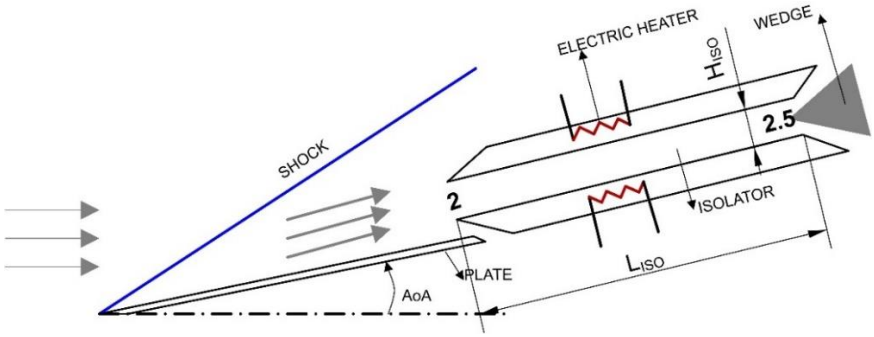

Figure 5-8: Schematic of experimental setup for heated isolator carried out by Fischer at RWTH [3] with helium as free stream.

The geometrical design parameters considered by Fischer [3] and its equivalent parameters in the analytical model are detailed in Table 5-19. Although the actual length of the isolator design by Fischer [3] was 0.2067[m], the measurements of back pressure and Mach number were carried out at 0.18[m] from station 2. Therefore the length of the isolator used in the analytical study is 0.18 [m]. The validation case data is tabulated in Table 5-20. The experiments carried out by Fischer [3] make use of pure helium as free

stream, therefore, the analytical model uses corresponding NASA polynomials [10] for helium to compute both thermodynamic and transport data.

Table 5-19 Isolator Geometrical Parameters of C. M. Fischer [3].

Isolator geometrical parameter by C. M. Fischer [3]	Equivalent analytical geometrical parameter	Design values SI units
Isolator width	d_Z	0.1 [m]
Isolator length	L_{ISO}	0.18[m]
Isolator height	H_{ISO}	0.018 [m]

Table 5-20 Validation Case Configuration Data Experimentally Measured by Fischer [3].

CASE ID	M_2	$p_2\ [pa]$	$T_2[K]$	$p_{2.5}[pa]$ (extracted)	Mode Type	T_w[K]
EISV I	3.5	12440±7.1%	333	~40921	Oblique shock train	1000
EISV II	3.5	12440±7.1%	333	~30643	Oblique shock train	1000
EISV III	3.5	12440±7.1%	333	~27894	Oblique shock train	1000
EISV IV	3.0	16320±7.1%	411	~57393	Oblique shock train	800

From Table 5-20, the cases EISV I to V are simulated in the analytical model by imposing back pressure detailed in Fischer's experimental work [3]. At first the experimentally measured Mach numbers [3] at station 2.5 are compared with the ones obtained from analytical model in Table 5-21.

Table 5-21 Validation of Station 2.5 Mach Number.

CASE ID	Experimental Fischer [3] $M_{2.5}$	Analytical model $M_{2.5}$	$\lvert\Delta\epsilon\rvert$%
EISV I	2.1	1.88	10.5
EISV II	2.3	2.23	6.2
EISV III	2.4	2.40	4.3
EISV IV	1.7	2.48	3.3

From Table 5-21, it can be observed that the analytical model predicts the experimental [3] Mach number at station 2.5 with an accuracy ≥90%. As the static pressure at station 2.5 is imposed from the experimental data and the corresponding Mach number being predicted by the analytical model accurately, it can be concluded that the total pressure losses are

predicted closely to the experimental observations [3]. The accuracy with which the Mach number and total pressure losses are predicted can be attributed to the extent to which the physical flow characteristics are preserved by the analytical model. The flow characteristics mainly depend on the length of the shock train and the number of shock reflections inside the shock train. If these two characteristics are predicted, then the Mach number and other static quantities can be evaluated accurately. To quantify the characterization, consider the variation in coefficient of pressure (CP) along the isolator defined by:

$$CP = \frac{p - p_0}{\frac{1}{2} p_0 \gamma_0 M_0^2}$$

where the free stream helium conditions for the plate are given by $p_0 = 460$[Pa], $r_0 = 1.667$ and $M_0 = 7.5$. The analytical model splits the oblique shock train into three parts namely; one-dimensional flow with friction, wedge shock reflections and constant area passage. The coefficients of pressure (CP) of these three parts are compared with wall pressure coefficient obtained from experimental work by Fischer [3] in Figure 5-9 for cases EISV I to IV. Note that the coefficient of pressure obtained from the analytical model is an assembly of CP obtained from one-dimensional flow with friction and wedge surface pressure which are strictly not the wall pressure coefficient provided in experimental results [3]. Therefore the importance of the comparison made in Figure 5-9 is to obtain an insight into the extent with which the analytical model characterizes real physical phenomena.

From Figure 5-9 (a) to (d), it can be seen that the trends of pressure variation predicted by the analytical model are close to the wall pressure variation measured by Fischer. Also, it is obvious to see that the analytical pressure coefficient at $x = 0.18$[m] (or station 2.5) exactly coincides with the experimental data [3] as the pressure obtained from the experimental data at station 2.5 was imposed as a boundary condition to the analytical model.

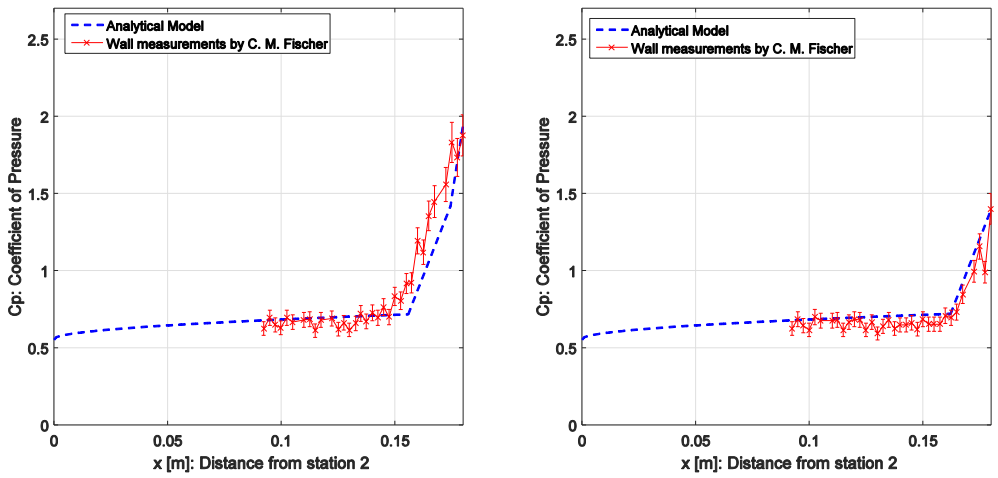

(a) (b)

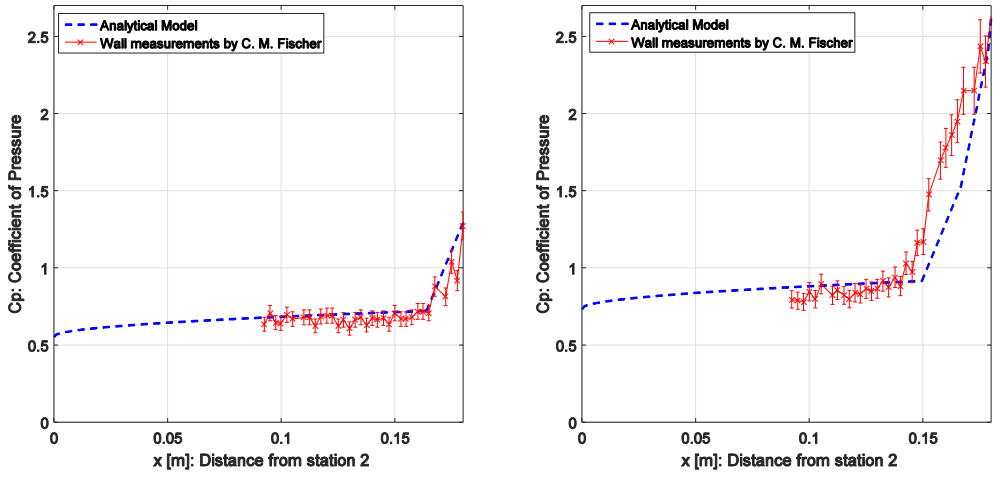

(c) (d)

Figure 5-9: Comparison of pressure coefficient (CP) obtained from analytical model and wall pressure coefficient from experimental work by C.M. Fischer for case (a) EISV I, (b) EISV II (c) EISV III and (d) EISV IV.

The analytical flow characterization for cases EISV I to IV are plotted using MATLAB in Figures 5-10 to 5-13 respectively and can be compared with Schileren shadowgraphs provided by C. M. Fischer's experimental work [3] to draw additional conclusions.

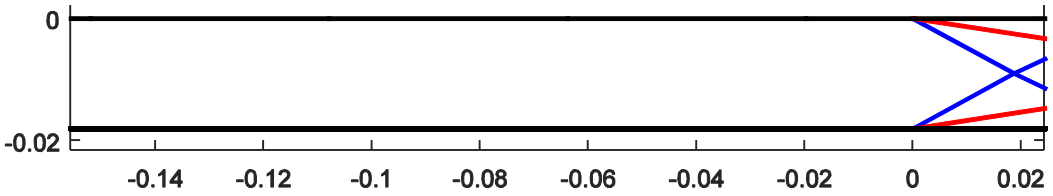

Figure 5-10: Analytical flow characterization of oblique shock train mode EISV I case.

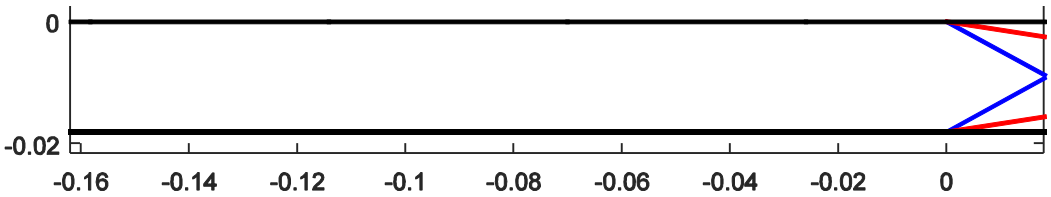

Figure 5-11: Analytical flow characterization of oblique shock train mode EISV II case.

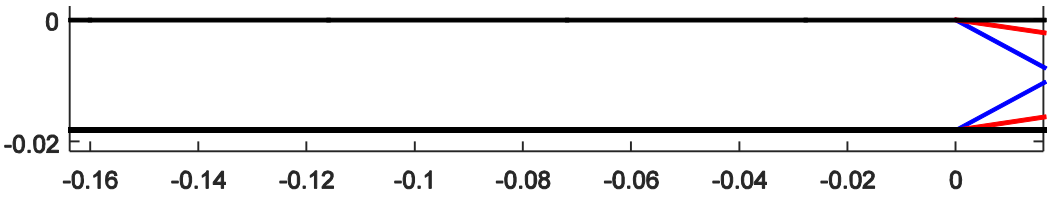

Figure 5-12: Analytical flow characterization of oblique shock train mode EISV II case.

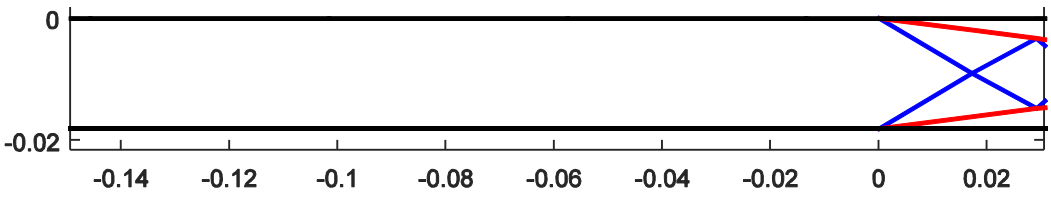

Figure 5-13: Analytical flow characterization of oblique shock train mode EISV III case.

5.2.3 Normal Shock Train Mode Validation

The computational LES (Large Eddy Simulation) work by Morgan at Stanford [33] of normal shock train study is used for validation. The LES computational work by Morgan [33] was based on experimental LDV (Laser Doppler Velocimetry) work by Carroll [34]. Therefore the results of the analytical model are compared with both computational and corresponding experimental work [33, 34]. At first consider the geometrical design parameters considered by Morgan [33] and Carroll [34]. Their equivalent geometrical parameters for the analytical study are detailed in Table 5-22. The validation case data is tabulated in Table 5-23.

Table 5-22 Isolator Geometrical Parameters of Morgan [33].

Isolator geometrical parameter by Morgan [33]	Equivalent analytical geometrical parameter	Design values SI units
Isolator width	d_Z	0.0762 [m]
Isolator length	L_{ISO}	0.75 [m]
Isolator height	H_{ISO}	0.03375[m]

Table 5-23 Validation Case Configuration Data.

CASE ID	$M_{2.2}$	$p_{t_{2.2}}$[pa]	$\frac{Re}{L}$[1/m]	$M_{2.5}$	Mode Type
ENSTV I	1.6	206153±690	30×10^6	~0.99	Normal shock train mode

The experimental work by Carroll [34] and computational work by Morgan [33] provided the Mach number upstream of the normal shock at station 2.2. Therefore in the analytical study we neglect the one-dimensional flow with friction part and only use the shock-nozzle model to obtain the normal shock train results. The boundary layer thickness at station 2.2 was provided by Carroll [34] from which the momentum thickness was computed to calculate the shock train length. The static temperature of the free stream was calculated using Reynolds number and state relationship and found to be approximately 195K.

The Mach number variation along the supersonic core obtained from computational work by Morgan [33] and the corresponding experimental work by Carroll [34] is compared with the analytical model predictions. The data obtained from computational and experimental work [33, 34] clearly provides crisp variation of Mach number through first six shocks and then smudges away becoming asymptotic to M~0.99. Therefore in Figure 5-14, the Mach numbers through first six shock-nozzle pairs are compared with computational [33] and experimental work [34]. As the inter-shock distance is unknown in the analytical model, the location of peak Mach numbers obtained from the analytical model are overlapped on the computational [33] and experimental [34] data.

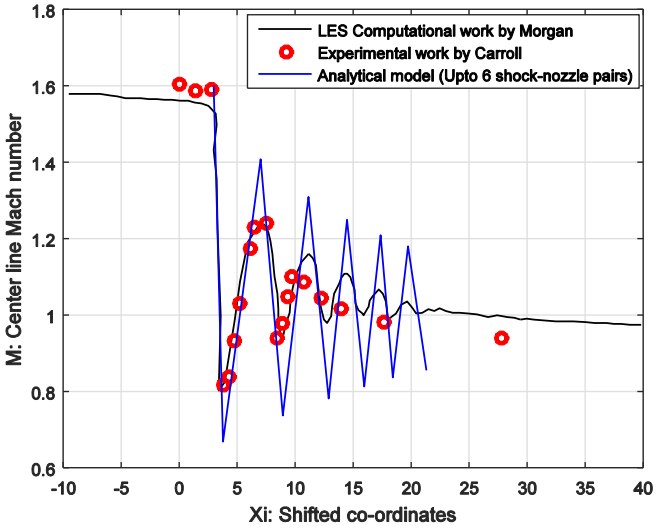

Figure 5-14: Validation of centerline Mach number through normal shock train for case ENSTV I.

The x-axis along which the plot is made in Figure 5-14 is defined similar to the one defined in the computational work [33] and given by $Xi = (x - x_2)/\delta$, where the x represents the distance from station 2, x_2 represents the co-ordinate shift and δ is the

boundary layer thickness at station 2.2 used for normalization. The values of x_2 and δ are detailed in the computational work by Morgan [33].

The total pressure losses through the supersonic core inside the normal shock train can be studied using the variation of p_t/p with Xi. The comparison of p_t/p along Xi obtained from analytical model (for first six shock-nozzle pairs) and computational work by Morgan [33] is made in Figure 6-15.

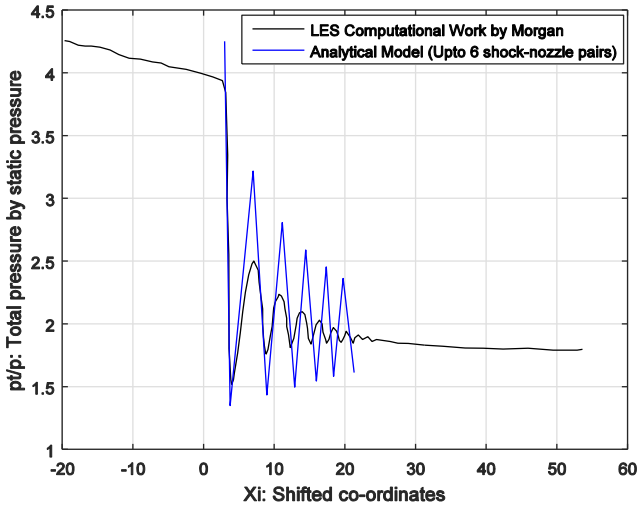

Figure 5-15: Validation of total to static pressure ratio through normal shock train for case ENSTV I.

From Figure 5-14 and 5-15, it can be seen that the analytical model predicts the trends of Mach number and total pressure losses correctly. Also, it can be seen that the peaks of Mach number are over predicted by the analytical model. This is because the supersonic core area in real physical flow keeps decreasing (Figure 4-16) while the analytical model assumes the core area at shock-nozzle exit is the same as duct area.

To make final conclusion on the normal shock train model, consider the asymptotic behavior of shock-nozzle model in Figure 5-16; this can be compared with the asymptotic data obtained from computational and experimental work [33, 34] in Figure 5-14. It can be

seen from Figure 5-16(a) and 5-14, that the Mach numbers from analytical model, experimental work by Carroll [34] and computational work by Morgan [33] asymptotically reach M~1. This signifies that the analytical model is consistent with the observations made in experimental and computational work [33, 34].

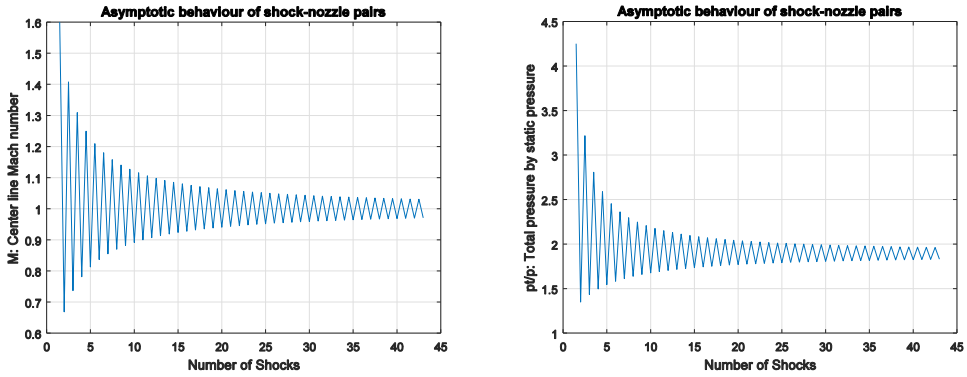

(a) (b)

Figure 5-16: Asymptotic behavior of (a) Mach number and (b) total to static pressure ratio inside normal shock train from analytical model for case ENSTV I.

Similar to the asymptotic comparison of Mach number inside the normal shock train, the total to static pressure ratio can be compared. From Figure 5-16(b) and 6-15, it can be seen that the ratio of total to static pressure obtained from analytical model and computational work by Morgan [33] asymptotically reach p_t/p~1.8.

In a ramjet operating mode, if the analysis is carried out using method detailed by Heiser and Pratt [25], the entrance Mach number of the burner is imposed by the thermal throat location and fueling condition. When an entrance Mach number at station 2.5 is imposed, the closest post shock subsonic Mach number from the asymptotic behavior (Figure 5-16(a)) is selected, thereby fixing unique number of normal shocks required in the shock train. This will provide all the corresponding flow variables (p,T) for the burner analysis.

5.3 Burner Validation

The SCRamjet burner model presented in section 4.5 along with the injector model in section 4.4 is validated in this section using experimental ground test [22] and flight test data [7]. At first the thermochemistry model presented in section 3.3.1 is validated with corresponding NASA CEA [34] tool. The mole fractions of nine species considered in section 3.3.1 for hydrogen-air equilibrium chemistry analysis using MATLAB are compared with NASA CEA [34] results. The equilibrium composition at $(\phi = 0.99, T = 2500\ K, p = 10KPa)$ and $(\phi = 0.49, T = 1800\ K, p = 1KPa)$ are validated Table 5-24 and 5-25 respectively.

Table 5-24 Validation of Equilibrium Mole Fraction at $\phi = 0.99, T = 2500\ K, p = 10KPa$.

Species	Moles fraction Equilibrium model	Mole fraction CEA-NASA	$\lvert\Delta\epsilon\rvert$%
H2	0.041535	0.041571	0.0035
N2	0.624010	0.623620	0.0390
O2	0.015117	0.014751	0.0366
H2O	0.269800	0.268860	0.0939
OH	0.021935	0.023968	0.2033
H	0.016325	0.016238	0.0087
O	0.005666	0.005562	0.0104
N	10^{-7}	$<10^{-5}$	~0
NO	0.005421	0.005611	0.019

Table 5-25 Validation of Equilibrium Mole Fraction at $(\phi = 0.49, T = 1800\ K, p = 1KPa)$.

Species	Moles fraction Equilibrium model	Mole fraction CEA-NASA	$\lvert\Delta\epsilon\rvert$%
H2	0.0003297	0.0003264	0.0003
N2	0.7136163	0.7130300	0.0586
O2	0.0941450	0.0934470	0.0698
H2O	0.1862350	0.1873200	0.1084
OH	0.0024426	0.0027986	0.0356
H	0.0000660	0.0000651	~0
O	0.0003762	0.0003718	0.0004
N	10^{-7}	$<10^{-5}$	~0
NO	0.0027888	0.0026374	0.0151

From Table 5-24 and 5-25, the absolute percentage error when normalized with sum of mole fractions (or 1) is found to be less than 1%. Therefore the realization of the equilibrium model in MATLAB [27] is accurate and can be confidently implemented into the burner model. Additionally to obtain a broader picture of the equilibrium model a temperature sweep at constant pressure is carried out to observe the trends in the equilibrium mass and mole fractions. This is done at $p = 1KPa$ and $\phi = 0.5$ with temperature varying from 900K to 5000K and corresponding variation of mass and mole fractions obtained from equilibrium model are plotted using MATLAB [27] in Figure 5-17 (a) and 5-17 (b) respectively. It is observed from Figure 5-17, the temperatures at which dissociation of nitrogen molecules (N_2) occur are consistent with plots made by Anderson [23] for pure air.

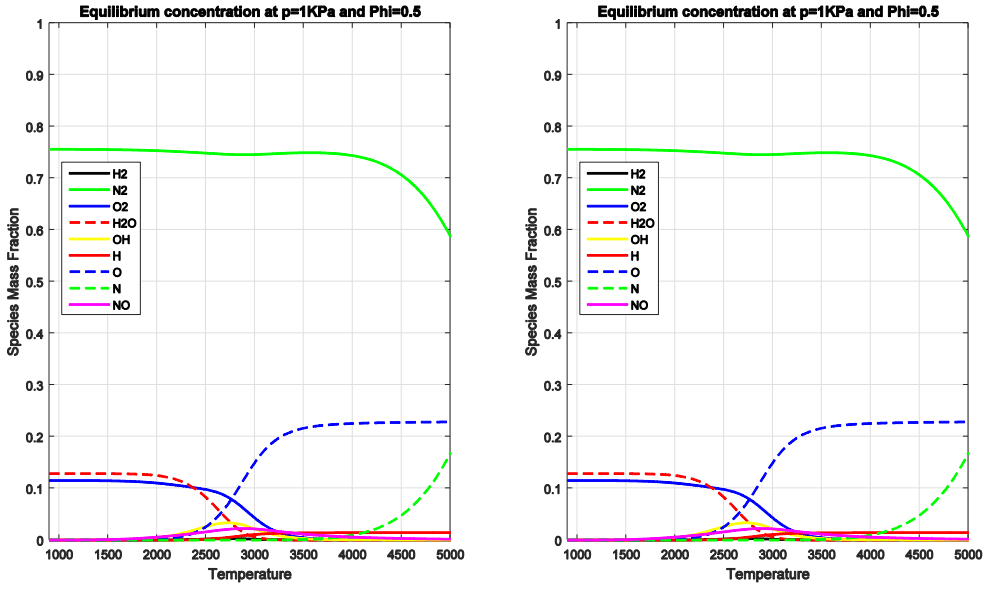

(a) (b)

Figure 5-17: (a) Species mass fraction (b) Species mass fraction.

The ODEs derived for the burner analysis in section 4.5.1.4 are validated by comparing static pressure variations along the burner obtained from ground test [22] and flight test [7] data. The first set of comparisons are made with the experimental ground test carried out at University of Queensland using free-piston shock tunnel by R. R. Boyce [22]. The diverging burner geometry which was ground tested by Boyce [22] is detailed in Figure 5-18 with its top and side view. Note that in Figure 5-18 all the dimensions are in meters.

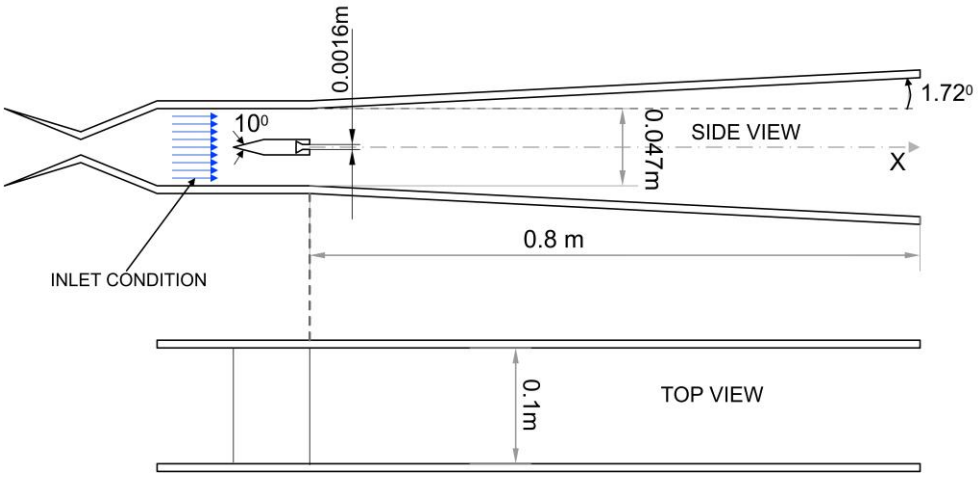

Figure 5-18: Burner geometry used for experimental ground test by Boyce [22].

The experiment by Boyce [22] was performed in a window of 5 milliseconds from which the average wall pressure distribution of the burner was obtained. The injector used by Boyce [22] was strut type with a slot width of 1.6mm. The injector inlet conditions (or station 2.5) used for validation are tabulated in Table 5-26. Note that the fuel was injected at sonic conditions by Boyce [22].

Table 5-26: Validation Case Data of Experimental Ground Test by Boyce [22].

CASE ID	$M_{2.5}$	$p_{2.5}\ [pa]$	$T_{2.5}[K]$	ϕ	T_w[K]	M_{jet}
EGBV I	2.47±6%	59000±9%	1025±13%	0.19	300	1
EGBV II	2.47±6%	59000±9%	1025±13%	0.38	300	1
EGBV III	2.47±6%	59000±9%	1025±13%	0.58	300	1

The velocity and the total conditions of the fuel injected was estimated from the information given in Table 5-26 assuming the pressure of the fuel during injection to be matched with pressure at station 3. An approximate drag coefficient of the strut was calculated from classical shock-expansion theory and was found to be $C_D = 0.05$. The analytical model of the injector and the burner are used to obtain its corresponding pressure distribution and are then compared with experimental data provided by Boyce [22]. Note that the hydrogen-strut mixing model presented in section 4.5.1.1 is used for analytical simulation. The comparison of pressure distribution and the corresponding Mach number and temperature distribution obtained from the analytical model for case EGBV I to III are plotted in Figure 5-19 to 5-21. The X-axis in these plots represent the distance from the injector exit (or station 3) in meters. The pressure and temperature are non-dimensionalized with respect to the injector inlet conditions (or station 2.5) tabulated in Table 5-26.

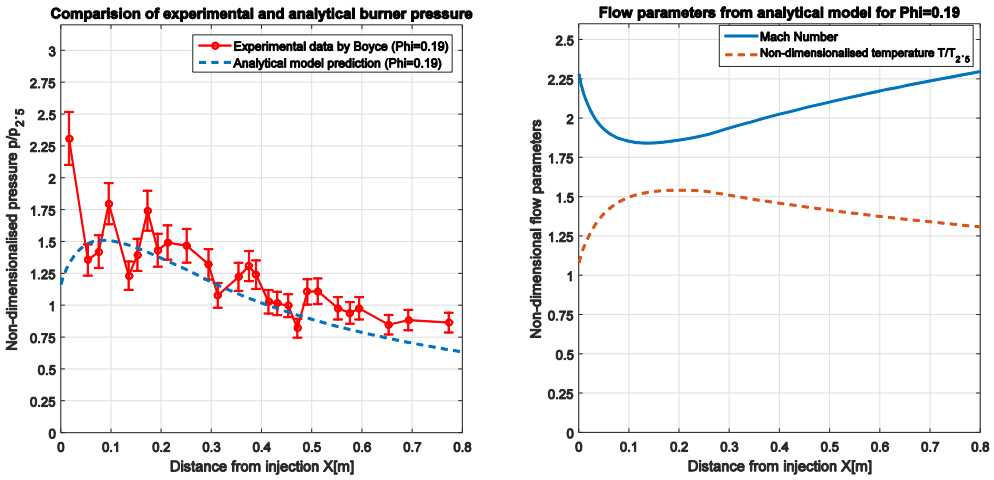

(a) (b)

Figure 5-19: Case EGBV I, (a) Comparison of pressure distribution, (b) Flow variable obtained from analytical model.

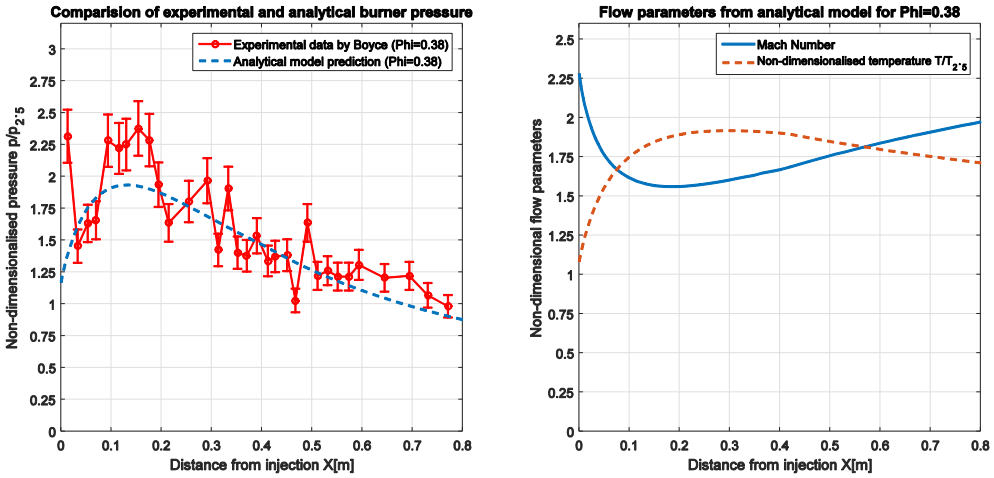

Figure 5-20: Case EGBV II, (a) Comparison of pressure distribution, (b) Flow variables obtained from analytical model.

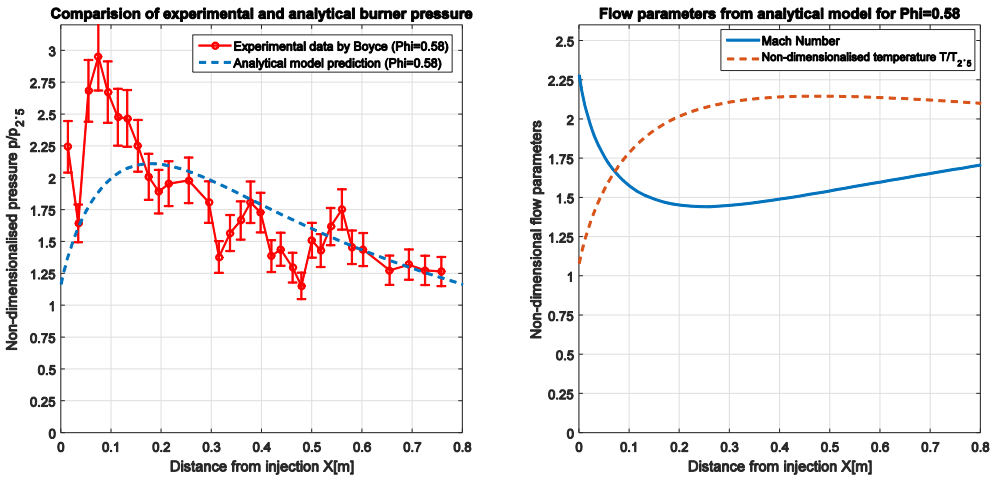

Figure 5-21: Case EGBV III, (a) Comparison of pressure distribution, (b) Flow variables obtained from analytical model.

The comparison of analytical and experimental [22] pressure profile from Figure 5-19(a) to 5-21(a) reveals that the analytical model predicts the mean pressure distribution with reasonable accuracy. Also, the initial wall pressure fluctuations in the experimental data [22] are mostly likely due to the shock-expansion waves created by the injector strut. At station 3 the pressure is slightly higher (with lower Mach number) when compared to the inlet conditions at station 2.5. This is due to the injector drag and jet area blockage effect. The Mach number and non-dimensionalized temperature obtained from analytical model are plotted in Figures 5-19(b) to 5-21(b). For $\phi = 0.58$ the minimum Mach number is least while maximum temperature is highest when compared to $\phi = 0.38$ and $\phi = 0.19$. These observations are consistent with Rayleigh flow in classical gas-dynamics [26].

To investigate the effect of mixing efficiency, the hydrogen-strut mixing model is replaced with parallel injection model presented in section 4.5.1.1 for case EGBV III and the corresponding pressure distribution and mixing efficiency profile obtained from the analytical model are compared in Figure 5-22.

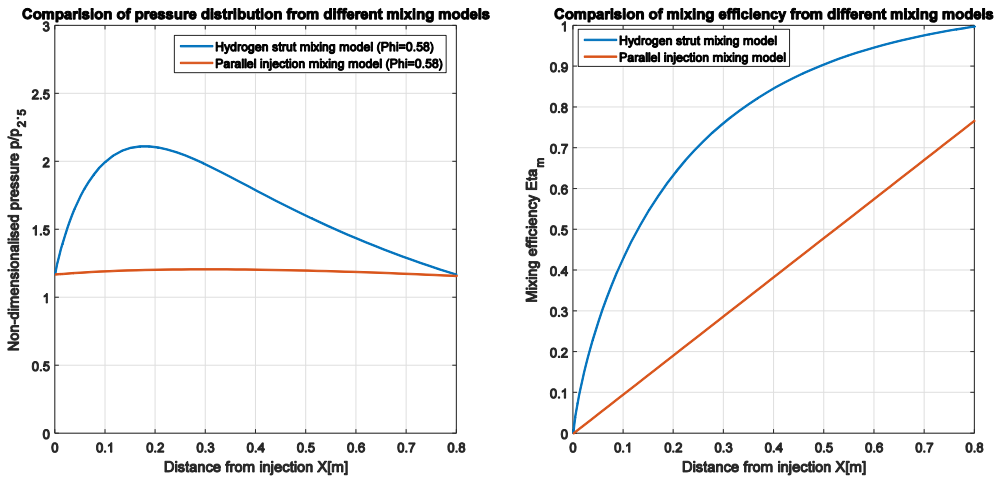

Figure 5-22: Case EGBV III, (a) Comparison of pressure distribution, (b) Comparison of mixing efficiency.

From Figure 5-22, it can clearly be seen that the burner pressure profile depends largely on the mixing efficiency distribution ($\eta_m(x)$). The linear mixing model for parallel injection largely deviated from hydrogen-strut mixing model prediction. Therefore it is important to note that the burner flow variables and its profiles can be predicted accurately only if the mixing efficiency is known.

The generalized models for mixing presented in section 4.5.1.1 possess a great significance if the pressure profile from the experiments are known as the fit parameters can be fine-tuned or calibrated to match the pressure profile obtained from the experiments. This becomes useful in estimating the flow variables which were not experimentally measured and/or are difficult to measure.

The next validation of the burner model is carried out using Hyshot-II flight test data provided by University of Queensland [7]. The SCRamjet schematic of Hyshot-II flight test [7] is shown in Figure 5-23. The Hyshot-II equivalent burner-nozzle geometrical parameters for the analytical study is detailed in Table 5-27.

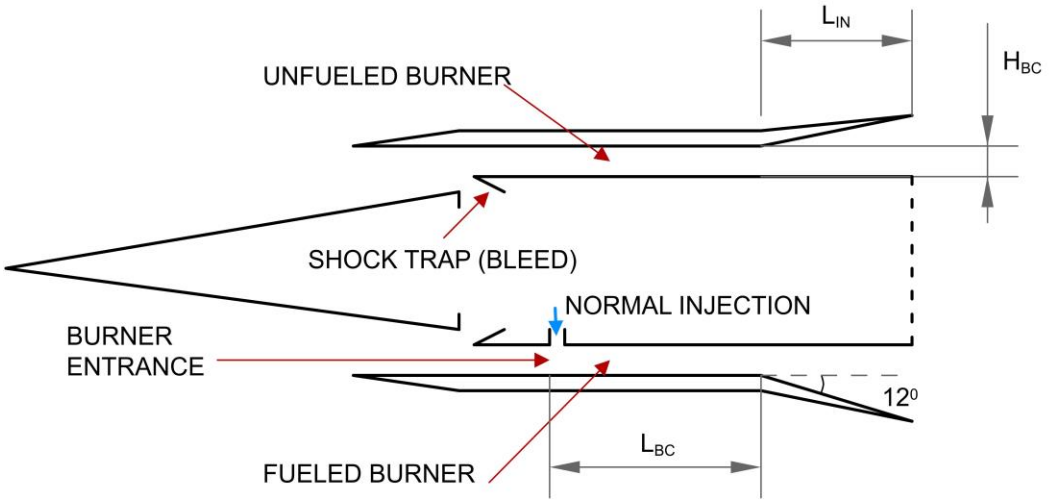

Figure 5-23: Schematic of Hyshot-II SCRamjet geometry.

Table 5-27 Geometrical Parameters of Hyshot-II Burner-Nozzle [7].

Equivalent analytical model parameter	Description of geometrical parameters	Design values/range SI units
L_{BC}	Length of constant area burner	0.242 [m]
L_{IN}	Length of internal nozzle	0.147 [m]
σ_{IN}	Constant wall angle of internal nozzle	12^0
H_{BC}	Height of constant area burner	0.0098[m]
d_Z	Engine depth	0.075[m]

The Hyshot-II [7] used gaseous hydrogen as fuel by normally injecting it at sonic conditions. The injector inlet conditions (or station 2.5) for fueled and unfueled case is detailed in Table 5-28. These conditions were estimated from experimental flight data using high fidelity computational analysis by Smart [7]. Also, the Prandtl number was estimated by Smart [7] as 0.9 assuming the flow is turbulent.

Table 5-28: Validation Case Data Estimated for Hyshot-II Flight Test [7].

CASE ID	$M_{2.5}$	$p_{2.5}\ [pa]$	$T_{2.5}[K]$	ϕ	T_w[K]	M_{jet}
EFTV I	2.393	44847	1416.6	0.346	350	1
EFTV II	2.436	55256	1388.4	0.000	350	1

In Table 5-28, the case EFTV I is the fueled case and EFTV II is the unfueled case. The one-dimensional pressure distribution obtained from analytical model for two cases in Table 5-28 are compared with flight test data of Hyshot-II [7]. Note that hydrogen normal mixing model presented in section 4.5.1.1 is used for analytical simulation. The comparison of the pressure distribution and corresponding Mach number and temperature distribution obtained from the analytical model for case EFTV I and II are plotted in Figure 5-24 and 5-25 respectively. The X-axis in these plots represent the distance from the injector exit (or station 3) in meters. The pressure and temperature are non-dimensionalized with respect to the injector inlet conditions (or station 2.5) tabulated in Table 5-28.

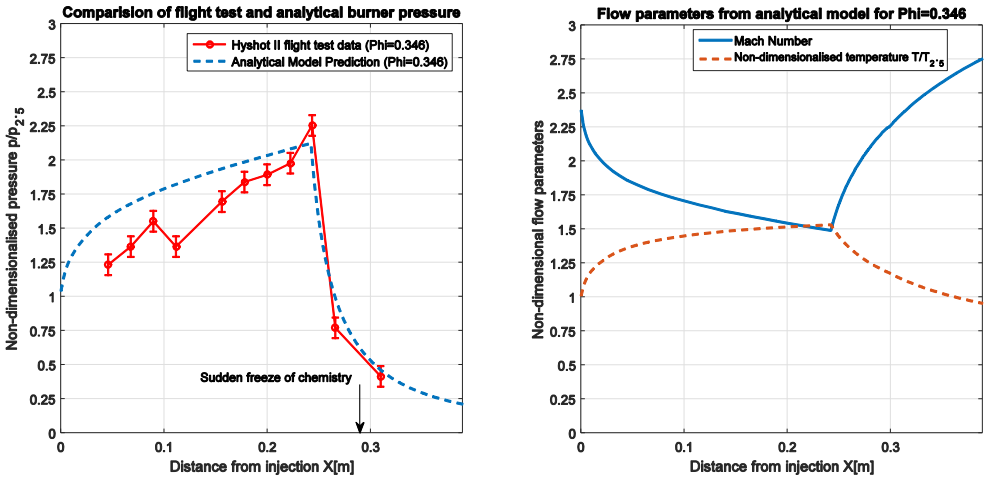

Figure 5-24: Case EFTV I, (a) Comparison of pressure distribution, (b) Flow variables obtained from analytical model.

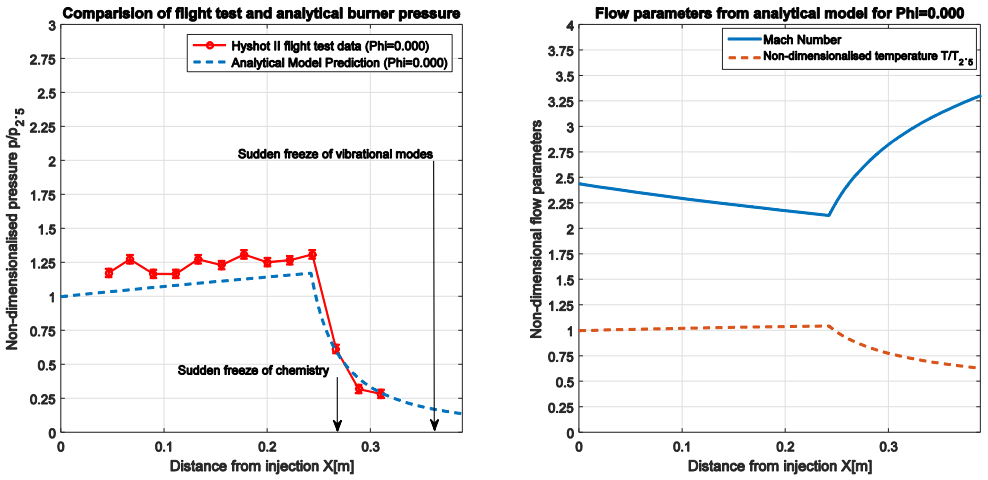

Figure 5-25: Case EFTV II, (a) Comparison of pressure distribution, (b) Flow variables obtained from analytical model.

Consider case EFTV I and its corresponding burner flow parameters plotted in Figure 5-24. From the pressure distribution plotted in Figure 5-24(a), it can be seen that the normal mixing efficiency model presented in section 4.5.1.1 characterizes the heat addition process accurately. The corresponding mixing efficiency for EFTV I case is plotted in Figure 5-26. The maximum pressure predicted by the analytical model is close to that of the flight data of Hyshot-II [7] in Figure 5-24(a). It was observed that the skin friction coefficient (c_f) determined from the procedure detailed in section 3.4 varied from 0.0037 to 0.003. The sudden freeze approximation inside nozzle to account for the non-equilibrium chemistry proposed in the analytical model was triggered at approximately at distance 0.29[m] from the injection (where $Da_{chem} = 1$). The Mach number and non-dimensionalized static temperature variation predicted by the analytical model are plotted in Figure 5-24(b).

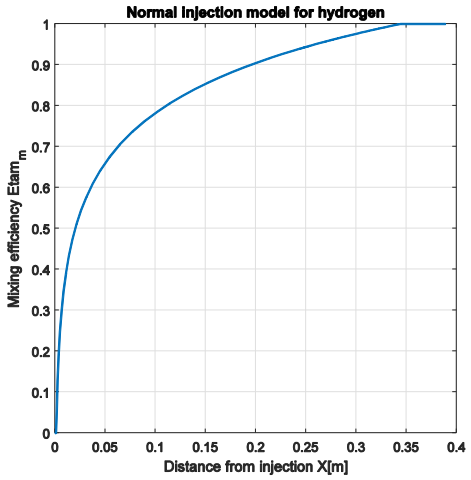

Figure 5-26: Case EFTV I mixing efficiency variation along the burner-nozzle.

Consider the case EFTV II and its corresponding burner flow parameters plotted in Figure 5-25. From the pressure distribution plotted in Figure 5-24(a), it can be seen that the skin friction effect is appropriately predicted in the constant area regime. Similar to case EFTV I, for the case EFTV II the skin friction coefficient varied between 0.0037 and 0.003

as predicted by procedure detailed in section 3.4. The sudden freeze approximation inside the nozzle to account for the non-equilibrium chemistry proposed in the analytical model was triggered approximately at a distance of 0.27[m] from injection. Also, the sudden freeze approximation for non-equilibrium thermodynamics ($Da_{therm} = 1$) was trigged approximately at a distance of 0.38 [m]. Note once the flow is chemically frozen, the flow is thermally perfect until it gets thermodynamically frozen from where it is calorically perfect.

To conclude the validation, it can be stated that the supersonic burner model proposed in section 4.5.1 were validated with ground test data [22] and flight test data [7] and provided accurate prediction of the pressure distribution through the burner. Thus making the burner model a credible tool to carry out fast parametric analysis.

Chapter 6

Conclusion

A brief summary of this document is presented in this chapter along with the future work that is intended to be carried out.

6.1 Summary

A reduced order analytical model for a dual model SCRamjet (DMSJ) engine is presented in Chapter 4 and validated in Chapter 5. The required theoretical background governing the physics of high speed gas flows is presented in Chapter 3. The analytical model of DMSJ was built on MATLAB [27] platform and it is split into five interactive components namely; inlet, isolator, injector, burner and nozzle.

The inlet compression process is modelled using thermally perfect oblique shockwaves. The compression process is split into external and internal compression where the shock reflections are automated using a proposed methodology detailed in section 4.2.2. The viscous corrections for the inlet are made by using the displacement thickness and modifying the inviscid boundary as presented in section 4.2.3. The inlet model was validated with experimental data provided by NASA [9] and computational work by Nandakumar [2] in section 5.1. It was observed that the analytical model predicted the flow properties with an average accuracy of 90%. Also, the inlet model slightly under predicted the pressure rise consistently and the probable reason was attributed to the nose bluntness effect which was ignored by the analytical model.

The SCRamjet isolator operating in one of the three modes namely: shock free-mode or oblique shock train mode or normal shock train mode is modelled using thermally perfect gas processes. The shock free mode is modelled using one-dimensional flow with friction. The oblique shock train mode is modelled using the wedge model presented in section 4.3.2 and the normal shock train mode using the shock-nozzle approach presented

in section 4.3.3. The c_f predicted using the reference temperature method is found to slightly over predict the effect of friction. The flow characterization of the oblique shock train mode and normal shock train mode by the analytical model is found to be accurate. The validation of the analytical model with respect to experimental work [3, 34] and computation work [2, 33] revealed an accuracy of >90% in the flow variables predicted.

The burner and nozzle model makes use of the generalized quasi one dimensional flow theory. The ODE's proposed for the burner in section 5.5 and 5.6 and are integrated using Runge-Kutta 4th order scheme and are validated with ground test [22] and flight test data [7]. The prediction of mean burner pressure distribution proved to be accurate. It was found that the burner flow distribution is highly dependent on the mixing efficiency profile.

The current work therefore introduces a new reduced order model for complete dual mode SCRamjet engine simulation using MATLAB [27]. This model's reliability in predicting the flow variables inside the SCRamjet engine is established by validating with experimental and computation results obtained from existing literatures.

6.2 Future Work

The future work will focus on improving the reduced order modelling of the SCRamjet and to carry out more validation to improve its reliability. Some of the future work scheduled is summarized here:

- Validation of SCRamjet isolator-burner interaction model.
- Validation of single expansion ramp model.
- Improving the inlet model to capture nose bluntness effect.
- Improving the inlet model to account for three-dimensional effects.
- Improving the nozzle model to account for three-dimensional effects.
- To add hydrocarbon fuel-air equilibrium model to the existing hydrogen-air equilibrium model for combustion process.

Appendix A

Thermally Perfect Oblique and Normal Shocks

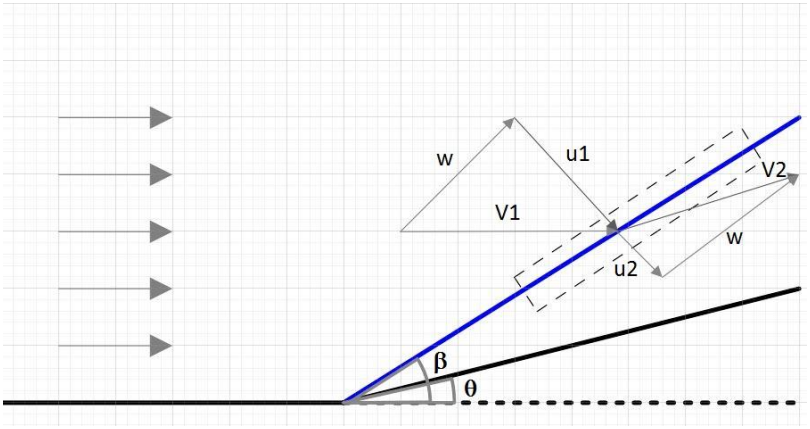

Figure 1

Trigonometric relations between parameters in control volume:

$$\tan(\beta) = \frac{u_1}{w} \tag{1}$$

$$\tan(\beta - \theta) = \frac{u_2}{w} \tag{2}$$

$$u_1 = V_1 \sin(\beta) \tag{3}$$

$$u_2 = V_2 \sin(\beta - \theta) \tag{4}$$

$$V_2 = V_1 \frac{\cos(\beta)}{\cos(\beta - \theta)} \tag{5}$$

Conservation Equations applied to control volume (Chemically Frozen)

$$\rho_1 u_1 = \rho_2 u_2 \tag{6}$$

$$p_1 + \rho_1 u_1^2 = p_2 + \rho_2 u_2^2 \tag{7}$$

$$h_{sens1} + \frac{V_1^2}{2} = h_{sens2} + \frac{V_2^2}{2} = h_{tot} \tag{8}$$

Thermodynamic Relations

$$\frac{p}{\rho} = R\,T \tag{9}$$

$$h_{sens} = \int_{T_{ref}}^{T} C_p dT \tag{10}$$

$$h_{tot} = h_{sens} + \frac{1}{2} V^2 \tag{11}$$

Combining mass conservation eq(6), state relation eq(9) and momentum eq(10) we have:

$$\frac{RT_1}{u_1} + u_1 = \frac{RT_2}{u_2} + u_2 \tag{12}$$

Recalling $u_1 = V_1 \sin(\beta)$ and if $\alpha = \frac{RT_1}{V_1 \sin(\beta)} + V_1 \sin(\beta)$ then,

$$\alpha\, u_2 - RT_2 - u_2^2 = 0 \tag{13}$$

Substituting for u_2 from eq(4) in eq(10) we have:

$$V_2^2 \sin^2(\beta - \theta) - \alpha V_2 \sin(\beta - \theta) + RT_2 = 0 \tag{14}$$

Consider energy equation by re arranging we have:

$$\frac{V_2^2}{2} = h_{tot} - \int_{T_{ref}}^{T_2} C_p dT \tag{15}$$

$$V_2 = \sqrt{2\left(h_{tot} - \int_{T_{ref}}^{T_2} C_p dT\right)} \tag{16}$$

By substituting V_2 from eq(16) in eq(5) we have:

$$\sqrt{2\left(h_{tot} - \int_{T_{ref}}^{T_2} C_p dT\right)} = V_1 \frac{\cos(\beta)}{\cos(\beta - \theta)} \tag{17}$$

Rearranging and squaring we have:

$$2\left(h_{tot} - \int_{T_{ref}}^{T_2} C_p dT\right)\cos^2(\beta - \theta) - V_1^2 \cos^2(\beta) = 0 \tag{18}$$

Also, by substituting V_2 from eq(5) in eq(14) we have

$$\left(V_1 \frac{\cos(\beta)}{\cos(\beta - \theta)}\right)^2 \sin^2(\beta - \theta) - \left(\frac{RT_1}{V_1 \sin(\beta)} + V_1 \sin(\beta)\right)\left(V_1 \frac{\cos(\beta)}{\cos(\beta - \theta)}\right)\sin(\beta - \theta) + RT_2 = 0 \tag{19}$$

Rearranging we have

$$\left(V_1 \frac{\cos(\beta)}{1}\right)^2 \tan^2(\beta - \theta) - \left(\frac{RT_1 + V_1^2 \sin^2(\beta)}{\tan(\beta)}\right)\tan(\beta - \theta) + RT_2 = 0 \tag{20}$$

Gas thermal heat capacity:

$$\frac{C_p}{R} = \sum_1^8 a(i)\, T^{i-2}$$

Air Data: (a(i) polynomial coefficients)

$R = 287.035$ J/Kg K

80<T<1000

–3.7319821E+00	5.4196701E–01	3.4693586E+00	3.8353798E–04
–2.7653130E–06	8.1886142E–09	–7.7368690E–12	2.4348723E–15

1000<T<6000

2.3769851E+05	–1.2440527E+03	5.1266690E+00	–2.0400644E–04
6.8321801E–08	–1.0553542E–11	6.6450071E–16	0.0000000E+00

Final Equation Set for Computation: (Oblique Shock Wave)

Considering equation (18) and (20) Unknown variables are β and T_2

$$2\left(h_{tot} - \int_{T_{ref}}^{T_2} C_p dT\right)\cos^2(\beta-\theta) - V_1^2\cos^2(\beta) = 0 \quad (21)$$

$$V_1^2\cos^2(\beta)\tan^2(\beta-\theta) - \left(\frac{RT_1 + V_1^2\sin^2(\beta)}{\tan(\beta)}\right)\tan(\beta-\theta) + RT_2 = 0 \quad (22)$$

Isolating T_2 from equation (22) we get and back substituting in equation (21) we have the required equation for oblique shockwaves:

$$\boldsymbol{2\left(h_{tot1} - \int_{T_{ref}}^{\sigma(\beta)} c_p dT\right)\cos^2(\beta-\theta) - V_1^2\cos^2(\beta) = 0}$$

Where, $T_2 = \sigma(\beta)$ and given by:

$$\sigma(\beta) = \left(\frac{RT_1 + V_1^2\sin^2(\beta)}{\tan(\beta)}\right)\tan(\beta-\theta) - V_1^2\cos^2(\beta)\tan^2(\beta-\theta)$$

Note: $h_{tot} = h_{tot1} = h_{tot2}$

Post processing:

$$V_2 = V_1\frac{\cos(\beta)}{\cos(\beta-\theta)}$$

$$\gamma_2 = \frac{c_{p2}}{c_{p2} - R}$$

$$a_2 = \gamma_2 RT_2$$

$$M_2 = \frac{V_2}{a_2}$$

$$\rho_2 = \rho_1\frac{\tan(\beta)}{\tan(\beta-\theta)}$$

Appendix B

Control Volume Viscous Correction

Conservation Equations applied to control volume (Chemically Frozen)

$$\rho_1 u_1 = \rho_2 u_2 = C_{mass} \tag{1}$$

$$p_1 + \rho_1 u_1^2 = p_2 + \rho_2 u_2^2 + \int_0^{L_i} \tau_w \, dA_w = C_{mom} \tag{2}$$

$$h_{sens1} + \frac{u_1^2}{2} = h_{sens2} + \frac{u_2^2}{2} = C_{energy} \tag{3}$$

Thermodynamic Relations

$$\frac{p}{\rho} = R\,T \tag{4}$$

$$h_{sens} = \int_{T_{ref}}^{T} C_p dT \tag{5}$$

$$h_{tot} = h_{sens} + \frac{1}{2}u^2 \tag{6}$$

Approximation of shear force integral in equation (2):

$$\int_0^{L_i} \tau_w \, dA_w = \frac{1}{2}\bar{\rho}\bar{u}^2 \bar{f} A_w L_i$$

where the average quantities are given by: $\bar{\rho} = \frac{1}{2}(\rho_1 + \rho_2)$ and $\bar{u} = \frac{1}{2}(u_1 + u_2)$. The two final equation with T_2 and u_2 as unknowns using equations (1, 2 and 3) are given by:

$$\boldsymbol{C_{mass}\left(\frac{RT_2}{u_2} + u_2\right) + \frac{A_w}{2}\left(\rho_1 + \frac{C_{mass}}{u_2}\right)(u_1 + u_2)^2 \bar{f} L_i - C_{mom} = 0}$$

$$\boldsymbol{\int_{T_{ref}}^{T_2} C_p dT + \frac{u_2^2}{2} - C_{energy} = 0}$$

Appendix C

One Dimensional Supersonic Combustion

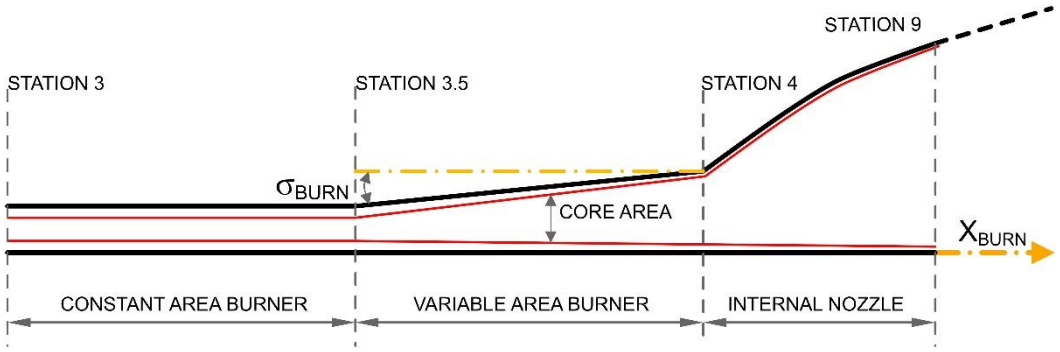

Figure 1.

Symbols:

A	Area $[m^2]$
H	Duct Height $[m]$
d	Engine Depth $[m]$
x	Axial Position $[m]$
p	Pressure $[Pa]$
T	Temperature $[K]$
h	Specific Enthalpy $[J/Kg]$
h_{sens}	Sensible Specific Enthalpy $[J/Kg]$
$\Delta_f^0 h$	Specific Formation Enthalpy $[J/Kg]$
e	Specific Internal Energy $[J/Kg]$
e_{sens}	Sensible Specific Internal Energy $[J/Kg]$
η_m	Mixing efficiency
ρ	Density $[Kg/m^3]$
Y_k	Species Mass Fraction
c_p	Specific Heat at Constant Pressure $[J/Kg\ K]$
c_v	Specific Heat at Constant Volume $[J/Kg\ K]$
f	Fuel to Air Ratio by Mass
$\mathcal{M}$	Molecular mass
ϕ	Equivalence Ratio
f	Fuel to air ratio by mass
F_{bx}	Body force per unit mass $[N/kg]$
D_{Hb}	Burner Hydraulic Diameter $[m]$
C_w	Burner Wall Perimeter [m]
C_j	Fuel Jet Perimeter

FLOW THERMODYNAMICS

Enthalpy:

$$h = \sum_{k=1}^{N} Y_k h_k$$

Where the species enthalpy h_k is given by the following equations:

$$h_k = h_{sens\,k} + \Delta_f^0 h_k$$

$$h_{sens\ k} = \int_{Tref}^{T} c_{pk} dT$$

Internal Energy:

$$e = \sum_{k=1}^{N} Y_k e_k$$

Where the species internal energy e_k is given by the following equations:

$$e_k = e_{sens\ k} + \Delta_f^0 h_k$$

$$e_{sens\ k} = \int_{Tref}^{T} c_{vk} dT$$

Heat Capacity:

$$c_p = \left(\frac{\partial h}{\partial T}\right)_{p,\phi} = \sum c_{pk} Y_k + \sum h_k \left(\frac{\partial Y_k}{\partial T}\right)_{p,\phi}$$

$$c_v = \left(\frac{\partial e}{\partial T}\right)_{v,\phi} = \left(\frac{\partial e}{\partial T}\right)_{\rho,\phi} = \sum c_{vk} Y_k + \sum e_k \left(\frac{\partial Y_k}{\partial T}\right)_{v,\phi}$$

Note: Meyer's relation is valid for individual species and not the mixture, Therefore we have

$$c_{pk} - c_{vk} = \frac{\mathcal{R}}{\mathcal{M}_k}$$

The species specific heat capacity at constant pressure (c_{pk}) can be obtained from NASA polynomials. With the molecular mass of the species known, species the species specific heat capacity at constant volume (c_{vk}) can be evaluated.

Equivalence Ratio:

$$\phi = \frac{\left(\frac{F}{A}\right)}{\left(\frac{F}{A}\right)_{stoic}} = \frac{f}{f_{st}} \eta_m$$

Differentiating we get:

$$\frac{d\phi}{dx} = \frac{f}{f_{st}} \frac{d\eta_m}{dx} \tag{23}$$

Molecular Mass:

$$\boldsymbol{\mathcal{M}} = \frac{1}{\sum \frac{Y_k}{\mathcal{M}_k}}$$

Differentiating we get:

$$\frac{d\boldsymbol{\mathcal{M}}}{dx} = -\boldsymbol{\mathcal{M}}^2 \sum \frac{1}{\mathcal{M}_k} \frac{dY_k}{dx} \tag{24}$$

DEVELOPMENT OF QUASI ONE DIMENSIONAL FLOW EQUATIONS TO RUNGE KUTTA 4th ORDER FORM

Conservation equations derived from integral form for typical scramjet combustion process is detailed here:

Mass Conservation:

$$\frac{1}{\rho}\frac{d\rho}{dx}+\frac{1}{u}\frac{du}{dx}+\frac{1}{A}\frac{dA}{dx}=\frac{1}{\dot{m}}\frac{d\dot{m}}{dx} \tag{25}$$

Momentum Conservation:

$$\frac{dp}{dx}=-\frac{\dot{m}}{A}\frac{du}{dx}-\frac{(u-u_{fx})}{A}\frac{d\dot{m}}{dx}-\frac{1}{2}\rho u^2 c_f\left(\frac{C_w}{A}\right)+\rho F_{bx} \tag{26}$$

Energy Conservation:

$$\frac{dh}{dx}=-u\frac{du}{dx}-\left(h+\frac{u^2}{2}-e_{tf}\right)\frac{1}{\dot{m}}\frac{d\dot{m}}{dx}+\frac{\dot{q}_{nf}C_w}{\dot{m}}+F_{bx}+\frac{\dot{q}_v}{u} \tag{27}$$

State Relationship:

$$\frac{1}{p}\frac{dp}{dx}=\frac{1}{\rho}\frac{d\rho}{dx}+\frac{1}{T}\frac{dT}{dx}-\frac{1}{\mathcal{M}}\frac{d\mathcal{M}}{dx} \tag{28}$$

Additional Definitions:

Fuel to air ratio by mass

$$f=\frac{\dot{m}_f}{\dot{m}_a}$$

Mass flow and its derivative

$$\frac{1}{\dot{m}}\frac{d\dot{m}}{dx}=\frac{\dot{m}_f}{\dot{m}}\frac{d\eta_m}{dx}=\frac{f}{1+f\eta_m}\frac{d\eta_m}{dx}$$

Mixing efficiency relation

$$\dot{m}_{fm}=\dot{m}_f\eta_m$$

Friction term

$$\frac{1}{2}\rho u^2 c_f\left(\frac{C_w}{A}\right)=\frac{1}{2}\rho u^2\left(\frac{4c_f}{D_{Hb}}\right)$$

Fuel jet velocity

$$u_f=\sqrt{u_{fx}^2+u_{fy}^2}$$

Total internal energy of fuel injected:

$$e_{tf}=h_{fsens}+\Delta_f^0 h_f+\frac{u_f^2}{2}-\frac{p}{\rho_f}$$

Wall heat transfer term:

$$\frac{\dot{q}_{nf}C_w}{\dot{m}}=-\frac{c_f R_f(h_{aw}-h_w)C_w}{2A}$$

$$h_{aw}=h+r\frac{u^2}{2}$$

$$c_f = \begin{cases} \dfrac{0.664}{(Re_x^*)^{0.5}}, & Re_x < Re_T\ (Laminar) \\ \dfrac{0.0592}{(Re_x^*)^{0.2}}, & Re_x \geq Re_T\ (Turbulent) \end{cases}$$

$$R_f = \begin{cases} Pr^{-\frac{2}{3}}, & Re_x < Re_T\ (Laminar) \\ Pr^{-\frac{1}{3}}, & Re_x \geq Re_T\ (Turbulent) \end{cases}$$

$$r = \begin{cases} Pr^{1/2}, & Re_x < Re_T\ (Laminar) \\ Pr^{1/3}, & Re_x \geq Re_T\ (Turbulent) \end{cases}$$

Note that for air $Pr = 0.71$ with 3% error in the range $300 < T < 2000$

Compact Form of Conservation Equations

The derivation of compact form starts with definition of two variables. The variable I_m is a collection of independent terms in the RHS of momentum conservation equation (4) and the variable I_e is a collection of independent terms in the RHS of energy equation (5). Note that appropriate relations in section **Additional Definitions** are made use to define I_m and I_e.

$$I_m = -\frac{(u - u_{fx})}{A}\frac{d\dot{m}}{dx} - \frac{1}{2}\rho u^2\left(\frac{4c_f}{D_{Hb}}\right) + \rho F_{bx} \tag{7}$$

$$I_e = -\left(h + \frac{u^2}{2} - e_{tf}\right)\frac{1}{\dot{m}}\frac{d\dot{m}}{dx} - \frac{2c_f R_f(h_{aw} - h_w)}{D_{Hb}} + F_{bx} + \frac{\dot{q}_v}{u} \tag{8}$$

Using equation (3) to (8) we can now define the conservation equation in their compact form:
Mass conservation

$$\frac{1}{\rho}\frac{d\rho}{dx} + \frac{1}{u}\frac{du}{dx} + \frac{1}{A}\frac{dA}{dx} = \frac{\dot{m}_f}{\dot{m}}\frac{d\eta_m}{dx} \tag{9}$$

Momentum conservation

$$\frac{dp}{dx} = -\frac{\dot{m}}{A}\frac{du}{dx} + I_m \tag{10}$$

Energy conservation

$$\frac{dh}{dx} = -u\frac{du}{dx} + I_e \tag{11}$$

State relationship

$$\frac{1}{p}\frac{dp}{dx} = \frac{1}{\rho}\frac{d\rho}{dx} + \frac{1}{T}\frac{dT}{dx} - \frac{1}{\mathcal{M}}\frac{d\mathcal{M}}{dx} \tag{12}$$

Derivative of Temperature: (An alternate Energy Equation)

The chemical equilibrium solver uses p, T, ϕ to find the composition and compute the mixture thermodynamic properties. Therefore it is required to bring in the temperature in the governing flow equations. So, consider the energy equation:

$$\frac{dh}{dx} = -u\frac{du}{dx} + I_e$$

Now $h = h(p, T, \phi)$ therefore we have:

$$\frac{dh}{dx} = \left(\frac{\partial h}{\partial p}\right)_{T\,\phi} \frac{dp}{dx} + \left(\frac{\partial h}{\partial T}\right)_{p\,\phi} \frac{dT}{dx} + \left(\frac{\partial h}{\partial \phi}\right)_{p\,T} \frac{d\phi}{dx}$$

Isolating for $\frac{dT}{dx}$ and substituting $c_p = \left(\frac{\partial h}{\partial T}\right)_{p\,\phi}$ we get:

$$\frac{dT}{dx} = \frac{1}{c_p}\left(\frac{dh}{dx} - \left(\frac{\partial h}{\partial p}\right)_{T\,\phi} \frac{dp}{dx} - \left(\frac{\partial h}{\partial \phi}\right)_{p\,T} \frac{d\phi}{dx}\right)$$

Using Eq (11) and Eq (10) and substituting for $\frac{dh}{dx}$ and $\frac{dp}{dx}$ in terms of $\frac{du}{dx}$ respectively we have:

$$\frac{dT}{dx} = \frac{1}{c_p}\left(\left(-u\frac{du}{dx} + I_e\right) - \left(\frac{\partial h}{\partial p}\right)_{T\,\phi}\left(-\frac{\dot{m}}{A}\frac{du}{dx} + I_m\right) - \left(\frac{\partial h}{\partial \phi}\right)_{p\,T} \frac{d\phi}{dx}\right) \tag{13}$$

Regrouping the terms we have:

$$\frac{dT}{dx} = \frac{1}{c_p}\left(\left(\left(\frac{\partial h}{\partial p}\right)_{T\,\phi} \frac{\dot{m}}{A} - u\right)\frac{du}{dx} - \left(\frac{\partial h}{\partial p}\right)_{T\,\phi} I_m - \left(\frac{\partial h}{\partial \phi}\right)_{p\,T} \frac{d\phi}{dx} + I_e\right) \tag{14}$$

Derivative of Molecular Mass

Recall Eq (2) we have:

$$\frac{d\mathcal{M}}{dx} = -\mathcal{M}^2 \sum \frac{1}{\mathcal{M}_k}\frac{dY_k}{dx}$$

Now the species mass fraction $Y_k = Y_k(p, T, \phi)$. Therefore its derivative is given by:

$$\frac{dY_k}{dx} = \left(\frac{\partial Y_k}{\partial p}\right)_{T\,\phi} \frac{dp}{dx} + \left(\frac{\partial Y_k}{\partial T}\right)_{p\,\phi} \frac{dT}{dx} + \left(\frac{\partial Y_k}{\partial \phi}\right)_{p\,T} \frac{d\phi}{dx} \tag{15}$$

Substituting for $\frac{dT}{dx}$ and $\frac{dp}{dx}$ from Eq (14) and Eq (10) in Eq (15) respectively we get:

$$\begin{aligned}\frac{dY_k}{dx} = {} & \left(\frac{\partial Y_k}{\partial p}\right)_{T\,\phi}\left(-\frac{\dot{m}}{A}\frac{du}{dx} + I_m\right) \\ & + \left(\frac{\partial Y_k}{\partial T}\right)_{p\,\phi} \frac{1}{c_p}\left(\left(\left(\frac{\partial h}{\partial p}\right)_{T\,\phi} \frac{\dot{m}}{A} - u\right)\frac{du}{dx} - \left(\frac{\partial h}{\partial p}\right)_{T\,\phi} I_m - \left(\frac{\partial h}{\partial \phi}\right)_{p\,T} \frac{d\phi}{dx} + I_e\right) \\ & + \left(\frac{\partial Y_k}{\partial \phi}\right)_{p\,T} \frac{d\phi}{dx}\end{aligned}$$

Grouping the terms with $\frac{du}{dx}$ and $\frac{d\phi}{dx}$and we get:

$$\begin{aligned}\frac{dY_k}{dx} = {} & \left(\left(\frac{\partial Y_k}{\partial T}\right)_{p\,\phi} \frac{1}{c_p}\left(\left(\frac{\partial h}{\partial p}\right)_{T\,\phi} \frac{\dot{m}}{A} - u\right) - \left(\frac{\partial Y_k}{\partial p}\right)_{T\,\phi} \frac{\dot{m}}{A}\right)\frac{du}{dx} + \left(\left(\frac{\partial Y_k}{\partial \phi}\right)_{p\,T} - \left(\frac{\partial Y_k}{\partial T}\right)_{p\,\phi} \frac{1}{c_p}\left(\frac{\partial h}{\partial \phi}\right)_{p\,T}\right)\frac{d\phi}{dx} \\ & + \left(\frac{\partial Y_k}{\partial p}\right)_{T\,\phi} I_m + \left(\frac{\partial Y_k}{\partial T}\right)_{p\,\phi} \frac{1}{c_p} I_e - \left(\frac{\partial Y_k}{\partial T}\right)_{p\,\phi} \frac{1}{c_p}\left(\frac{\partial h}{\partial p}\right)_{T\,\phi} I_m\end{aligned}$$

Consider

$$\sigma_{1k} = \left(\left(\frac{\partial Y_k}{\partial T}\right)_{p\,\phi} \frac{1}{c_p}\left(\left(\frac{\partial h}{\partial p}\right)_{T\,\phi} \frac{\dot{m}}{A} - u\right) - \left(\frac{\partial Y_k}{\partial p}\right)_{T\,\phi} \frac{\dot{m}}{A}\right) \tag{16}$$

$$\sigma_{2k} = \left(\left(\frac{\partial Y_k}{\partial \phi}\right)_{p\,T} - \left(\frac{\partial Y_k}{\partial T}\right)_{p\,\phi} \frac{1}{c_p}\left(\frac{\partial h}{\partial \phi}\right)_{p\,T}\right) \tag{17}$$

$$\sigma_{3k} = \left(\frac{\partial Y_k}{\partial p}\right)_{T\,\phi} I_m + \left(\frac{\partial Y_k}{\partial T}\right)_{p\,\phi} \frac{1}{c_p} I_e - \left(\frac{\partial Y_k}{\partial T}\right)_{p\,\phi} \frac{1}{c_p}\left(\frac{\partial h}{\partial p}\right)_{T\,\phi} I_m \tag{129}$$

Therefore

$$\frac{dY_k}{dx} = \sigma_{1k}\frac{du}{dx} + \sigma_{2k}\frac{d\phi}{dx} + \sigma_{3k} \tag{130}$$

Substituting Eq (19) in Eq (2) we have:

$$\frac{d\boldsymbol{\mathcal{M}}}{dx} = -\boldsymbol{\mathcal{M}}^2 \sum \frac{1}{\mathcal{M}_k}\left(\sigma_{1k}\frac{du}{dx} + \sigma_{2k}\frac{d\phi}{dx} + \sigma_{3k}\right)$$

$$\frac{d\boldsymbol{\mathcal{M}}}{dx} = \left(-\boldsymbol{\mathcal{M}}^2 \sum \frac{\sigma_{1k}}{\mathcal{M}_k}\right)\frac{du}{dx} + \left(-\boldsymbol{\mathcal{M}}^2 \sum \frac{\sigma_{2k}}{\mathcal{M}_k}\right)\frac{d\phi}{dx} + \left(-\boldsymbol{\mathcal{M}}^2 \sum \frac{\sigma_{3k}}{\mathcal{M}_k}\right) \tag{31}$$

Derivative of Velocity

This derivative is computed in a way such that it is independent of dependent derivatives.
Using Eq (9) and Eq (12) and eliminating the term $\frac{1}{\rho}\frac{d\rho}{dx}$ we have:

$$\frac{1}{p}\frac{dp}{dx} - \frac{1}{T}\frac{dT}{dx} + \frac{1}{\boldsymbol{\mathcal{M}}}\frac{d\boldsymbol{\mathcal{M}}}{dx} + \frac{1}{u}\frac{du}{dx} + \frac{1}{A}\frac{dA}{dx} = \frac{\dot{m}_f}{\dot{m}}\frac{d\eta_m}{dx}$$

Using Eq(10) and substituting for $\frac{dp}{dx}$ we have

$$\frac{1}{p}\left(-\frac{\dot{m}}{A}\frac{du}{dx} + I_m\right) - \frac{1}{T}\frac{dT}{dx} + \frac{1}{\boldsymbol{\mathcal{M}}}\frac{d\boldsymbol{\mathcal{M}}}{dx} + \frac{1}{u}\frac{du}{dx} + \frac{1}{A}\frac{dA}{dx} - \frac{\dot{m}_f}{\dot{m}}\frac{d\eta_m}{dx} = 0$$

Using Eq(14) and substituting for $\frac{dT}{dx}$ we have

$$\frac{1}{p}\left(-\frac{\dot{m}}{A}\frac{du}{dx} + I_m\right) - \frac{1}{T}\left(\frac{1}{c_p}\left(\left(\left(\frac{\partial h}{\partial p}\right)_{T\,\phi}\frac{\dot{m}}{A} - u\right)\frac{du}{dx} - \left(\frac{\partial h}{\partial p}\right)_{T\,\phi} I_m - \left(\frac{\partial h}{\partial \phi}\right)_{p\,T}\frac{d\phi}{dx} + I_e\right)\right) + \frac{1}{\boldsymbol{\mathcal{M}}}\frac{d\boldsymbol{\mathcal{M}}}{dx}$$
$$+ \frac{1}{u}\frac{du}{dx} + \frac{1}{A}\frac{dA}{dx} - \frac{\dot{m}_f}{\dot{m}}\frac{d\eta_m}{dx} = 0$$

Using Eq(20) and substituting for$\frac{d\boldsymbol{\mathcal{M}}}{dx}$ we have

$$\frac{1}{p}\left(-\frac{\dot{m}}{A}\frac{du}{dx}+I_m\right)-\frac{1}{T}\left(\frac{1}{c_p}\left(\left(\left(\frac{\partial h}{\partial p}\right)_{T\,\phi}\frac{\dot{m}}{A}-u\right)\frac{du}{dx}-\left(\frac{\partial h}{\partial p}\right)_{T\,\phi}I_m-\left(\frac{\partial h}{\partial \phi}\right)_{p\,T}\frac{d\phi}{dx}+I_e\right)\right)$$
$$+\frac{1}{\mathcal{M}}\left(\left(-\mathcal{M}^2\sum\frac{\sigma_{1k}}{\mathcal{M}_k}\right)\frac{du}{dx}+\left(-\mathcal{M}^2\sum\frac{\sigma_{2k}}{\mathcal{M}_k}\right)\frac{d\phi}{dx}+\left(-\mathcal{M}^2\sum\frac{\sigma_{3k}}{\mathcal{M}_k}\right)\right)+\frac{1}{u}\frac{du}{dx}+\frac{1}{A}\frac{dA}{dx}$$
$$-\frac{\dot{m}_f}{\dot{m}}\frac{d\eta_m}{dx}=0$$

Pull all the terms containing $\frac{du}{dx}$ on LHS we have:

$$\left(\frac{u}{c_pT}+\frac{1}{u}-\frac{1}{c_pT}\left(\frac{\partial h}{\partial p}\right)_{T\,\phi}\frac{\dot{m}}{A}-\frac{\dot{m}}{pA}-\left(\mathcal{M}\sum\frac{\sigma_{1k}}{\mathcal{M}_k}\right)\right)\frac{du}{dx}$$
$$=-\frac{1}{A}\frac{dA}{dx}+\left(-\frac{1}{c_pT}\left(\frac{\partial h}{\partial \phi}\right)_{p\,T}+\left(\mathcal{M}\sum\frac{\sigma_{2k}}{\mathcal{M}_k}\right)\right)\frac{d\phi}{dx}-\frac{I_m}{p}-\frac{\left(\frac{\partial h}{\partial p}\right)_{T\,\phi}I_m}{c_pT}+\frac{I_e}{c_pT}$$
$$+\left(\mathcal{M}\sum\frac{\sigma_{3k}}{\mathcal{M}_k}\right)+\frac{\dot{m}_f}{\dot{m}}\frac{d\eta_m}{dx}$$

Taking

$$\alpha=\left(\frac{u}{c_pT}+\frac{1}{u}-\frac{1}{c_pT}\left(\frac{\partial h}{\partial p}\right)_{T\,\phi}\frac{\dot{m}}{A}-\frac{\dot{m}}{pA}-\left(\mathcal{M}\sum\frac{\sigma_{1k}}{\mathcal{M}_k}\right)\right) \tag{32}$$

$$\beta=\left(-\frac{1}{c_pT}\left(\frac{\partial h}{\partial \phi}\right)_{p\,T}+\left(\mathcal{M}\sum\frac{\sigma_{2k}}{\mathcal{M}_k}\right)\right) \tag{33}$$

$$\omega=\left(-\frac{I_m}{p}-\frac{\left(\frac{\partial h}{\partial p}\right)_{T\,\phi}I_m}{c_pT}+\frac{I_e}{c_pT}+\left(\mathcal{M}\sum\frac{\sigma_{3k}}{\mathcal{M}_k}\right)+\frac{\dot{m}_f}{\dot{m}}\frac{d\eta_m}{dx}\right) \tag{34}$$

Using Eq(21), Eq(22), Eq(1) and Eq(23) we have the governing equation for velocity which has only independent derivatives on right hand side:

$$\frac{du}{dx}=\frac{1}{\alpha}\left(-\frac{1}{A}\frac{dA}{dx}+\beta\frac{f}{f_{st}}\frac{d\eta_m}{dx}+\omega\right) \tag{35}$$

Quasi One Dimensional Flow Equations in Runge Kutta 4th Order Compatible Form

$$\frac{dp}{dx} = -\frac{\dot{m}}{A}\left(\frac{1}{\alpha}\left(-\frac{1}{A}\frac{dA}{dx} + \beta\frac{f}{f_{st}}\frac{d\eta_m}{dx} + \omega\right)\right) + I_m$$

$$\frac{dT}{dx} = \frac{1}{c_p}\left(\left(\left(\frac{\partial h}{\partial p}\right)_{T\,\phi}\frac{\dot{m}}{A} - u\right)\frac{du}{dx} - \left(\frac{\partial h}{\partial p}\right)_{T\,\phi} I_m - \left(\frac{\partial h}{\partial \phi}\right)_{p\,T}\frac{f}{f_{st}}\frac{d\eta_m}{dx} + I_e\right)$$

Where the parameters in governing equations are given by:

$$\alpha = \left(\frac{u}{c_p T} + \frac{1}{u} - \frac{1}{c_p T}\left(\frac{\partial h}{\partial p}\right)_{T\,\phi}\frac{\dot{m}}{A} - \frac{\dot{m}}{pA} - \left(\mathcal{M}\sum\frac{\sigma_{1k}}{\mathcal{M}_k}\right)\right)$$

$$\beta = \left(-\frac{1}{c_p T}\left(\frac{\partial h}{\partial \phi}\right)_{p\,T} + \left(\mathcal{M}\sum\frac{\sigma_{2k}}{\mathcal{M}_k}\right)\right)$$

$$\omega = \left(-\frac{I_m}{p} - \frac{\left(\frac{\partial h}{\partial p}\right)_{T\,\phi} I_m}{c_p T} + \frac{I_e}{c_p T} + \left(\mathcal{M}\sum\frac{\sigma_{3k}}{\mathcal{M}_k}\right) + \frac{\dot{m}_f}{\dot{m}}\frac{d\eta_m}{dx}\right)$$

$$\sigma_{1k} = \left(\left(\frac{\partial Y_k}{\partial T}\right)_{p\,\phi}\frac{1}{c_p}\left(\left(\frac{\partial h}{\partial p}\right)_{T\,\phi}\frac{\dot{m}}{A} - u\right) - \left(\frac{\partial Y_k}{\partial p}\right)_{T\,\phi}\frac{\dot{m}}{A}\right)$$

$$\sigma_{2k} = \left(\left(\frac{\partial Y_k}{\partial \phi}\right)_{p\,T} - \left(\frac{\partial Y_k}{\partial T}\right)_{p\,\phi}\frac{1}{c_p}\left(\frac{\partial h}{\partial \phi}\right)_{p\,T}\right)$$

$$\sigma_{3k} = \left(\frac{\partial Y_k}{\partial p}\right)_{T\,\phi} I_m + \left(\frac{\partial Y_k}{\partial T}\right)_{p\,\phi}\frac{1}{c_p} I_e - \left(\frac{\partial Y_k}{\partial T}\right)_{p\,\phi}\frac{1}{c_p}\left(\frac{\partial h}{\partial p}\right)_{T\,\phi} I_m$$

$$I_m = -\frac{(u - u_{fx})}{A}\dot{m}_f\frac{d\eta_m}{dx} - \frac{1}{2}\rho u^2\left(\frac{4c_f}{D_{Hb}}\right) + \rho F_{bx}$$

$$I_e = -\left(h + \frac{u^2}{2} - e_{tf}\right)\frac{\dot{m}_f}{\dot{m}}\frac{d\eta_m}{dx} - \frac{2c_f R_f(h_{aw} - h_w)}{D_{Hb}} + F_{bx} + \frac{\dot{q}_v}{u}$$

$$\phi = \frac{f}{f_{st}}\eta_m$$

Derivatives without analytical expression

$\left(\frac{\partial h}{\partial p}\right)_{T\,\phi}$; $\left(\frac{\partial h}{\partial \phi}\right)_{p\,T}$; $\left(\frac{\partial Y_k}{\partial T}\right)_{p\,\phi}$; $\left(\frac{\partial Y_k}{\partial p}\right)_{T\,\phi}$; $\left(\frac{\partial Y_k}{\partial \phi}\right)_{p\,T}$

Appendix D

Numerical Correction for Ramjet Burner Entrance

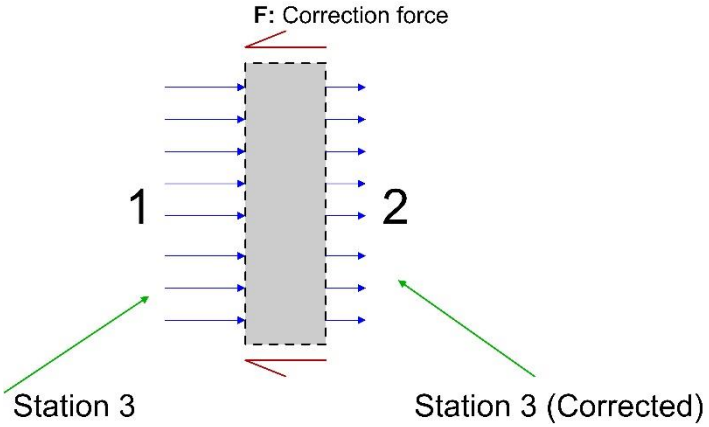

Figure 1.

The normal shock train model provides Mach number close to burner requested Mach number (but not exact). Say for example the burner imposed Mach number at station 3 is 0.7, if the normal shock train provides 0.68, then to reach the exact Mach number we consider a small "correction force" which acts as numerical correction to fill the gap of 0.02 Mach number. The correction is performed using CPG equations. Consider static pressure mass flow parameter.

$$MFp(\gamma, M) = \frac{\dot{m}\sqrt{T_t}}{pA} = M\sqrt{\frac{r}{R}\left(1 + \frac{\gamma - 1}{2}M^2\right)}$$

Impulse function

$$I = pA(1 + \gamma M^2)$$

Considering an adiabatic process with all the properties upstream (1) and Mach number downstream M_2 known, then the following equations are used for performing the required correction.

$$\frac{\dot{m}_1\sqrt{T_{t1}}}{p_1 A_1} = MFp(\gamma, M_1)$$

$$\frac{\dot{m}_2\sqrt{T_{t2}}}{p_2 A_2} = MFp(\gamma, M_2)$$

with $\dot{m}_1 = \dot{m}_2$, $T_{t1} = T_{t2}$ and $A_1 = A_2$ we have:

$$\boldsymbol{p_2 = p_1 \frac{MFp(\gamma, M_1)}{MFp(\gamma, M_2)}}$$

$$\boldsymbol{\rho_2 = \frac{\left(\frac{\rho_1 u_1^2}{M_2}\right)1}{\gamma\, p_2}}$$

$$\boldsymbol{T_2 = \frac{p_2}{\rho_2 R}}$$

$$\boldsymbol{u_2 = M_2\sqrt{\gamma R T_2}}$$

Therefore without explicitly estimating the correction force we can obtain the above corrected conditions. The correction force must have been:

$$F_{correction} = I_2 - I_1 = p_2 A_2(1 + \gamma M_2^2) - p_1 A_1(1 + \gamma M_1^2)$$

References

[1] Alexander S. Roudakov, Vyacheslav L. Semenov, and John W. Hicks., 1998, “Recent Flight Test Results of the Joint CIAM-NASA Mach 6.5 Scramjet Flight Program,”,NASA/TP-1998-206548, pp. 1–10.

[2] Vijaykumar, N., 2014, “Design and Multifidelity Analysis of Dual Mode Scramjet Compression System Using Coupled NPSS and Fluent Simulation,” M.S. Thesis, The University of Texas at Arlington, Arlington, TX.

[3] Chirstian Max Fischer, 2014, “Investigation of Isolator Flow of Scramjet Engines,” Thesis Dissertation, RWTH Aachen University.

[4] Fry, R. S., 2004. “A century of ramjet propulsion technology evolution. Journal of Propulsion and Power”, **20(1)**, 27-58.

[5] Driscoll, J. F., Huh, H., Yoon, Y., & Donbar, J., 1996. “Measured lengths of supersonic hydrogen-air jet flames—compared to subsonic flame lengths—and analysis. Combustion and Flame”, **107(1)**, 176-186.

[6] Doster, J. C., 2008. “Hypermixer pylon fuel injection for scramjet combustors”. ProQuest.

[7] Smart, M. K., Hass, N. E., & Paull, A., 2006. “Flight data analysis of the HyShot 2 scramjet flight experiment”. AIAA journal, **44(10)**, 2366-2375.

[8] Wilke, C. R., 1950. “A viscosity equation for gas mixtures”. The Journal of Chemical Physics, **18(4)**, 517-519.

[9] Emami, S., Trexler, C. A., Auslender, A. H., & Weidner, J. P., 1995 “Experimental investigation of inlet-combustor isolators for a dual-mode scramjet at a Mach number of 4”. NASA Technical Paper No. NASA-TP-3502.

[10] McBride, B. J., Gordon, S., & Reno, M. A. (1993).”Coefficients for Calculating Thermodynamic and Transport Properties of Individual Species”. NASA Technical Memorandum 4513.

[11] Tu, Q. 2013. “Effects of fuel injection on mixing and upstream interactions in supersonic flow” Thesis dissertation. University of Florida.

[12] Birzer, C. H., & Doolan, C. J., 2009. “Quasi-one-dimensional model of hydrogen-fueled scramjet combustors”. Journal of Propulsion and Power, **25(6)**, 1220-1225.

[13] Dalle, D. J., Frendreis, S. G., Driscoll, J. F., & Cesnik, C. E., 2010, August. “Hypersonic Vehicle Flight Dynamics with Coupled Aerodynamics and Reduced-order Propulsive Models”. In AIAA Atmospheric Flight Mechanics Conference & Exhibit.

[14] Anders Jr, J. B., 1975. “Effects of vibrational non-equilibrium on the inviscid design of an axisymmetric nozzle for hypersonic flow”. NASA STI/Recon Technical Report N, 75, 14991.

[15] Ben-Yakar, A., & Hanson, R. K., 2001. “Cavity flame-holders for ignition and flame stabilization in scramjets: an overview”. Journal of Propulsion and Power, **17(4)**, 869-877.

[16] Bray, K. N. C., & Appleton, J. P., 1961. “Atomic recombination in nozzles: methods of analysis for flows with complicated chemistry”. University of Southampton.

[17] Witte, D. W., & Tatum, K. E., 1994. “Computer Code for Determination of Thermally Perfect Gas Properties”. Vol. 3447, National Aeronautics and Space Administration, Langley Research Center.

[18] Segal, C., 2009. “The scramjet engine: processes and characteristics”. Vol. 25, Cambridge University Press.

[19] Surzhikov, S. T., & Seleznev, R. K., 2015 July. “Quasi-One-Dimensional and Two-Dimensional Numerical Simulation of Scramjet Combustors”. AIAA Joint Propulsion Conference.

[20] Nandakumar Vijayakumar, Donald. R. Wilson, Frank. K. Lu., 2014 July. “Multi-fidelity Simulation of a Dual Mode Scramjet Compression System using Coupled NPSS and FLUENT Codes”. AIAA Joint Propulsion Conference.

[21] Hall, J. G., & Treanor, C. E., 1967. “Nonequilibrium effects in supersonic-nozzle flows”. No. AGARD-OGRAPH-124, Advisory Group for Aerospace Research and Development Neuilly-Sur-Seine (France).

[22] Boyce, R. R., Paull, A., Stalker, R. J., Wendt, M., Chinzei, N., & Miyajima, H., 2000. “Comparison of supersonic combustion between impulse and vitiation-heated facilities”. Journal of Propulsion and Power, **16(4)**, 709-717.

[23] Anderson, J. D., 2000. “Hypersonic and High temperature Gas Dynamics”. AIAA.

[24] Hirschel, E. H., 2005. “Basics of aerothermodynamics”. p. 201, New York: Springer.

[25] Heiser, W. H., & Pratt, D. T., 1994. “Hypersonic Airbreathing Propulsion”. AIAA.

[26] Anderson, J. D., 1990. “Modern Compressible Flow: with historical perspective”. McGraw Hill Higher Education.

[27] “MATLAB® Primer 2015b user guide”, The MathWorks® Inc, Natick, M*A*.

[28] Balachandran, P., 2006. “Fundamentals of compressible fluid dynamics”. PHI Learning Pvt. Ltd.

[29] Mattingly, J. D., 1996. “Elements of gas turbine propulsion”, (Vol. 1), McGraw-Hill Science, Engineering & Mathematics.

[30] Butcher, J. C., 1987. “The numerical analysis of ordinary differential equations: Runge-Kutta and general linear methods”. Wiley-Interscience.

[31] Sitaraman, H., & Raja, L. L., 2013, “Magneto-hydrodynamics simulation study of high speed flow control using Rail Plasma Actuator (RailPAc)”. AIAA Plasmadynamics and Lazers Conference.

[32] Donald Ray Wilson., 1973, “Analysis of MHD Channel flows by a coupled core flow-boundary layer model,” PhD Thesis, The University of Texas at Arlington, Arlington, TX.

[33] Morgan, B., Duraisamy, K., & Lele, S. K., 2014. “Large-eddy simulations of a normal shock train in a constant-area isolator”. AIAA journal, ***52*****(3)**, 539-558.

[34] Carroll, B. F., 1988. “Numerical and Experimental Investigation of Multiple Shock Wave/Turbulent Boundary Layer Interactions in a Rectangular Duct”, Ph.D Thesis, University of Illinois at Urbana-Champaign, Urbana, IL, USA.

[35] McBride, B. J., & Gordon, S., 1996. “Computer program for calculation of complex chemical equilibrium compositions and applications: II. User’s manual and program description”. NASA reference publication, 1311, 84-85.

[36] Voland, R. T., Huebner, L. D., & McClinton, C. R., 2006. “X-43A hypersonic vehicle technology development”. Acta Astronautica, ***59*****(1)**, 181-191.

[37] Caitlin, H., 2010. “USAF successfully tests X-51A WaveRider”. Jane's defence weekly, ***47*****(22)**, 130-139.

[38] Marimon Mateu, M., 2013. “Study of an air-breathing engine for hypersonic flight” Technical Report, Universitat Politècnica De Catalunya.

[39] Prebola Jr, J. L., 1998. “Performance of a Plasma Torch with Hydrocarbon Feedstocks for Use in Scramjet Combustion”. Doctoral dissertation, Virginia Polytechnic Institute and State University.

[40] Tatum, K. E., 1996. “Computation of thermally perfect properties of oblique shock waves” Vol. 4749, National Aeronautics and Space Administration, Langley Research Center.

[41] Meador, W. E., & Smart, M. K., 2005. “Reference enthalpy method developed from solutions of the boundary-layer equations”. AIAA journal, **43(1)**, 135-139.

Biographical Information

Vijay Gopal was born in November 1990 to Mr. Gopal Ananthan and Mrs. Sheelavathy Gopal. He is an Indian national and earned his Bachelor of Engineering in Telecommunication Engineering at BMS College of Engineering, Bangalore, India in 2012. His passion towards high speed aerodynamics made him pursue Masters of Science in Aerospace Engineering at The University of Texas at Arlington. He plans to continue a research career in the domain of high speed aerodynamics and propulsion.